Pressure effect on Single-walled and Double-walled Carbon Nanotubes Investigated by Infrared Spectroscopy

Dissertation zur Erlangung des Doktorgrades
der Mathematisch-Naturwissenschaftlichen
Fakultät der Universität Augsburg

vorgelegt von
Ahmed Sobhy Mohamed Morsy Abouelsayed

Jun 2012

Erstgutachter:	Prof. Dr. C.A. Kuntscher
Zweitgutachter:	Prof. Dr. A. Reller

Tag der mündlichen Prüfung: 11 October 2012

Contents

1 Introduction

Since the discovery of carbon nanotubes in 1991 by Iijima [1] extensive experimental and theoretical studies have been made on their structural, mechanical, thermodynamic, and electronic properties. These studies have been motivated by scientific and technological interest. The reason for this enthusiasm lies in the amazing physical properties of carbon nanotubes. They are a model system for one-dimensional physics, relatively easy in preparation, and possess a great potential for applications. The combination of these features will motivate the researchers in this field to conduct more investigations on the electronic properties of carbon nanotubes and will also encourage small and large industries to its applications. One-dimensionality inherent to carbon nanotubes results in a large anisotropy of optical absorption, depolarization effects and vibrational confinement. In addition, the electronic behavior is described by the Luttinger-liquid in contrast to two- and three-dimensional solids where the Fermi liquid behavior is expected. In addition to the applications, the carbon nanotubes offer a large scope for studying various physical phenomena induced in the low-dimensional systems. The low-dimensional systems have produced new light on the effects of the electron-phonon interactions, and the electron-electron interaction on a quantum system.

The goal of this project was to study the influence of high hydrostatic pressure on the electronic properties of single-walled carbon nanotubes (SWCNTs), peapods (C_{60} encapsulated SWCNTs) and the double-walled carbon nanotubes (DWCNTs). High pressure studies will enable researchers to observe closely and investigate effectively the electronic properties of carbon nanotube under extreme stress conditions. Particularly interesting are the effects caused by hydrostatic compression which leads to radial deformation and further collapse of carbon nanotubes. This is obviously manifested in the distortion in the carbon nanotube cross section, and change, for example, to an oval shape. The structural deformation is generally expected for any hollow tubular structures, when it is exposed to a certain critical external pressure. Carbon nanotube may withstand such extreme deformations and recover their initial properties on release of the external stress. However, electronic, optical, as well as chemical properties are expected to be very suddenly and noticeably affected by this collapse.

Optical spectroscopy and high pressure techniques provides further information by studying the induced interband transitions. The analysis of the induced interband transitions allows conclusions about the band structure of the studied material. One of the main goals of this work is to clarify the relevance of the pressure transmitting media regarding the pressure-induced effects in SWCNTs. Therefore, pressure-dependent transmittance measurements were performed using helium, CsI and alcohol mixture as pressure transmitting media. The results from this work will be compared with those previously obtained from argon [2,3]. We also studied the role of pressure transmitting media in the *oriented* SWCNTs.

In addition, infrared spectroscopic measurements on peapods (C_{60} encapsulated SWCNTs) and double-walled carbon nanotube (DWCNTs) under pressure have been performed. Several interesting features can be seen: "DWCNTs are more stable than SWCNTs [4]". The internal tube is protected by the external tube against the application of pressure. "Multi-walled carbon nanotube samples have a wide range of diameters and variable number of walls, which makes it difficult to distinguish contributions from internal and external tubes. Double wall carbon nanotubes with narrow diameter distribution have recently become available and contributions from the internal tubes in the Raman spectrum have been identified [4]".

Basic properties of carbon nanotube and the changes in the electronic response of the nanotubes under high pressure are further explained in Chapter 2. The Optical coefficient, the Fourier transform infrared spectroscopy, high-pressure generation technique are described in Chapter 3. The studied nanotube films i.e., unoriented and oriented nanotubes, C_{60} peapods and DWCNTs are presented in Chapter 3. The results, analysis and discussion of the pressure-dependent infrared studies on the SWCNTs, C_{60} peapods and DWCNTs films are illustrated in Chapter 4. Finally I summarized the findings of this work in the Chapter 5.

2 Properties of Carbon Nanotubes

The first section of this chapter will briefly stipulate the electronic properties of graphene. Then, the geometric structure of carbon nanotubes and the construction of their Brillouin zone in relation to that of graphite will be described. After briefly discussing the electronic properties of graphene, the concept of the zone folding will be introduced, demonstrating the properties of single-walled carbon nanotubes and how they can be directly obtained from the known properties of graphene. Zone folding combined with tight binding allows the calculation of the band structure of carbon nanotubes. Next, it will be clear how, the density of sates of single-walled carbon nanotubes is characterized by van-Hove singularities. The effect of nanotube bundles and the optical properties of the carbon nanotubes will also be discussed. Finally in the last section, I explained the single-walled, C_{60} peapods and double-walled carbon nanotubes under pressure.

2.1 Electronic band structure of graphene

Figure 2.1 shows the hexagonal Brillouin zone and the band structure calculation of graphene using the tight-binding approximation model [5–7]. It is clear from the Figure that the valence bands and conduction bands are crossing at K point in the graphene Brillouin zone, but the electronic energy states is zero at the crossing point, and this means that Graphene is a semimetal [6]. The electronic energy states close to Fermi level of graphene contains the π states perpendicular to the graphene sheet and their interactions. From the tight binding approximations, the electronic band structure of graphene are given by the equation [5–7]:

$$E^{\pm}(\mathbf{k}) = \pm\gamma_0 \left\{ 1 + 4\cos(\frac{\sqrt{3}\mathbf{k}_x a}{2})\cos(\frac{\mathbf{k}_y a}{2}) + 4\cos^2(\frac{\mathbf{k}_y a}{2}) \right\}^{1/2} \quad . \tag{2.1}$$

From this equation, the the valence and conduction bands of graphene are given by E^- and E^+ respectively (see Figure 2.1 (b)). "$E^+(k)$ and $E^-(k)$ are called bonding

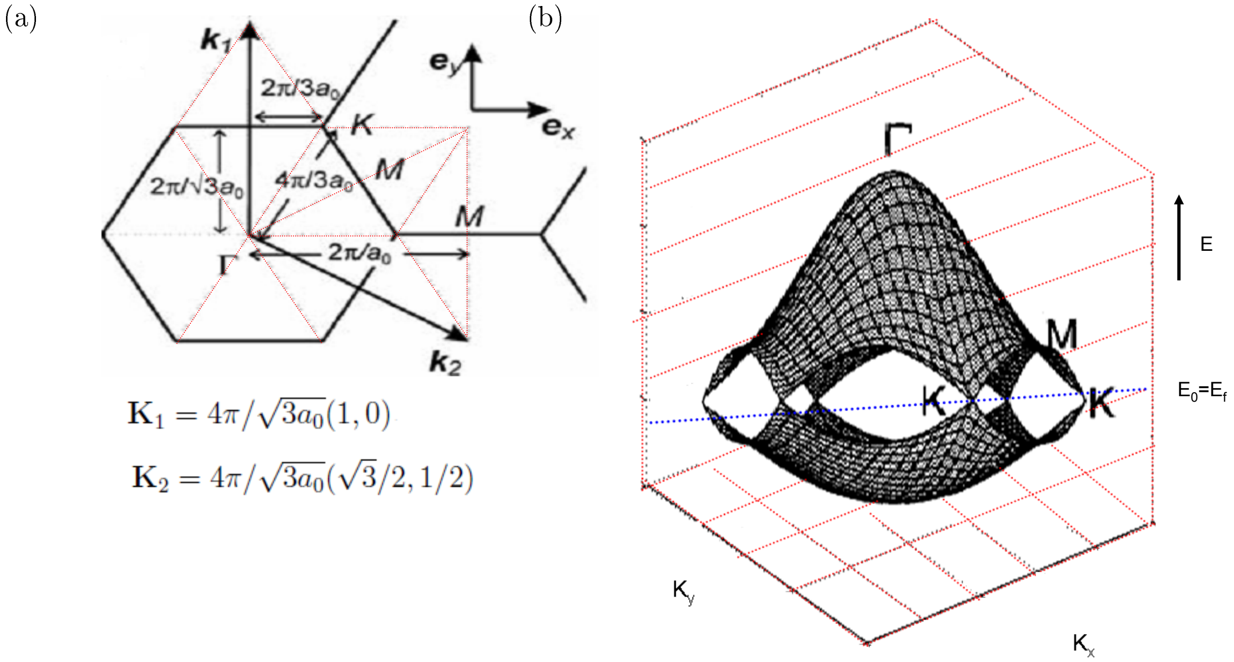

Figure 2.1: *(a) Hexagonal Brillouin zone of graphene. The figure shows the highsymmetry* Γ*, M and K points.* k_1 *and* k_2 *are the reciprocal lattice vectors of graphene [5]. (b) The energy dispersion relations for* σ *and* π *bands of two-dimensional graphite [6].*

and antibonding energy bands respectively [5,6]". **a** is lattice constant of graphene (see Figure 2.1 (a)), **k** is the wavevector of electrons for the graphene Brillouin zone, the interaction between two π electrons is $\pm\gamma_0$. The values of $\pm\gamma_0$ changes between 2.7 eV to 3.1 eV, depending on the method of calculation. The electronic band structure of graphene close to the Fermi energy, which is calculated by the nearest-neighbor tight-binding model of equation (2.1), shows a deviation by 0.5 eV to 1 eV from ab-initio calculations [8]. The equation (2.1) is used in section 2.3 to obtain the electronic dispersion relations for carbon nanotubes.

2.2 Structure of single-walled carbon nanotubes

The unrolled graphene sheet of a nanotube is shown in Figure 2.2. When we connect the points X and Y, and Z and W, Saito demonstrated that "a nanotube can be constructed [6]". The wrapping vector is explained by the vector **C**, and the vector **T** determines the translational vector of the nanotube. The red rectangle $XYZW$ defines the unit cell for the nanotube (see Figure 2.2). The structure of a single-wall

Nanotube	Chiral (n_1, n_2)	Armchair $\mathrm{n}_1 = n_2 = n$	Zigzag $\mathrm{n}_2 = 0, n_1 = n$
Diameter (d)	$d = \frac{\lvert\mathbf{C}\rvert}{\pi} = \frac{a_0\sqrt{n_1^2+n_1n_2+n_2^2}}{\pi}$	$d = \frac{\sqrt{3}na}{\pi}$	$\frac{na}{\pi}$
Number of hexagon (N)	$N = \frac{2(n_1^2+n_1n_2+n_2^2)}{d_R}$	$N = 2n$	$N = 2n$
Chiral angle (θ)	$\cos\theta = \frac{2n_1+n_2}{2\sqrt{n_1^2+n_1n_2+n_2^2}}$	$\cos\theta = \frac{2n_1+n_2}{2\sqrt{n_1^2+n_1n_2+n_2^2}}$	$\cos\theta = \frac{2n_1+n_2}{2\sqrt{n_1^2+n_1n_2+n_2^2}}$

Table 2.1: *The comparison between the diameter, chiral angle and number of hexagon of chiral, armchair and zigzag carbon nanotubes [6].*

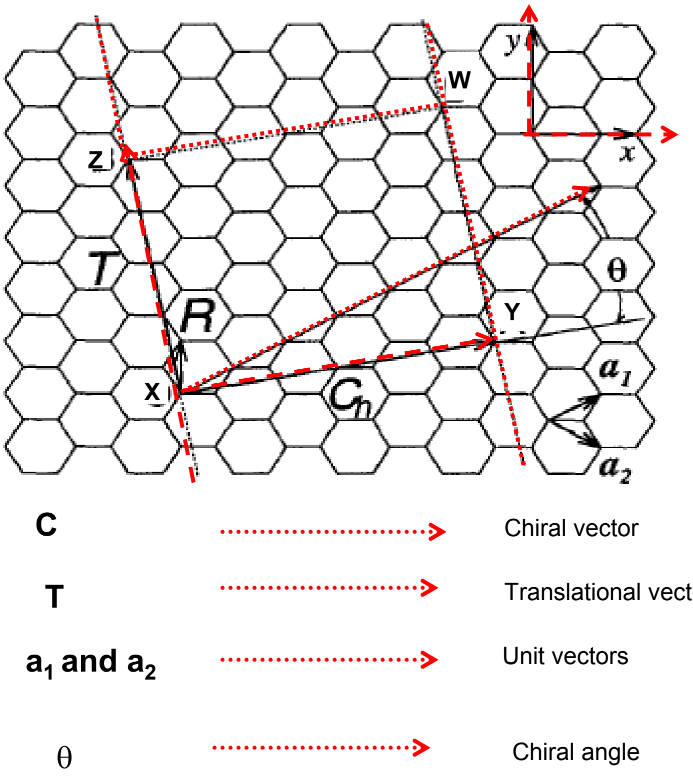

Figure 2.2: *The construction of a carbon nanotube from a graphene sheet. A nanotube indicated by the indices (4,2) is formed. The vector, which is perpendicular to* **C** *runs in the direction of the tube axis indicated by vector* **T** *[6].*

carbon nanotube is specified by the vector **C** which is perpendicular to the nanotube axis and the vector **T** in the direction of the nanotube axis [6]. By rolling the graphene sheet the points X and Y coincide as well as Z and W as shown in Figure 2.2. The wrapping (chiral) vector **C** can be represented as a linear combination of the two unit vectors $\mathbf{a_1}$ and $\mathbf{a_2}$ and is defined by $\mathbf{C} = n_1\mathbf{a_1} + n_2\mathbf{a_2}$. Where $\mathbf{a_1}$ and $\mathbf{a_2}$ are the two unit vectors of graphene sheet. "The diameter of the carbon nanotube, d, is given by $\frac{|\mathbf{C}|}{\pi}$, in which $|\mathbf{C}|$ is the circumferential length of the carbon nanotube [5,6]":

$$d = \frac{|\mathbf{C}|}{\pi} = \frac{a_0\sqrt{n_1^2 + n_1n_2 + n_2^2}}{\pi} \tag{2.2}$$

"The chiral angle θ (see Figure 2.2) is defined as the angle between the wrapping vector **C** and a_1, with values of θ in the range $0^\circ \leq \theta \leq 30^\circ$, because of the hexagonal symmetry of the graphen lattice [6]". Saito demonstrated that "the chiral angle θ denotes the tilt angle of the hexagons with respect to the direction of the nanotube axis, and the angle θ specifies the spiral symmetry [6]". The direction of the wrapping vector **C** is determined by the chiral angle θ, which is defined by the equation [5,6]:

$$\cos\theta = \frac{2n_1 + n_2}{2\sqrt{n_1^2 + n_1n_2 + n_2^2}} \tag{2.3}$$

The unit cell of the $1D$ carbon nanotube is the rectangle $XYZW$ defined by the vectors **C** and **T** (see Figure 2.2). "The number of hexagons per unit cell N is obtained as a function of n_1 and n_2 [5,6]":

$$N = \frac{2(n_1^2 + n_1n_2 + n_2^2)}{d_R} \tag{2.4}$$

where d_R is the greatest common divisor of $2n_2 + n_1$ and $2n_1 + n_2$. Thus, there are $2N$ carbon atoms in each unit cell of the carbon nanotube. Depending on the wrapping vector **C** and the chiral angle θ, the nanotubes are classified as zig-zag, chiral and armchair tubes (see Figure 2.3). The tubes of type $n_2 = 0$ and $\theta = 0$ are called zig-zag tubes. The tubes with $n_1 = n_2$ and $\theta = 30^\circ$ are called armchair tubes and all other tubes are known as chiral tubes. The diameter, θ and the number of hexagon of chiral, zigzag and armchair nanotube are listed in Table 2.1.

2.3 Electronic structure of single-walled and double-walled carbon nanotubes

Zone-Folding

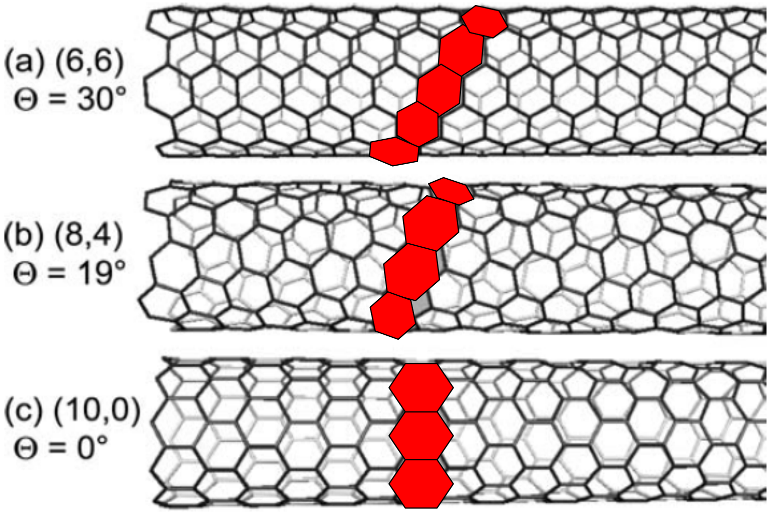

Figure 2.3: *The chirality of the three carbon nanotubes are as follows: (a) (6,6) armchair, (b) (8,4) chiral tube and (c) (10,0) zigzag nanotube [9].*

The electronic band structures of carbon nanotubes were calculated by using zone-folding approximation as well as by using first-principle calculations [5, 6, 8, 10–13]. The zone-folding is a simple method for calculation of the band structure of carbon nanotubes. In Refs. [5, 6], it was demonstrated how the zone-folding approximation can be used to identify the electronic energy states of carbon nanotubes from the electronic band structure of graphene obtained by using the tight binding model.

Reich demonstrated that "single-walled carbon nanotubes are one-dimensional solids [5]". There are several factors which should be considered regarding the unit cell of carbon nanotube: the number of the hexagon and the number of carbon atoms in the unite cell. It is clear from section 2.1 that the unit cell of carbon nanotube is defined by the two vectors: wrapping vector **C** and the translational vector **T** (see Figure 2.2). In the description of the two dimensional Brillouin zone of a single layer graphite, the allowed states of single wall carbon nanotube will lie along parallel lines separated by equal spacing. Therefore, the first Brillouin zone consists of a number of lines parallel to the tube axis. "As the tube is regarded as infinitely long, the wave vector k_z is continuous [5]".

Along the circumference of the tube, "the wave vector $\mathbf{K}_\perp$ is quantized according to the boundary condition [5, 6]". Thus, electronic band structure of a carbon nanotube can be derived from the electronic structure of graphene by taking into account the quantization along the circumference of the tube. To introduce simple explanation of the zone-folding approximation, the unit cell of the nanotube is obtained by suitably expanding the unit cell of graphene, as well as, the graphene Brillouin zone of the nanotube can be obtained by suitably reducing the Brillouin zone of graphene. The quantization along the circumference of the tube based on the boundary condition can be made by using the following simple statement. Let us consider a wavefunction with wavelength λ propagating along the circumference of the nanotube. If m is the number of nodes of this wave, the quantized waves along the circumference can be obtained using the following equation [5]:

$$m \cdot \lambda = |\mathbf{C}| = \pi \cdot d \tag{2.5}$$

$$\mathbf{K}_{\perp,m} = \frac{2\pi}{\lambda} = \frac{2}{d} \cdot m \tag{2.6}$$

"The quantize wave vector $\mathbf{K}_{\perp}$ is found from [5]":

$$\mathbf{K}_{\perp} \cdot C = 2\pi \tag{2.7}$$

This result indicates that the Brillouin zone is reduced to m lines parallel to the tube axis when the sheet is rolled up to form a nanotube. These allowed m lines are equidistant, and the distance between two neighboring lines is $\frac{2}{d}$. Therefore, the electronic states along the nanotube circumference are discrete [5, 6]. On the other hand, along the tube axis the electronic states are continuous. Now, we will see how the band structure of single-walled carbon nanotube can be calculated from the band structure of graphene. The diameters of an armchair nanotube d_A with chirality (n, n) and of a zigzag nanotube d_Z with chirality $(n, 0)$ are obtained from equation (2.2) as:

$$d_A = \frac{\sqrt{3} n a_0}{\pi} \tag{2.8}$$

$$d_Z = \frac{n a_0}{\pi} \quad , \tag{2.9}$$

The equations (2.8, 2.9 and 2.6) are used to get the periodic boundary conditions and to obtain the energy eigenvalues for the (n, n) armchair, $(n, 0)$ zigzag and (n_1, n_2) chiral nanotubes. Saito *et al.* [6] discussed the energy dispersion relation for armchair, zigzag and chiral nanotube at Γ, M and K points in the Brillouin zone. Saito demonstrated that "all (n, n) armchair nanotubes have a band degeneracy between the

Nanotube (n_1, n_2)	(Γ point)	(K point)	Zone boundary (X point)
Armchair $n_1 = n_2 = n$ Always metallic	k$= 0$ The bands nondegenerate	k$=\pm\frac{\pi}{3a}$ The bands degenerate and cross the Fermi level	k$= \pm\frac{\pi}{a}$
Zigzag $n_2 = 0, n_1 = n$ (9,0) (10,0)	k=0 (metallic) (semiconducting)		k$=\pm\frac{\pi}{\sqrt{3}a}$

Table 2.2: *The comparison between the band structure of armchair and zigzag carbon nanotubes [6].*

highest valence band and the lowest conduction band at $k = \pm 2\pi/3a$ and at the zone boundary ($ka = \pi$), where the bands cross the Fermi level [6]". In the case of zigzag nanotube $(n, 0)$, Saito demonstrated that " when n is a multiple of 3, the energy gap at $k = 0$ becomes zero; however, when n is not a multiple of 3, an energy gap opens at $k = 0$ [6]". The conclusions of their study are listed in Table 2.2.

Figure 2.4 shows the comparison between band structure, which is calculated be using the zone-folding approximation and by using first-principles calculations method for armchair nanotube with chirality $(10, 10)$ [5, 8, 9]. There is almost no difference between the band structure calculation by using these two method, while considering the third neighbor interaction between the carbon atom in the graphene sheet (see Figure 2.4 (a) and (c)). It is also clear from Figure 2.4 there is crossing between the valence and conduction bands at the K point, which means that the nanotube is metallic. In general, carbon nanotube can be semiconducting or metallic depending on the two chiral indices n_1 and n_2. In the following, we discuss how the electronic properties of carbon nanotube depend on the diameter as well as the chirality of the carbon nanotube.

Based on the zone-Folding approximation, Reich *et al.* [5] derived a straightforward equation which explain whether a tube of given chirality is metallic or semiconducting. As it can be seen in Figure 2.5, the valence and conduction bands only cross at the K points (the corners of the hexagonal Brillouin zone). For that reason, if one of the allowed lines passes through one of these points, a nanotube with given chirality n_1 and n_2 is metallic. This condition is fulfilled if the difference between the two chiral indices is multiple by three. In the other words, Reich *et al.* [5] showed from the following equation that the carbon nanotube can be metallic or semiconducting depending on

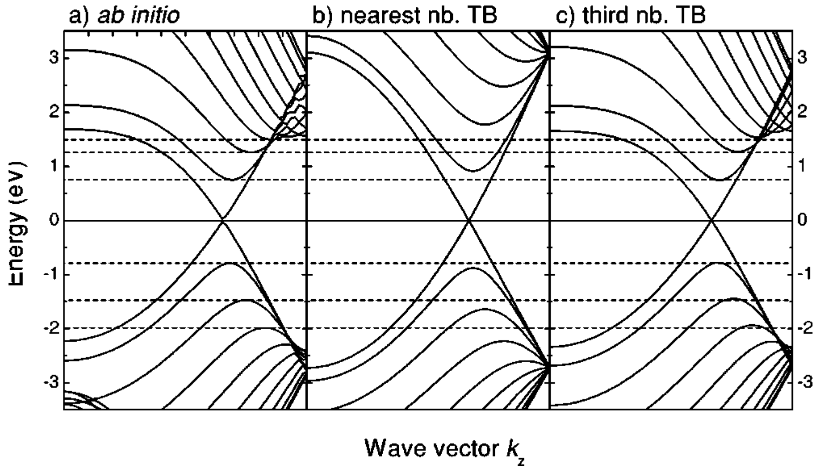

Figure 2.4: *The calculated band structure for metallic armchair nanotube with chirality* (10, 10) *for using (a) The ab-initio calculation model, (b) Tight binding model considering only the first neighbor interaction between the carbon atoms in the graphene sheet and (c) Tight binding model considering the third neighbor interaction between the carbon atoms in the graphene sheet [5, 8].*

the two chiral indices n_1 and n_2.

$$\mathbf{K}\cdot\mathbf{C} = \frac{1}{3}(\mathbf{k}_1 - \mathbf{k}_2)\cdot(n_1\mathbf{a}_1 + n_2\mathbf{a}_2) = \frac{2\pi}{3}(n_1 - n_2) = 2\pi m \tag{2.10}$$

where m is an integer, $\mathbf{K}$ is the graphene corner point and $\mathbf{C}$ is chiral vector. "The graphene K point is at $\frac{1}{3}(\mathbf{k}_1 - \mathbf{k}_2)$ [5]"

$$3m = n_1 - n_2 \quad , \tag{2.11}$$

In general, if $n_1 - n_2$ is a multiple of three the nanotube is metallic and if $n_1 - n_2$ is not multiple of three the nanotube is semiconducting. In the case of armchair nanotube, where the two chiral indices n_1 and n_2 are equal, the difference between $n_1 - n_2$ is equal to zero. Therefore, the armchair nanotubes are always metallic [5, 6]. However, a curvature effect moves the Fermi wave vector K_F away from the K point of the Brillouin zone in case of metallic nanotubes. This results in a very small band gap opened at E_F. The origin of this curvature-induced gap in metallic nanotubes is related to the reduction of the distance between the carbon atoms along the circumferential direction as a result of rolling up the graphene sheet into a cylinder. Saito *et al.* [14, 15] discussed the curvature effect in single walled carbon nanotubes. He found that the hopping integral γ_0 of a SWCNTs is changed with changing the tube diameter

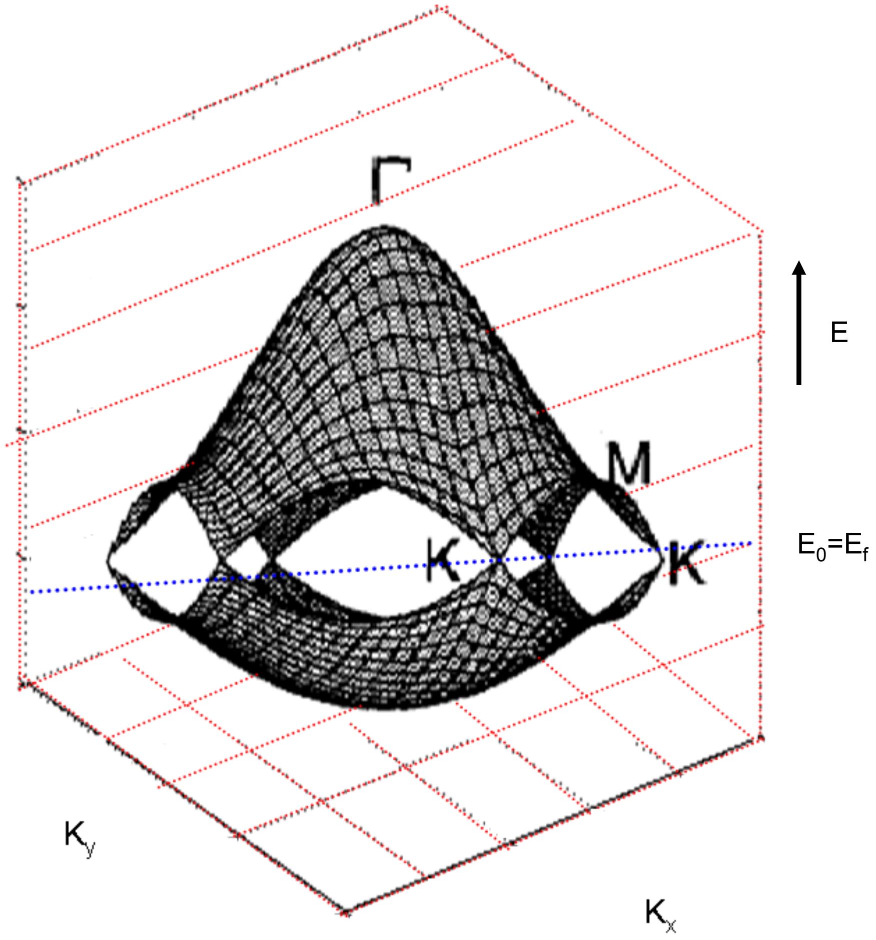

Figure 2.5: *The two dimensional band structure calculation of graphene using tight binding approxmation [6].*

according to: $\gamma_0(d) = \gamma_0\{1 - \frac{1}{2}(\frac{a_{c-c}}{d})^2\}$. a_0 is the lattice constant of carbon nanotube, which is slightly larger than the lattice constant of graphene. The lattice constant is equal 1.44 Å for a SWCNTs. In the case of armchair nanotube with chirality $(10, 10)$ and diameter $d = 1.4\ nm$, "the relative correction to $\gamma_0(d)$ is thus only 10^{-2} [15]". Therefore, the secondary gap is generally so small except for very small diameter nanotubes. "Within the nearest-neighbor tight-binding description the secondary gap or curvature induced gap is given by $E_{gab} = \frac{\gamma_0 a_0^2}{4d^2} \cos 3\theta$ [5]", where a_0 is the lattice constant of graphene. The curvature effect is typically neglected that "the expected magnitude of the secondary band gap on the order of 10 meV may sound too small for an experimental verification [5]". Figure 2.6 (a) shows the allowed energy states of a general semiconducting nanotube. Clearly, from Figure 2.6 (b) there is no crossing of

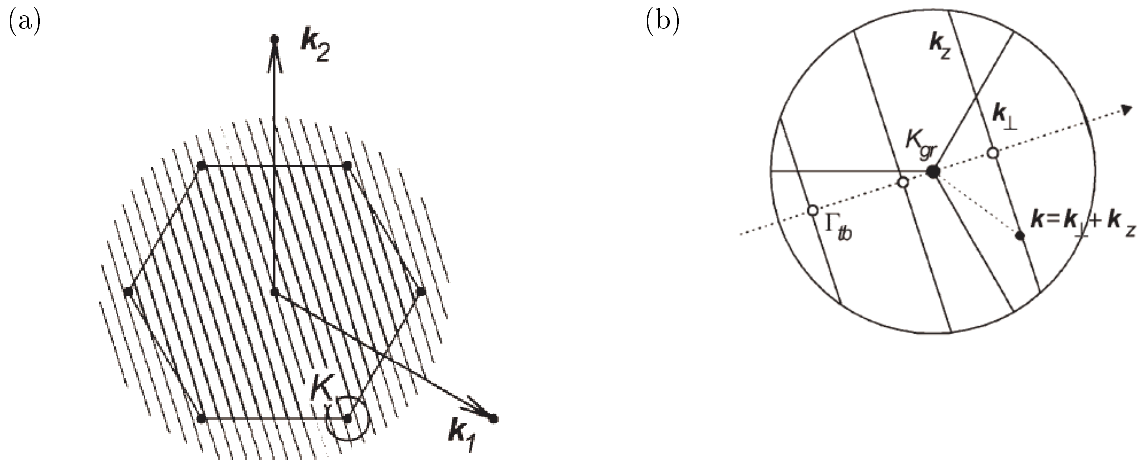

Figure 2.6: *(a) An illustration of how graphene Brillouin zone shows the allowed wavevectors of a carbon nanotube. (b) The drawing illustrate the increase in size of the allowed wavevectors* $\mathbf{k}$ *around the* K *point where,* $\mathbf{K}_z$ *is the allowed wavevector parrel to the tube axis, and* $\mathbf{K}_\perp$ *is the allowed wavevector perpendicular to the tube axis. The* Γ *point of the nanotube is represented by the open dots* $\mathbf{K}_z = 0$ *[5, 9].*

the energy state at the K point.

Double-walled carbon nanotubes

The electronic band structures of the DWCNTs were calculated by Saito *et al.* [16, 17], in particular for the tubes with chirality $(5,5)@(10,10)$. Their calculation method is based on the tight binding approximation as well as first-principle calculations by considering only nearest-neighbor interactions within a graphene layer, and using the same values for three dimensional graphite, $\gamma_0 = 3.13\ eV$ and $\gamma_1 = 0.35\ eV$ [6, 16–19]. Where γ_0 is hopping integral and γ_1 is the the interlayer interaction between the two graphene sheets. Saito demonstrated that "the determinant of the Hamiltonian matrix for a $(5,5)@(10,l0)$ DWCNT can be obtained as follows [16]":

$$det(H - EI) = (e-1)^3(e+1)^3(e^3 - e^2 - e - g_1^2 e + 1) * (e^3 + e^2 - e - g_1^2 e - 1) = 0 \quad (2.12)$$

"Where $e = \frac{E}{\gamma_0}$ and $g_1 = \frac{\gamma_1}{\gamma_0}$ [16]". Figure 2.7 shows the two layer of graphene sheets. All four tubes are known to be metallic from equation (2.11). The gap between the two layer of the graphene sheets is ≈ 3.44 Å [16]. In general, the relative orientation of the inner and outer tubes can be slightly changed in order to match the carbon site locations, also it can happen for each pair of coaxial tubes [6]. The formation of

Nanotube (n_1, n_2)	Translation vector (T)	Ratio of (T) $\frac{T_{inner}}{T_{outer}}$	Commensurate ratio
Armchair $n_1 = n_2 = n$ Inner (n_1, n_1) Outer (n_2, n_2)	$T_{inner} = a$ $T_{inner} = a$	1	1:1
Zigzag $n_2 = 0$ Inner ($n_1, 0$) Outer ($n_2, 0$)	$T_{inner} = \sqrt{3}a$ $T_{outer} = \sqrt{3}a$	1	1:1
Armchair as inner Zigzag as outer Inner (n_1, n_1) Outer ($n_2, 0$)	$T_{inner} = a$ $T_{outer} = \sqrt{3}a$	$\frac{1}{\sqrt{3}}$	The inner and outer tube can not commensurate
Chiral Different diameter Inner (n_1, n_2) Outer (n_3, n_4)	$T = \frac{\sqrt{3}L}{d_R}$ $T = \frac{\sqrt{3}L}{d_R}$	Irrational number in units of a	In general, the inner and outer tube can not commensurate

Table 2.3: *Commensurate relation for armchair, zigzag and chiral double wall carbon nanotube [6].*

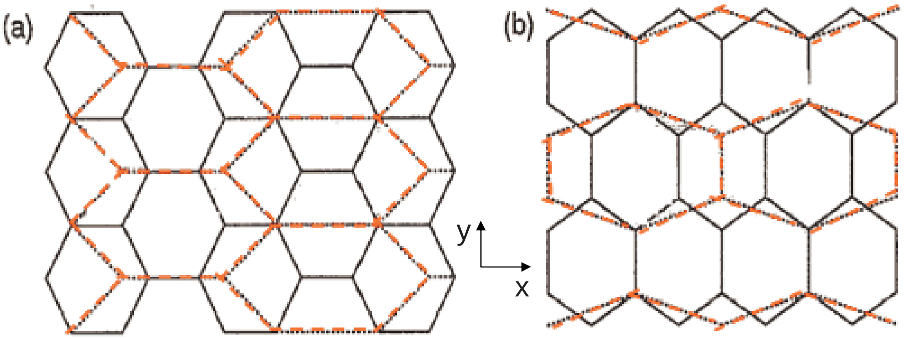

Figure 2.7: *The construction of the unit cell of a double layer carbon nanotube from a graphene sheet for (a)* $(5,5)@(10,10)$ *and (b)* $(9,0)@(18,0)$*. In order to see the inner tube, the inner tube (dotted red line) is projected on the outer tube (solid line) [16].*

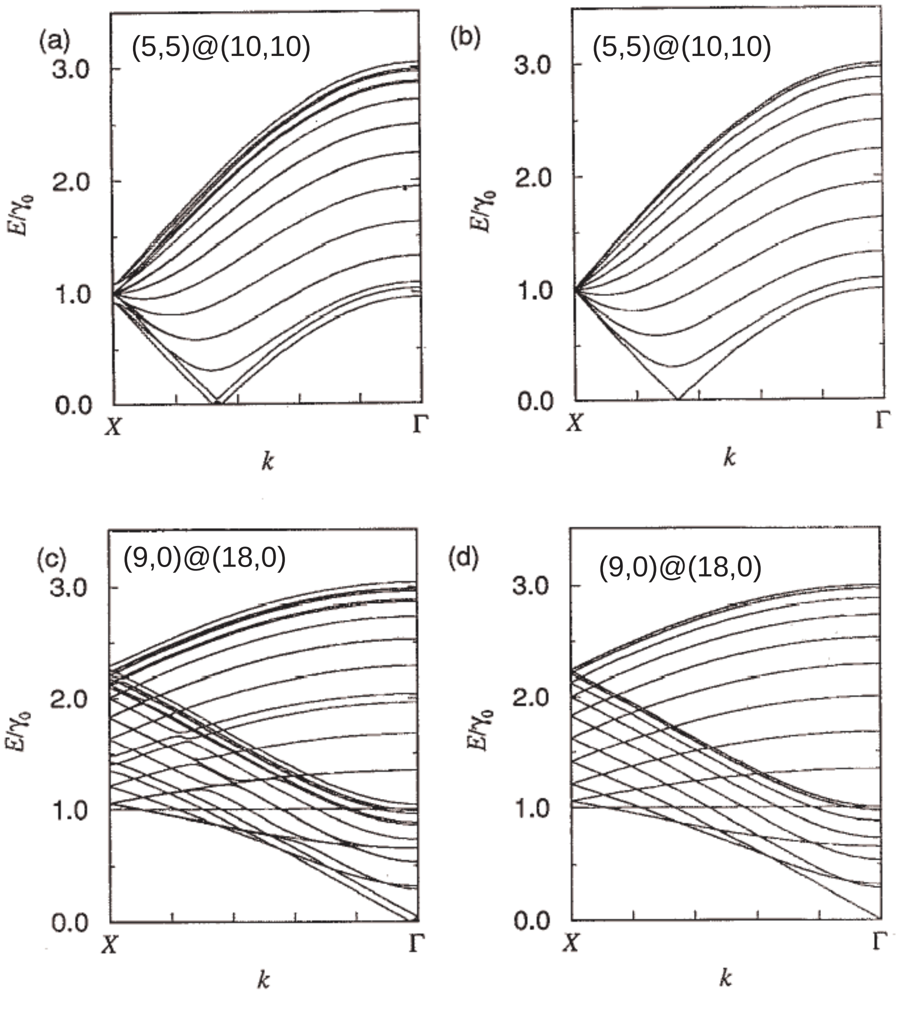

Figure 2.8: *The calculated energy dispersion relation for the double walled carbon nanotube* $(5,5)@(10,10)$ *(a) and (b) and* $(9,0)@(18,0)$ *in (c) and (d) in which the interlayer interaction* $\gamma_1 = 0.35\ eV$ *in (a) and (c) and* $\gamma_1 = 0\ eV$ *in (b) and (d) for comparison [16].*

	Interlayer interaction $\gamma_1 = 0$	Interlayer interaction $\gamma_1 = 0.35\ eV$
Number of energy bands E(k)	Figure 2.8 (b) (5,5)@(10,10) n$_i$ = 5 (*inner tube*) n$_{out}$ = 10 (*outer tube*) E(k)=11 for E $>$ 0	Figure 2.8 (a) (5,5)@(10,10) (splitting of E(k)) E(k)= 30 for E $>$ 0
Number of energy bands E(k)	Figure 2.8 (d) (9,0)@(18,0) n$_i$ = 9 (*inner tube*) n$_{out}$ = 18 (*outer tube*) E(k)=19 for E $>$ 0	Figure 2.8 (c) (9,0)@(18,0) (splitting of E(k))

Table 2.4: *The comparison between the band structure calculation of the double walled carbon nanotube with different chirality and by considering* $\gamma_1 = 0\ eV$ *and* $\gamma_1 = 0.35\ eV$ *[16].*

double walled carbon nanotube (inner and outer tube) can be commensurate to each other or non-commensurate. It depends on the ratio of two diameters as well as the ratio in the direction of the nanotube axis z. Table 2.3 shows commensurate relation for different types of double walled carbon nanotube along the z axis [6].

In the following, the band structure for two best-matched commensurate double-walled carbon nanotube will be discussed [16]. Figure 2.8 shows the energy dispersion relations for two commensurate armchair DWCNTs with different chirality. Saito illustrated that "this figure present the band structure of the DWCNTs when the interlayer interaction $\gamma_1 = 0.35\ eV$ (see equation (2.12) and Figure 2.8 (a) and (c)) [16]". Also for comparison, when γ_1 is equal to zero as shown in Figure 2.8 (b) and (d). Saito *et al.* [16] observed that the energy dispersion relations of the double walled carbon nanotube are changed with changing the values of the interlayer interaction between the inner and outer tube. Saito demonstrated that "when the interlayer interaction between the inner and the outer tube is not considered, i.e., $\gamma_1 = 0$ the energy dispersion relations $E(k)$ are just the overlay of the energy dispersion relations of the unperturbed inner and outer tubes [16]". On the other hand, when the interlayer interaction γ_1 is equal to 0.35 eV, some of the energy bands are split by the interlayer interaction [16]. Their observations are listed in the Table 2.4. n_i and n_{out} are the number of the allowed energy bands of the inner-tube and outer-tube respectively.

Energy gap, van-Hove singularities of SWCNTs

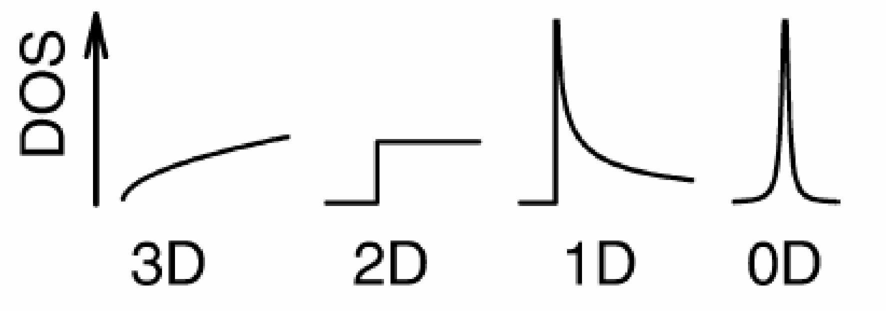

Figure 2.9: *An illustration of the density of states in three, two, one, and zero-dimensional systems. The density of states is inversely proportional to the square root of energy ($1/\sqrt{E}$) for one-dimensional systems [9].*

The density of states is known to depend noticeably on the dimension of the system (See Figure 2.9). In a three dimensional solid, the density of states is proportional to the square root of energy ($\sqrt{E}$), in a two dimensional system the density of state is constant, and in a one dimensional solid is inversely proportional to the square root of energy ($1/\sqrt{E}$) [9]. As a result of the one dimensional behavior of single wall carbon nanotube, their density of states shows a singular behavior. These are so-called van Hove singularities.

Generally, the electronic states of carbon nanotubes are related to the electronic bands of graphene. It is clear from section 2.1 that there is a crossing between valence and conduction bands at K point of graphene Brillouin zone. Thus, Mintmire demonstrated that "the DOS near the Fermi level will be directly related to the electronic energy levels of the states near the corners of the Brillouin zone (K point) [20]". Mintmire *et al.* [20] had derived a general equation, which describes the density of states $n(E)$ for one-dimensional electronic bands of single wall carbon nanotube. This universal equation for the density of states of carbon nanotube is given as [5, 20]:

$$n(E) = \frac{8}{q|k_z|} \sum_{m=-\infty}^{\infty} \frac{2}{\sqrt{3}a_0\gamma_0} g(E, E_m) \quad , \tag{2.13}$$

The wave vector along the nanotube axis is $\mathbf{k}_z$. "The function $g(E, E_m)$ is equal to 1 for $E_m = 0$ and $g(E, E_m)$ shows the divergence at $E = E_m$ for $E_m \neq 0$ [5]". a_0 is the lattice constant of carbon nanotube, which is slightly larger than the lattice constant of graphene. This is because the $C - C$ bond length in the case of carbon nanotubes is known to be a little larger than in graphene which is a result from rolling up the graphene sheet. γ_0 is the hopping integral (the interaction between the 2 P_z orbital) [5]. E_m is the quantized energy component along $\mathbf{k}_\perp$ which is related to Δk_m the quantized wave vector component along $\mathbf{k}_\perp$. The quantized energy component is obtained by the following way [5, 20]. First, the electronic energy bands of graphene are approximated "as a straight lines close to K point of the hexagons [5]". According to this approximation, the quantized energy E_m is proportional to the quantized wave vector Δk_m in which $E_m = \frac{\sqrt{3}}{2} a_0 \gamma_0 \Delta k_m$. By inserting the quantized wave vector component Δk_m in E_m, we will obtain the quantized energy component E_m along $\mathbf{k}_\perp$, and it is obtained by the following equation [5, 20]:

$$E_m = \frac{\sqrt{3}}{2} a_0 \gamma_0 \Delta k_m = |3m - n_1 - n_2| \frac{a_0 \gamma_0}{\sqrt{3} d}. \tag{2.14}$$

Obviously from equations (2.14), the quantized energy component E_m is inversely proportional to the diameter of carbon nanotube and directly proportional to the chiral indices n_1 and n_2. Figure 2.10 illustrates the DOS of both chiral and achiral nanotubes of different diameter. The zigzag nanotubes with chirality $(16, 0)$, and achiral $(13, 6)$ and $(21, 20)$ exhibits semiconducting behavior with a gap of approximately 1.1 eV (see Figure 2.10).

In case of the double wall carbon nanotube, the electronic density of states (van Hove singularities) are slightly modified due to the interaction between the inner and external tube [18]. Chen *et al.* [18] analyzed the linear optical properties of double-walled carbon nanotubes within the tight-binding model. They found that due to inter-tube interaction, absorption peaks may be slightly modified. In addition, many different absorption peaks are produced. Figure 2.11 elucidate the electronic density of states of both SWCNTs and DWCNT obtained by Chen *et al.* [18]. It is clear from Figure 2.11 that a new absorption peak appears in the case of DWCNT at $\approx 0.3 - 0.4\ eV$. The absorption peak around 5.8 eV is reduced strongly in the case of DWCNT. All other absorption peaks of the inner and outer tube "can be found in the absorption spectrum of the DWNT only with slightly energy shifted or magnitude modified [18]".

Nanotube interaction

Armchair bundles and isolated SWCNT with chirality (n, n) are expected to be true metals because of the crossing of π and π^* bands at E_F [21]. Ouyang *et al.* observed by using scanning tunnelling spectroscopy measurements that tunnelling spectra showed a gap-like feature at E_F on the bundle armchair tube with chirality (8,8). This gap is not present in spectra of the isolated (8,8) armchair tube (see Figure 2.12). The gap is called a pseudogap and it have energy of $\approx$ 100 meV. The pseudogap is different from

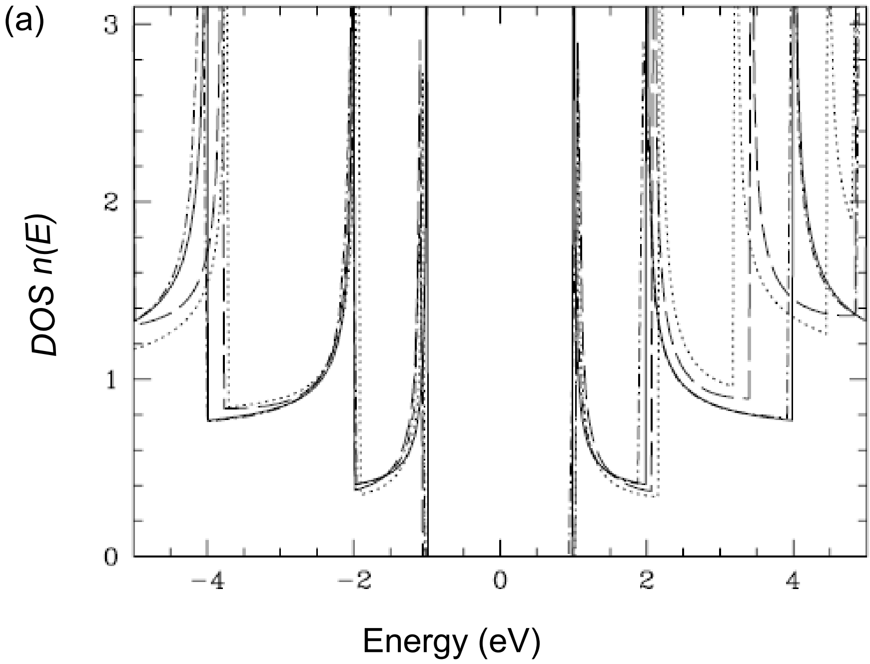

Figure 2.10: *Density of states of the nanotubes (a) for (16, 0) SWNT, dashed line depicts results for (13, 6) SWNT, and dot-dashed line depicts results for (21, 20) SWNT as examples for the density of states of the zig-zag and chiral SWCNTs [20].*

the curvature induced gaps, because the DOS at the Fermi energy E_F are not reduced completely to zero. We can understand the origin of the pseudogap by considering the crossing of π and π^* bands around the Fermi level for isolated and bundle SWCNTs as follows: in an isolated armchair SWCNT, π and π^* bands have different parity under a reflection operation and cross at E_F without opening a gap. On the other hand, in bundle SWCNT when the n-fold rotational symmetry is broken by intertube interactions, the π and π^* bands can mix, which produces a pseudogap at E_F. The gap at the Fermi energy can be open by any small rotation of the (6,6) tubes which breaks the symmetry of the (6,6) bundle. Thus, the intertube interactions are affecting the electronic structure close to the Fermi level, and also are affecting the density of states at larger energies [22]. Figure 2.13 shows the comparison of the DOS calculated for a few isolated and bundled armchair tubes [22]. The intertube interactions induce shifts of the van Hove singularities up to 0.25 eV [23, 24].

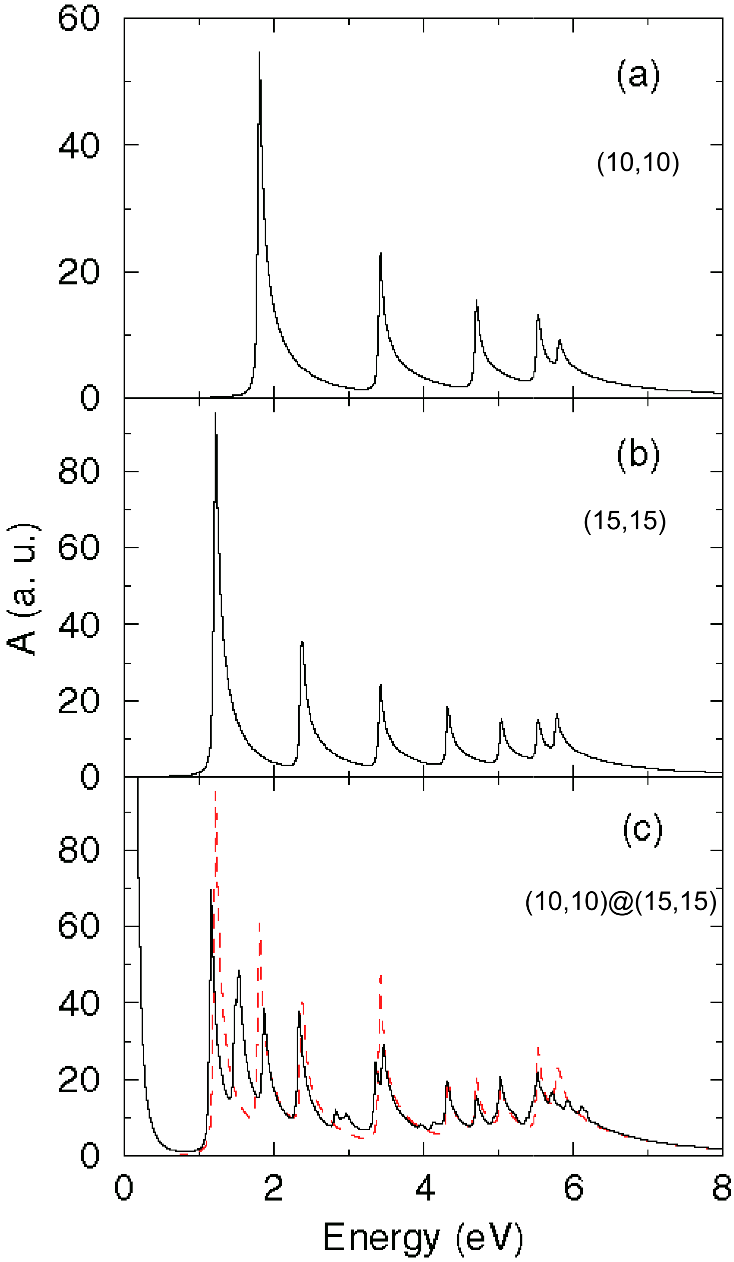

Figure 2.11: *The calculated absorption spectra of nanotubes for (a) (10,10) SWNT, (b) (15,15) SWCNT and (c) (10,10)@(15,15) DWCNT dashed red line depicts results for the simple sum of absorption spectra of the (10, 10) SWNT and (15,15) SWNT [18].*

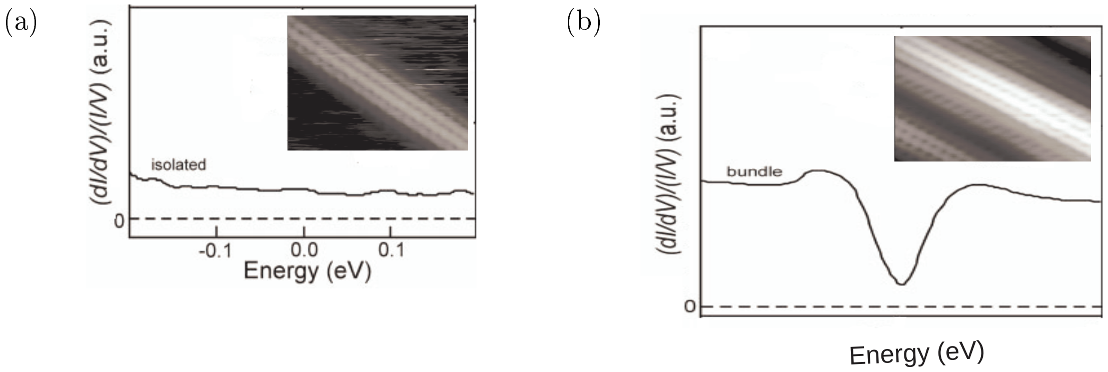

Figure 2.12: *(a)Scanning tunnelling spectroscopy measurements for the isolated armchair nanotube with chirality (8,8), the inset shows STM image of the isolated (8,8) armchair SWCNT. (b) Scanning tunnelling spectroscopy measurements showed a gap-like feature at E_F on the bundle armchair tube with chirality (8,8) the inset shows STM image of the bundled (8,8) armchair SWCNTs [21].*

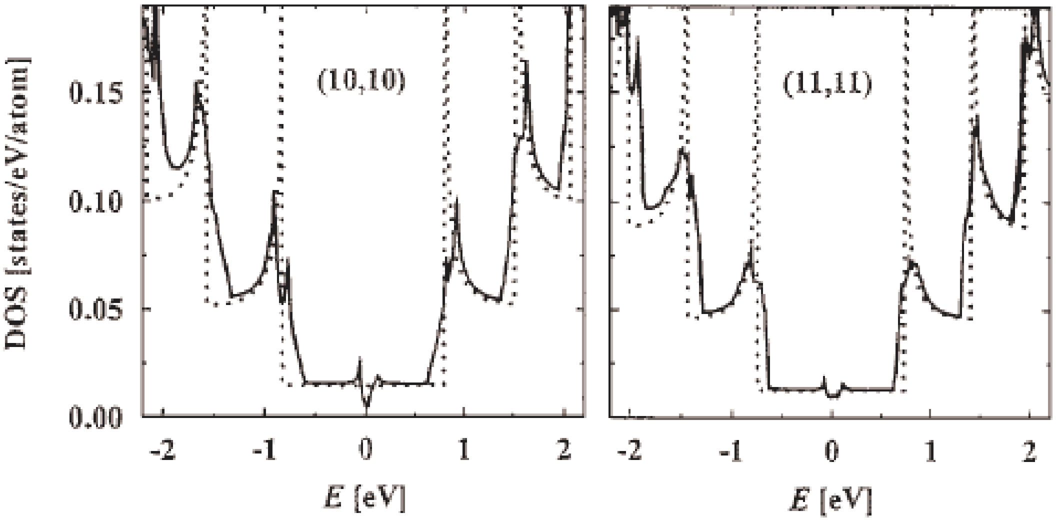

Figure 2.13: *Density of states of isolated (dotted lines) and bundled (solid lines) (10,10) and (11,11) carbon nanotubes. The attenuation, the broadening and the splitting of the vHs as isolated nanotubes bundle up into a close-packed triangular lattice are clearly visible [22].*

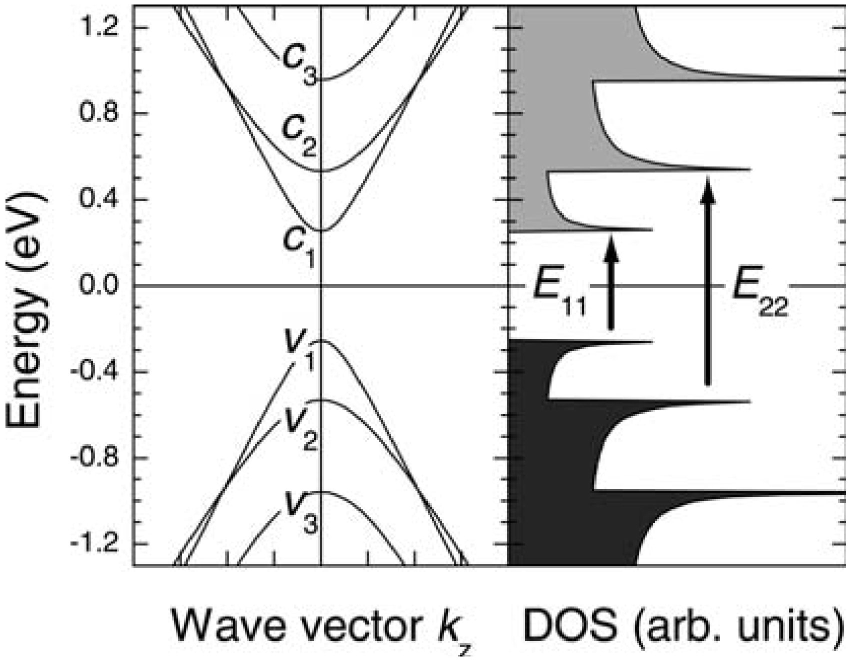

Figure 2.14: *According to selection rules the band to band transition can be mapped onto the energy differences between mirror spikes in the DOS [9].*

2.4 Band-to-Band transitions and selection rules

In general, when a photon of energy $(h\nu)$ excites an electron from the valence into the conduction this is called a band-to-band transition. Experimental study the band-to-band transitions by means of optical spectroscopy provides a convenient way to obtain information about the density of states. Based on the density of states of carbon nanotubes one can explain their optical properties. According to selection rules the measured absorption peaks can be mapped onto the energy differences between mirror spikes in the density of states of carbon nanotubes. By considering the selection rules, one can also understand the allowed transitions between the mirror spike of the vHs of carbon nanotube. There are two cases of the allowed transition. First, the transition in the direction of the tube axis, where the wave vector K_z is continuous. In this case of transition, Reich demonstrated that "the angular momentum quantum number m of the electronic band remains constant according to $\Delta m = 0\ for\ \mathbf{E} \parallel c$ [5,25]". In the other case, the allowed transition is perpendicular to the tube axis, where the allowed wave vector $K_\perp$ is quantized. Reich demonstrated that "the quantum number m must be change by plus or minus 1 according to $\Delta m = \pm 1 \; for \; \mathbf{E} \perp c$ [5]".

Figure 2.14 elucidates the possibly allowed transition between the valence band (V_i) and conduction bands (C_i). According to this figure, the first allowed transition between the mirror spike of the density of states is a transition from the first van-Hove singularity of the valence band V_1 to the first singularity of the conduction band C_1. The corresponding energy related to this transition is E_{11}. The second allowed transition is $V_2 \rightarrow C_2$ with the optical transition at E_{22}. In the optical measurements, the first and second optical transition are depending on the diameter distribution of carbon nanotubes. The third allowed transition is between V_3 to C_3 at energy E_{33} (see Figure 2.14) [5,9].

By plotting the energies of the optical transition as a function of the tube diameter, one obtains the very known Kataura plot, as we will see next. The optical absorption bands perpendicular to the tube axis is suppressed by the depolarization as a result of the selection rules [5,9,26]. "For an external electric field parallel to the tube axis, there is no induced polarization and the total parallel electric field is equal to the external field. Perpendicular to the tube axis the electric field is reduced due to the polarization [5]". The effect of the depolarization field on the optical conductivity perpendicular to tubes axis is illustrated in Figure 2.15. The optical conductivity for polarization parallel to the tube axis consists of the optical absorption expected according to the selection rules without much influence of the depolarization effect. The optical transitions are totally screened out for perpendicular polarization when the depolarization effect is taken into account. "Figure 2.15 (b) shows a picture of a nanotube grown inside a zeolite crystal taken with polarized light perpendicular and parallel to the tube axis [5]". It is clear from this picture that the lower part seems dark, because the absorption is large, and all the light is absorbed. It is also clear that there is only small absorption in the upper part, because the electric field perpendicular to the tube axis is reduced due to the polarization.

Kataura Plot: Trigonal warping effect

The optical properties of carbon nanotube can be explain based on the density of states. According to selection rules the measured absorption peaks can be mapped onto the energy differences between mirror spikes in the DOS. The energy difference depends on the nanotube diameter as shown in the Kataura plot (see Figure 2.16 (i)) [27]. Kataura also showed that there is a variety in energy for a fixed diameter due to different chirality. This spread is large for absorption bands at higher energies; for example; the spread for the M_{11} optical transition is larger than for the S_{11} optical transition. Kataura and co-workers used the tight-binding approximation to calculate the energy differences between the mirror spikes *ith* of vHs peaks in the valence and

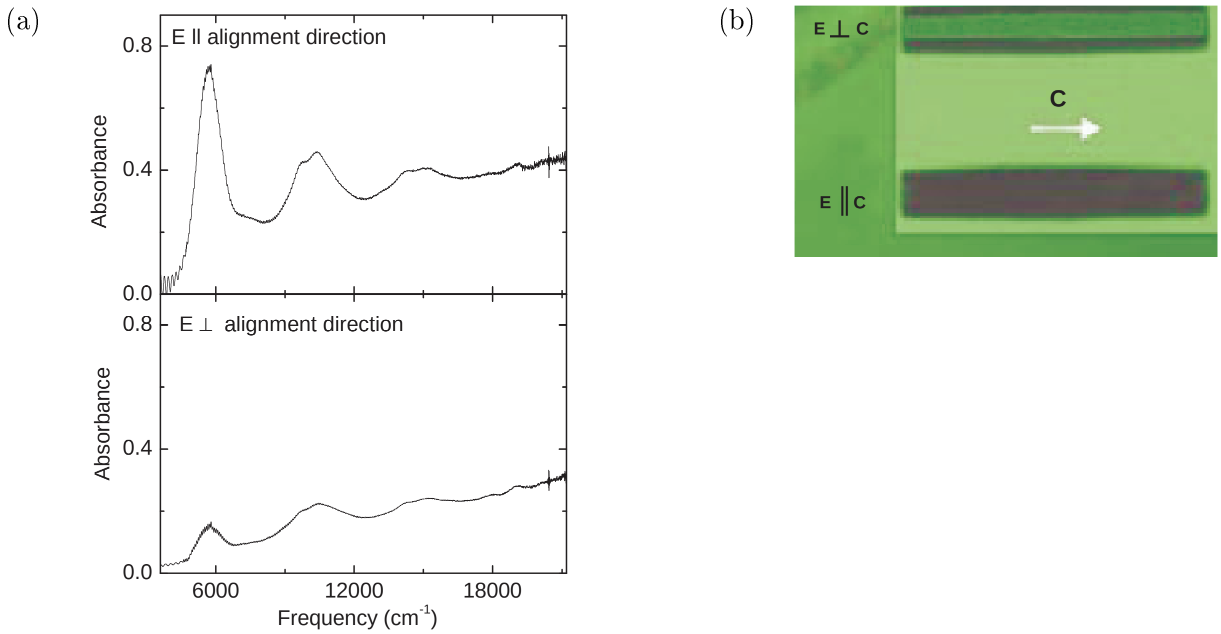

Figure 2.15: *(a) Typical near-infrared and visible absorbance spectra for* **E**$\|$ *tube axis is unaffected by the depolarization effect while that for* **E**$\perp$*tube axis is strongly modified. (b)Transmission through a small nanotube with the electric field vector perpendicular (upper) and parallel (lower) to the tube axis [26].*

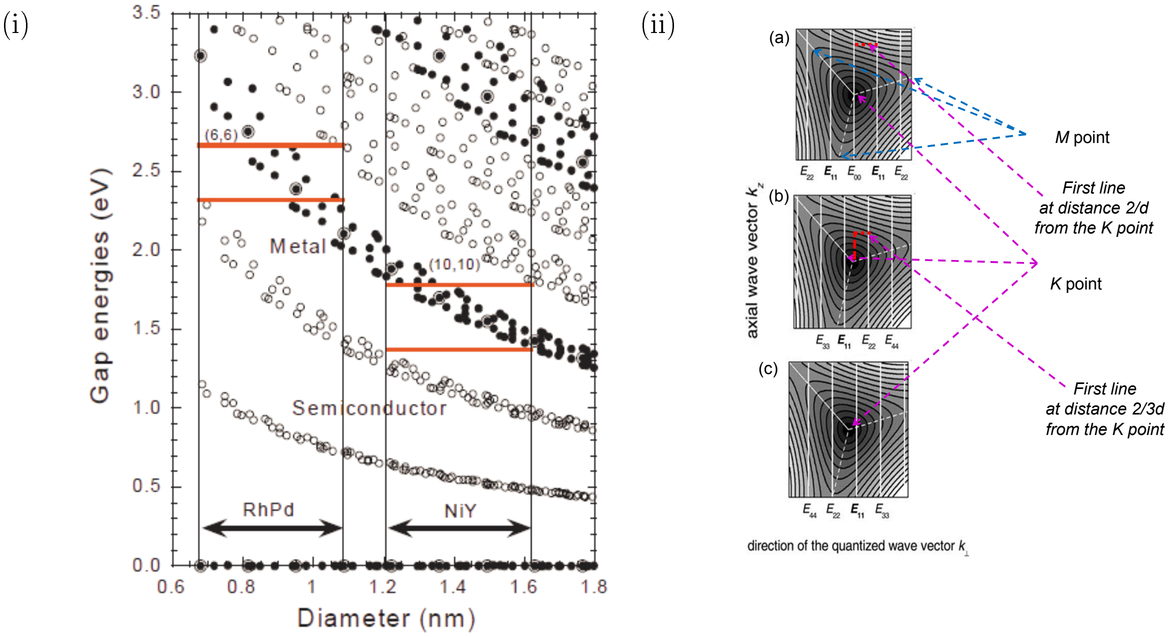

Figure 2.16: *(i)Energy separation for all (n_1, n_2) calculated for SWCNTs of diameters up to 3 nm. The black and red lines correspond to semiconducting and metallic nanotubes, respectively [27].(ii) Allowed wavevectors for the three nanotube. (a) Metallic nanotube, (b) Semiconducting tube with large band gap, and (c) Semiconducting tube with small band gap [5, 9, 13].*

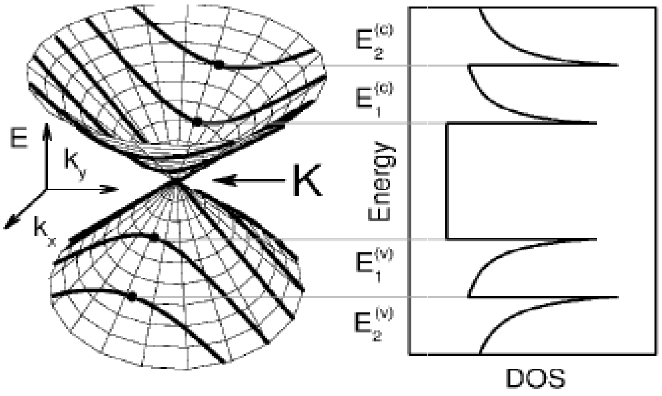

Figure 2.17: *An illustration of the density of states of carbon nanotubes based on cutting the two dimensional electronic dispersion relations of graphene [28].*

conduction bands counted from the Fermi energy, E_{ii}, as a function of the diameter d of carbon nanotube for all chiral angles at a given d value [27] (see Figure 2.16 (i)).

Kataura showed that, for a fixed diameter, the energy differences among the vHs peaks E_{ii} have a width in the energy and that this width increases with increasing energy relative to the Fermi energy [27]. It was also observed by Kataura that, at constant diameter, this width of the peak positions of the vHs was consistent with the experimental width of the peaks in the resonant Raman spectra for single-wall carbon nanotube samples and with the optical absorption spectra. Saito examined the Kataura plot in detail in order to understand the noticeable width in the peak positions of the Kataura plot. He found that the peak positions of the vHs is depending on the nanotube chirality. As a result of that, the width of the peak positions was showed by the presumed trigonal warping effect of the electronic energy states, by which way equi-energy contours in the hexagons around the K points change from circles to a triangular shape.

The energy contour lines around the K point of the hexagons are only circular for small values of wave vector $\mathbf{k}$. For large $\mathbf{k}$ values, they become nearly triangular connecting the three M points nearest to the K point (see Figure 2.16 (ii)) leading to the so called trigonal warping effect [15]. Saito demonstrated that "trigonal warping effects split the vHs peaks in the $1D$ density of states for metallic nanotubes, which come from the two nearest possible $\mathbf{K}_\perp$ vectors near the K point [15]".

The allowed wavevector lines of a metallic and two semiconducting tubes close to the K point of graphene are shown in Figure 2.16 (ii) from (a-c), respectively. The optical transitions in the near infrared and the visible are based on the electronic energies in the vicinity of K point of graphene. According to Section 2.3, within the zone folding approximation the nanotubes are metallic, if the graphene K point is among the allowed states of a carbon nanotube. The allowed wavevector lines around the K point of garphene give the energy positions of the van Hove singularities of carbon nanotubes [15, 28, 29] (See Figure 2.17). Since the measured absorption peaks can be mapped onto the energy differences between mirror spikes in the van Hove singularities. Therefore, the origin of the M_{11} optical transition is the two neighboring lines near the K point, which are at a distance of $2/d$ from the K point (see Figure 2.16 (ii) (a)). The first allowed line, in a semiconducting tube, is at a distance $2/3d$ from K point which is origin of the (S_{11}) optical transition. The second optical transition of semiconducting nanotube is (S_{22}), the third optical transition of semiconducting nanotube (S_{33}), and by similar way for all other optical transition. Because the energy dispersion relation of graphene close to the K point is approximately linear, the energy of the optical transitions will be order as the following S_{11}, S_{22}, M_{11}, S_{33}.

The trigonal warping of the graphene band structure around the K points describes the changes in the energy values of the optical transition at fixed diameter (see Figure 2.16 (i)). Reich and Saito *et al.* [13, 15] have presented a detailed analysis of electronic band structure of CNT with different chiralities. They have come to the conclusion that the energies of the optical transitions depend on the tube chirality as well on tube diameter [5, 9, 13, 15]. Figure 2.16 (ii) from (a-c) illustrates the trigonal warping around the K points of the graphene Brillouin zone. The contour lines are expected to be circles without trigonal warping effect.

2.5 Single-walled, C_{60} peapods and double-walled carbon nanotubes under pressure

Recently detailed pressure-dependent investigations on single-walled carbon nanotubes (SWCNTs), C_{60} peapods and double-walled carbon nanotubes films were performed to address pressure-induced phenomena such as structural phase transition [3, 30–33]. Vibrational spectroscopy, in particular, Raman spectroscopy is an important and convenient tool for studying pressure-induced structural phase transitions [30]. It is widely used in addition to X-ray scattering [34] and optical absorption spectroscopy [3]. Also, many theoretical studies predicted a structural phase transition, where the nanotubes cross section is strongly deformed from the circular to an oval shape [31, 35]. The radial deformation of carbon nanotubes under hydrostatic pressure is followed by the collapse which occurs at a critical pressure P_c, where P_c is inversely proportional to the diameter of the carbon nanotube i.e., $P_c \propto 1/d^3$, for individual [35] and bundled [31] SWCNTs (see Figure 2.18).

Both molecular dynamics analysis and ab-initio calculations predict that the circular cross-section of nanotubes deforms by applying pressure to oval, elliptical, racetrack-like or peanut-shaped cross-section [31, 36–41]. The molecular dynamics calculations showed a strong dependence of P_C on nanotube diameter, but a weak dependence of P_C on nanotube helicity. The similar ranges of P_C are ≈ 6-2.5 GPa for SWCNTs with d ≈ 0.7-1.4 nm, as stated by Capaz *et al.* [41]. The circular-to-oval structural transition was predicted by Reich *et al.* [36] for SWCNTs with d ≈ 0.8 nm at 9-15 GPa, depending on nanotube helicity. A similar circular-to-oval structural transition in a bundle of (10,10) tubes d=1.36 nm was observed by Chan *et al.* [37] at $P_C \approx 2.7$ GPa. The hexagonal deformation of the triangular lattice packing was found by Sluiter *et al.* [38] in bundled nanotubes. Collapsed SWCNTs in bundles may form covalent intertube connection under exceedingly high pressure [36,37]. The electronic structure of nanotubes is highly sensitive to radial distortion according to ab initio calculations of Gülseren *et al.* [42] for individual and Okada *et al.* [43] for bundles SWCNTs. Gülseren *et al.* [42] showed that a semiconducting tube can transform into a metallic one by oval deformation. As a result, dramatic changes in electronic and optical properties of carbon nanotubes are expected.

Experimentally, a large variety of SWCNTs samples including as-prepared, nearly defect SWNCTs and highly defect SWNCTs generated by oxidative purification, have been studied by several tools, for example, Raman spectroscopy [30, 44], X-ray scattering [34, 45] and optical absorption [3, 46]. It is expected that a wide spread of experimental results is related to variations in the preparation technique and structure of the samples. In this way, Tang *et al.* [45] gave a description of the decay of the x-ray diffraction peak (the hexagonal close-packed structure peak of bundled carbon nanotubes) for as-prepared SWCNTs at ≈ 1.6 GPa. The author attributed the observed anomaly around 1.6 GPa to "the structural distortions which occurred to the raft-like bundles, and the deformation is still elastic up to 4 GPa [45]". Sharma *et al.* [34] has observed the hexagonal close-packed structure peak of the carbon nanotubes up to 10 GPa for chemically treated SWCNTs. Some Raman studies of as-prepared SWCNTs with d ≈ 1-1.4 nm described of a disappearance of the radial-breathing mode (RBM) band and a change in the pressure derivative of the G band frequency at 1.52 GPa, which was assigned to the hexagonal [31, 47] or oval [48] cross section deformation. On the other hand, Teredesai *et al.* [49] observed the RBM bands of purified SWCNTs with similar diameters up to 4 GPa. Venkateswaran *et al.* [50] discussed the possibility of a structural transition at ≈ 2 GPa in order to explain a drop of the RBM inten-

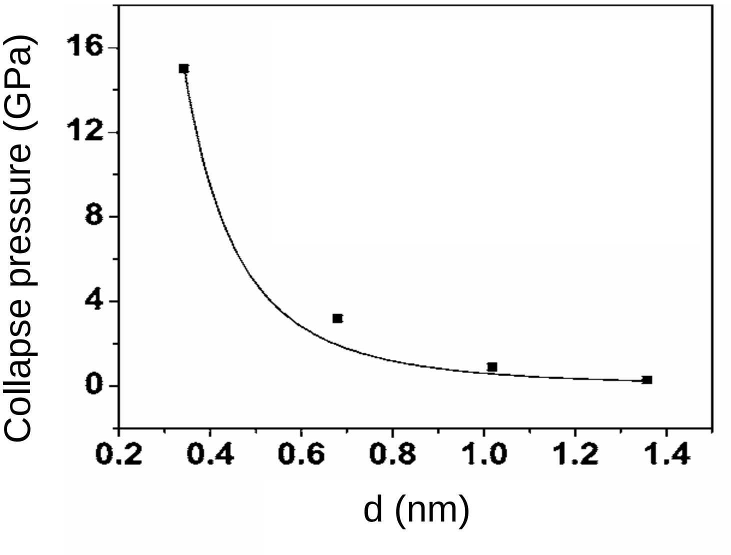

Figure 2.18: *Collapse pressure of SWCNTs bundles as a function of the tube diameter [32].*

sity observed there. Venkateswaran *et al.* [50] illustrated that the intensity of radial breathing mode and tangential mode is suddenly dropped around 2 GPa, indicative of a phase transition, despite the persistent of the radial breathing mode and tangential mode to higher pressures.

Clearly, there are discrepancies between experimental results, which were carried out under pressure. "These discrepancies were attributed to the intercalation of the pressure transmitting medium [51–53]". Merlen *et al.* [53] explained that the pressure transmitting medium can fill the nanotubes, which were opened by some purification procedure, and thus stop a large deformation and collapse of the nanotubes. For that reason, the role of the pressure transmitting medium in the pressure studies is not clear at present. In order to address the role of the pressure media, pressure-dependent investigations on the unoriented SWCNTs and oriented SWCNTs have been performed in the near infrared and visible frequency range to study the effect of the different pressure media. In this project we used different pressure transmitting media with different hydrostaticity (helium, argon CsI and alcohol mixture) to see the effect of hydrostaticity on SWCNTs.

Gadagkar *et al.* [32] have performed a set of molecular dynamics simulations in order to investigate the behavior of DWCNTs under pressure. They focused mainly on the response of the inner and the outer tubes. "The molecular dynamics simulations were carried out on four SWCNTs (5,5), (10,10), (15,15), and (20,20), and four DWCNT, (5,5)@(10,10), (7,7)@(12,12), (10,10)@(15,15), and (15,15)@(20,20) bundles [32]". Gadagkar *et.al* studied the collapse of single SWCNTs and DWCNT carbon nanotube bundles under hydrostatic pressure. They observed that the collapse pressure P_c varies as $1/d_{ref}^3$, in which d_{ref} is the effective radius of the DWCNTs . The effective radius of the DWCNTs is given by the following equation.

$$\frac{1}{d_{ref}^3} = (\frac{1}{2}\sum_{i=1}^{2}\frac{1}{d_i^3}) \tag{2.15}$$

P_c of DWCNTs is found to be inversely proportional to effective radius d_{ref} of the DWCNTs [32]. Experimentally, Raman spectroscopy were used extensively to study bundles of DWCNTs under hydrostatic pressure [4,54–56]. The authors concluded that the inner-tube inside the outer-tube is highly defect-free and unperturbed, where the inner tube provides structural support to the outer tube, and the outer tube shields the inner tube from applying the external pressure. Furthermore, the changes in the line width of the radial breathing mode of the empty nanotubes and the C_{70} peapods (C_{70} encapsulated single wall carbon nanotubes) under hydrostatic pressure were experimentally investigated by Raman spectroscopy [57]. Caillier *et al.* investigated the behavior of bundled C_{70} peapods by Raman spectroscopy and compared with the corresponding behavior of the non-filled SWCNTs under hydrostatic pressure. He observed that there is weak interaction below 2 GPa between the C_{70} and the nanotube. Furthermore, Rafailov *et al.* [33] presented Raman spectra of C_{60} peapods and C_{70} peapods (C_{60} encapsulated in single-wall carbon nanotubes) at different excitation wavelengths under hydrostatic pressure. The author concluded that a pressure shielding of C_{70} inside the tubes is observed "with an abrupt change in the slope for the C_{70} modes at 1.5 GPa [33]".

Arvanitidis *et al.* [54] investigated the effect of the hydrostatic pressure on the double wall carbon nanotube using alcohol mixture as a pressure transmitting medium. Obviously from Figure 2.20, the intensity of the radial breathing modes and the tangential band of the outer tubes remain detectable up to 10 GPa. On the other hand, the intensity of the radial breathing modes and the tangential band of the internal tubes is less sensitive to the application of pressure up to 10 GPa. Arvanitidis *et al.* [54] showed that the outer tubes shields the inner tubes, whereas the inner tube support the outer tubes against the increasing pressure.

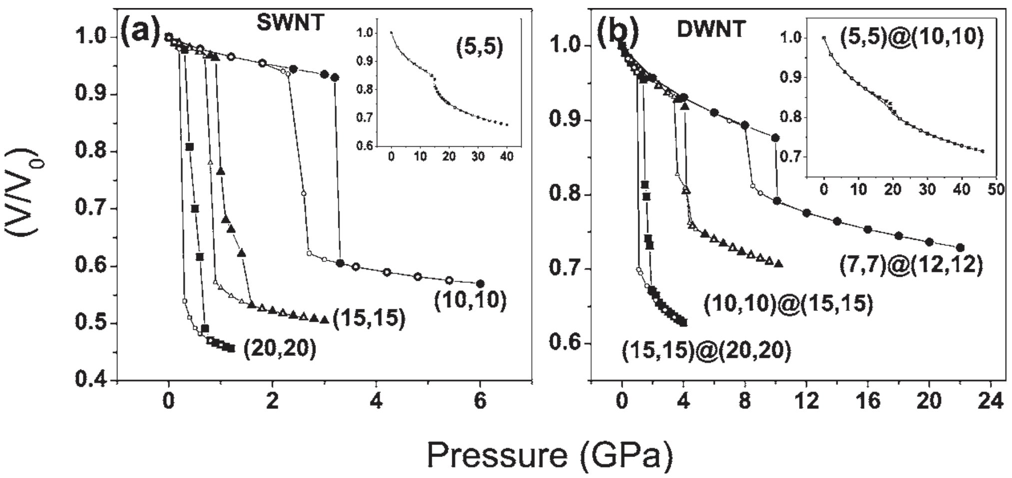

Figure 2.19: *The pressure dependence of the normalized nanotube volume for different tube diameter. The abrupt reduction of the volume corresponds to the collapse of a tube. Insets show the same data in the extended pressure range [32].*

Another study used both experimental Raman measurement and theoretical calculation to investigate the stability of double wall carbon nanotubes under hydrostatic pressures up to 10 GPa [55]. Puech *et al.* [55] showed that the tangential mode of the outer tube is more sensitive to the application of pressure comparing to the tangential mode of the inner tube as illustrated in the Figure 2.21. It is clear from this figure that the changing in the slope of the tangential mode of the outer tube is the same like in case of single wall carbon nanotube in contrast with the inner tube where the slope of this mode remains constant with application of pressure. Basing on these observations they have concluded that "the outer tubes act as a protection shield for the inner tubes [55]".

Beside studying the role of the pressure transmitting media on SWCNTs, we studied the effect of high-pressure on DWCNTs by Infrared spectroscopy to examine their structural stability and compare it with that of SWCNTs and C_{60} peapods. We also studied the role of the pressure transmitting media on the DWCNTs.

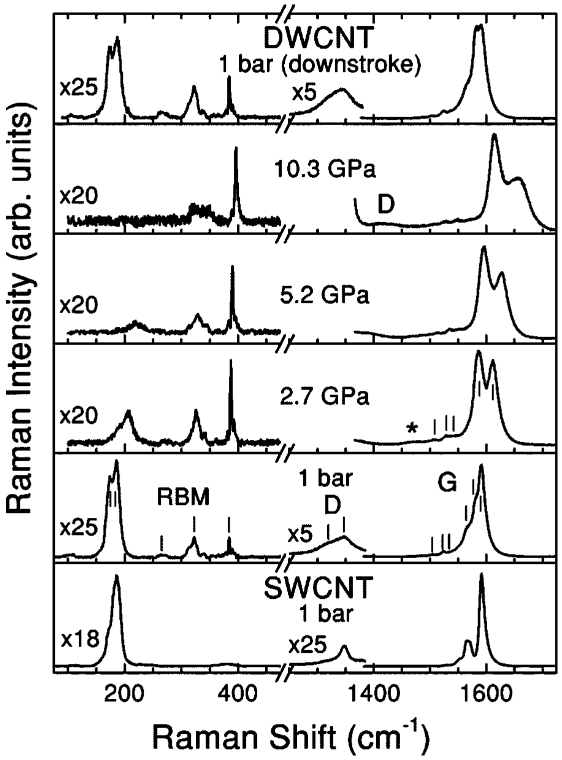

Figure 2.20: *Raman spectra of the double wall carbon nanotube as a function of pressure and using alcohol mixture as a pressure transmitting medium [54].*

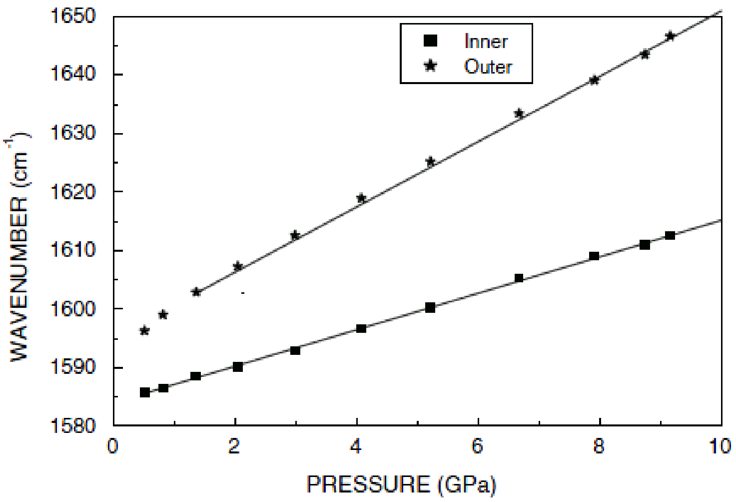

Figure 2.21: *Frequencies of the tangential modes for the inner and outer tube as a function of pressure [55].*

3 Experimental Techniques

The main issues we want to address by the pressure-dependent infrared studies are:

1. The role of the pressure transmitting medium in single-walled carbon nanotubes (SWCNTs), peapods (C_{60} encapsulated SWCNTs) and double-walled carbon nanotubes (DWCNTs).
2. High pressure studies will enable us to observe closely and investigate effectively the electronic properties of carbon nanotube under extreme stress conditions.
3. The influence of the pressure transmitting media regarding the pressure-induced effects in SWCNTs.
4. Optical spectroscopy and high pressure techniques provide further information by studying the induced interband transitions.
5. The analysis of the induced interband transitions allows conclusions about the band structure of the studied material.

In order to achieve these goals, (i) I used a Fourier transform Infrared (FTIR) spectrometer (Bruker IFS66v/S) coupled to an infrared (IR) microscope in order to perform the infrared measurements under pressure (see Section 3.2 for more details). (ii) I used the following pressure transmitting media(see Subsection 3.3.4):

- Finely ground CsI powder.
- 4:1 methanol-ethanol alcohol mixture.
- Cryogenic liquified argon.
- Liquid helium.

(iii) For the generation of pressures, I used two types of diamond anvils cells (DACs) as follows and for more details see Section 3.3:

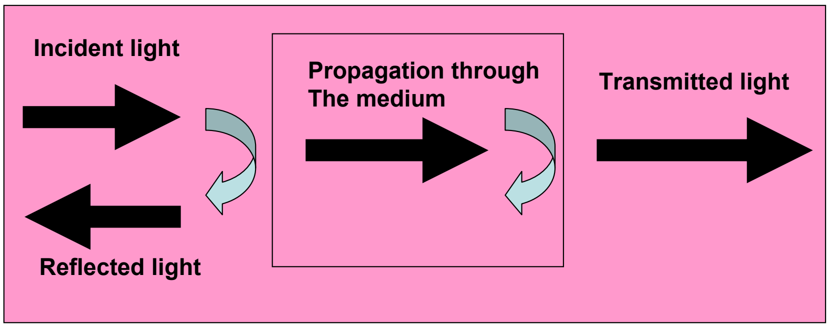

Figure 3.1: *Reflected light, transmitted light and propagated light beam incident on an optical medium [59]*

1. **Syassen-Holzapfel cell [58] cell**
2. **a clamped cryoDAC Mega by *Easylab* company.**

(iv) I used the following setup for filling the two pressure cells with the liquids pressure medium (see Subsection 3.3.4).

1. **I used cryogenic filling setup for filling the Syassen-Holzapfel type DAC with argon [2].**
2. **For filling the Syassen-Holzapfel type DAC with helium I used commercial glass cryostat.**

In order to determine the pressure inside the pressure cells, the ruby luminescence method were used within this project.

3.1 Optical coefficients

The optical processes can be described by a set of parameters that determine the properties of the medium. The reflectivity or transmission is described in terms of a frequency-dependent complex dielectric function $\epsilon(\omega)$**. The analysis of the measured data is then performed by fitting the spectra with Drude-Lorentz model of the measured data. In this section, the physical quantities that can be obtained from the infrared spectroscopic measurements are described briefly. The definitions of many different optical response functions are also presented in this section. See Ref. [59–61]**

for more detailed information on the first two subsections. Figure 3.1 shows the interaction of a light beam incident on an optical medium.

3.1.1 The complex refractive index and dielectric constant

The refractive index n describes the propagation of light through a transparent medium. The refractive index depends on the frequency of light and is defined as the velocity of light in free space c divided by the speed of light in the medium v. The refractive index is a complex quantity ($\tilde{n} = n + i\kappa$), where n and κ perform the refractive index and extinction coefficient of the material. The absorption coefficient α is directly related to extinction coefficient κ. The relationship between α and κ can be derived by considering the propagation of the waves through a medium with a complex refractive index. When the refractive index is known, it is possible to determine the complex dielectric constant ($\tilde{\epsilon} = \epsilon_1 + i\epsilon_2$) which is related to the refractive index as $\tilde{\epsilon} = \tilde{n}^2$. From these relations, the real and imaginary parts of the dielectric constant can be described by $\epsilon_1 = n^2 - \kappa^2$ and $\epsilon_2 = 2n\kappa$ respectively. The reflectivity R of a material is related to the refractive index by Fresnel equation as:

$$R = \frac{(n-1)^2 + \kappa^2}{(n+1)^2 + \kappa^2} \quad . \tag{3.1}$$

The transmittance is related to the complex refractive index and dielectric function. The transmittance of the material is then given by the expression.

$$T = \frac{[(1-R)^2 + 4R\sin(\phi)^2]e^{-\alpha d}}{(1-Re^{-\alpha d})^2 + 4Re^{-\alpha d}\sin(\beta+\phi)^2} \quad , \tag{3.2}$$

where α is the power absorption coefficient given by $4\pi \mathrm{k}/\lambda_0$ (λ_0 is the wavelength in vacuum), d is the thickness of the material, and β and ϕ are the phase change upon passing through the material and reflection, respectively. Experimentally, the intensity of light transmitted through the sample is divided to the intensity of light without the sample. In case of the reflectivity measurements, the intensity of light reflected from the sample is divided by the intensity of light reflected from a reference mirror (aluminium or sliver mirror).

3.1.2 Drude-Lorentz model

Experimental observations show that many materials demonstrate a number of resonant absorption bands. We can observe such natural resonance in reflectivity or transmittance measurements. The frequency-dependent dielectric constant of the Lorentz

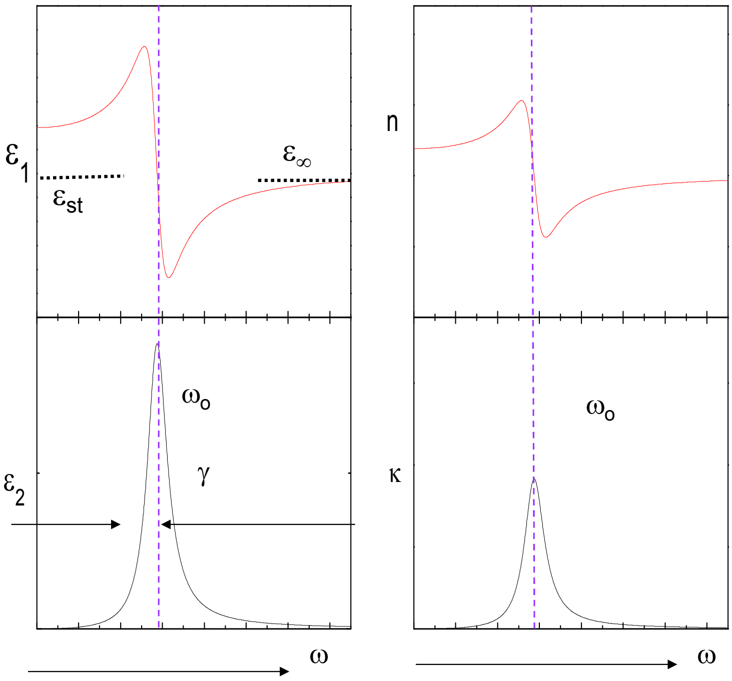

Figure 3.2: *(a) Frequency dependence of the real ϵ_1 and imaginary ϵ_2 parts of the dielectric constant at frequencies close to resonance [59]. (b) Frequency dependence of the real and imaginary parts of the refractive index calculated from the dielectric constant [59].*

model can be written as

$$\epsilon_1(\omega) = 1 + \frac{Ne^2}{\epsilon_0 m_0} \frac{\omega_0^2 - \omega^2}{(\omega_0^2 - \omega^2)^2 + (\gamma\omega)^2} \tag{3.3}$$

$$\epsilon_2(\omega) = \frac{Ne^2}{\epsilon_0 m_0} \frac{\gamma\omega}{(\omega_0^2 - \omega^2)^2 + (\gamma\omega)^2} \tag{3.4}$$

where γ is the damping due to energy loss mechanisms, ω is the frequency of the incident radiation, and ω_0 is the resonance frequency of the excitation, N is the number of charge carriers, and m_0 is the free electron mass. We can obtain the Drude model directly from the Lorentz model by taking the restoring force ω_0 to zero. The Drude model is obtained from the following equation.

$$\epsilon_1 = 1 - \frac{Ne^2}{\epsilon_0 m_0} \frac{1}{(\omega^2 + \gamma^2)} \tag{3.5}$$

The real and imaginary parts of the dielectric function described by Lorentz model are shown in Figure 3.2(a). Figure 3.2 (b) shows the real and imaginary parts of the refractive index.

3.2 Fourier transform infrared spectroscopy

Optical spectroscopy provides further information by studying the induced interband transitions on single-walled carbon nanotubes (SWCNTs), peapods (C_{60} encapsulated SWCNTs) and double-walled carbon nanotubes (DWCNTs). The analysis of the induced interband transitions allows conclusions about the band structure of the studied material. I used a Fourier transform Infrared (FTIR) spectrometer (Bruker IFS66v/S) coupled to an infrared (IR) microscope within this project in order to perform the infrared measurements under pressure.

3.2.1 How does an interferometer work?

The interferometer main purpose is to divide the infrared beam into two beams, and make one of the infrared beam moves a different distance than the other. The optical path difference δ is defined as the difference in distance traveled by these two infrared beams. Figure 3.3 shows a diagram of the Michelson interferometer. It is clear from this figure that the Michelson interferometer holds four arms. The arm number one is the infrared source of light; the arm number two is a fixed mirror; the arm number three holds a moving mirror; and the arm number four is open. The infrared beam is divided into two beams by using the so-called beamsplitter, which is at the intersection of the four arms. The beamsplitter is constructed to reflect half of the infrared beam that impinges upon it, and transmit half of the infrared beam. The infrared beam that strikes the detector is therefore the sum of these two infrared beams. If the fixed mirror and the moving mirror are exactly the same distance from the beamsplitter, the distance moved by the infrared beams that reflect off the fixed mirror and the moving mirror is also the same. If the fixed mirror and the moving mirror are exactly the same distance from the beamsplitter, this particular state is known as zero path difference (ZPD). The optical path difference (δ) between the two infrared beams is obtained by translating the moving mirror away from the beamsplitter in the Michelson interferometer.

Let us consider three different infrared beams with different wavelengths λ_1, λ_2 and λ_3 strikes the interferometer shown in Figure 3.3. We will see that the three

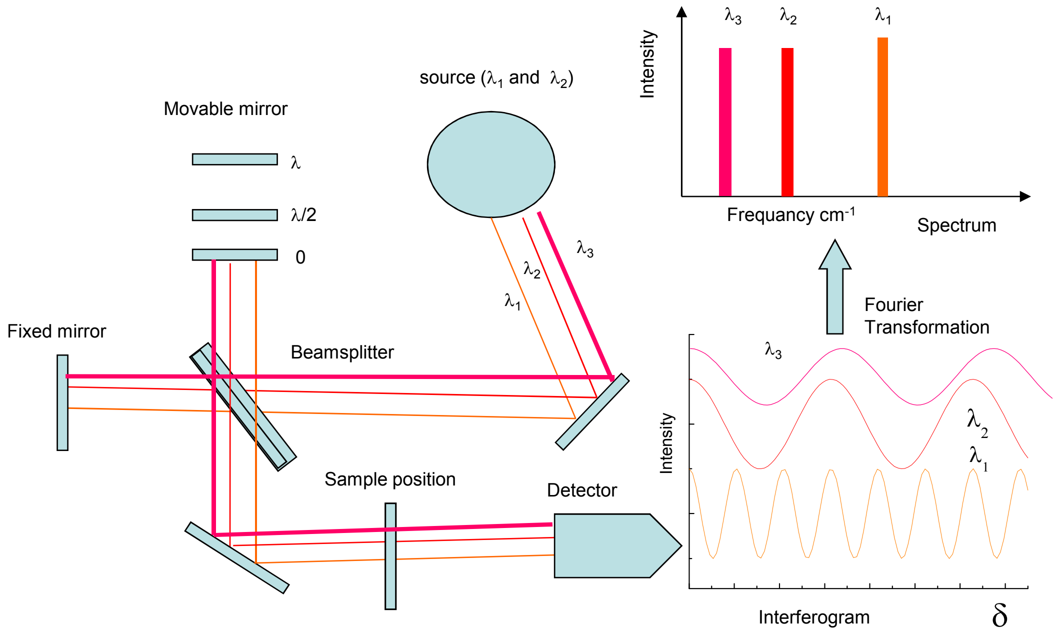

Figure 3.3: *A optical diagram of a Michelson interferometer explaining the working principle of an FTIR spectrometer. The moving mirror in the interferometer is the only continuously moving part in the instrument.*

infrared beams undergo destructive interference when $\delta = [n + \frac{1}{2}\lambda]$ and constructive interference when $\delta = n\lambda$, in which λ can be λ_1 or λ_2 or λ_3. It is clear from Figure 3.3 that the three infrared beams of wavelengths λ_1, λ_2 and λ_3 are totally different with different optical path differences and undergo constructive and destructive interference at different δ. As a result, the interferograms of the three infrared beams will be different (see Figure 3.4). This is how the signals due to different wavenumbers of light are distinguished by the spectrometer. In general, constructive interference take place for any value of δ where the two light beams are in phase. (i.e., $\delta = n\lambda$; n=0,±1,±2, etc.,). The destructive interference occur when λ is half wavelengths (*i.e.*, $\delta = [n+\frac{1}{2}\lambda]$). Both of these interferograms are cosine, but their frequencies are different. Therefore, the interferogram can be described as an infinitely long cosine wave defined by:

$$I(\delta) = B(\nu)cos(2\pi\delta\nu) \tag{3.6}$$

where I(δ) is the intensity "of the detector signal as a function of optical path difference and [2]" $B(\nu)$ is the intensity of the source as a function of frequency ν given in cm^{-1}.

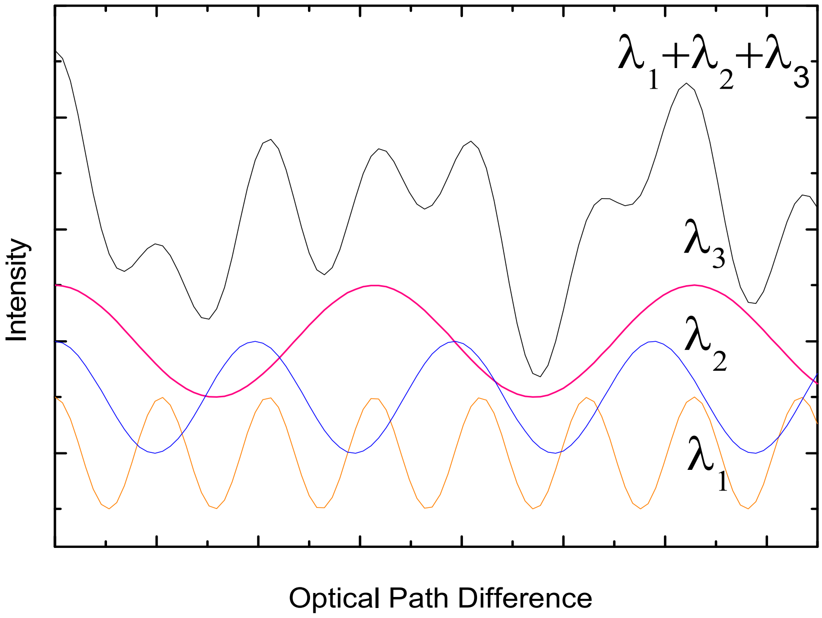

Figure 3.4: *The interferogram of light as wavelength* λ_1*,* λ_2 *and* λ_3 *and the sum of the three interferograms.*

Let us change the three infrared beams λ_1, λ_2 and λ_3 in the interferometer with a broadband infrared source. It is possible, to treat each frequency as a result of a cosine function with its own periodicity, and the whole interferogram measured by the detector is the summation of all the interferograms from all the different wavelengths. The intensity as a function of the path difference in the interferogram can be defined as,

$$I(\delta) = \sum_{\nu_1}^{\nu_n} B(\nu_i)\cos(2\pi\delta\nu_i) \tag{3.7}$$

"A typical infrared source emits a continuous spectrum and therefore we can replace the summation by an integral [2]",

$$I(\delta) = \int_0^{\infty} B(\nu)\cos(2\pi\delta\nu)d\nu \tag{3.8}$$

The Fourier transform calculates the infrared spectrum from the interferogram.

$$B(\nu) = \int_0^{\infty} I(\delta)\cos(2\pi\delta\nu)d\delta \tag{3.9}$$

Frequency range	Radiation source	Beamsplitter	Polarizer	Detector
Farinfrared 30 - 700 cm^{-1}	Mercury lamp	50 μm Mylar/Ge 23 μm 6 μm	Polyethylene	Si bolometer 4.2 K DTGS
Midinfrared 500 - 8000 cm^{-1}	Globar	KBr/Ge	KRS-5	MCT detector DTGS
Nearinfrared 2000 - 12000 cm^{-1}	Tungsten lamp	CaF_2	KRS-5	InSb detector
Visible/UV 10000 - 30000 cm^{-1}	Tungsten lamp	CaF_2	Prism	Si diode GaP diode

Table 3.1: *Different radiation source, beamsplitters, polarizers and detectors used for various frequency ranges for the infrared measurements using the Fourier transform spectrometer.*

Figure 3.5 shows a typical interferogram and the corresponding spectrum. The interferogram in Figure 3.5 illustrates a sharp intensity at zero optical path difference ($\delta = 0$), which is called the centerburst. The interferogram in Figure 3.5 shows also low intensity at higher optical path differences in the wings of interferogram. At zero path difference all infrared wavelengths undergo constructive interference, and this is the reason of the high intensity of the centerburst. As a results of the changes of the optical path difference all sinusoidal waves of different infrared frequency get out of phase with each other and undergo destructive interference. In an FTIR spectrum the random noise is reduced by adding the interferograms together and the signal-to-noise ratio is improved.

Fourier transform infrared (FTIR) spectrometers enable significantly higher signal-to-noise ratio compared to dispersive instruments. In a FTIR spectrometer the complete spectrum of the infrared radiation propagates through a sample and strikes the detector within a single measurement event. In contrast to a grating spectrometer there are no slits. In the dispersive spectrometer, the slit is selecting a narrow spectral component of the infrared radiation therefore, the intensity of the light, which reaches to the detector is dramatically reduced.

3.2.2 Fourier transform infrared spectrometer

The standard instrument includes the following parts: (i) the infrared beam source; (ii) the Michelson interferometer; (iii) the sample; (iv) the three different detectors; and(vi) the computer. Within this project, the infrared measurements were done using the FTIR spectrometer (Bruker IFS66v/S). Figure 3.6 shows the optical layout

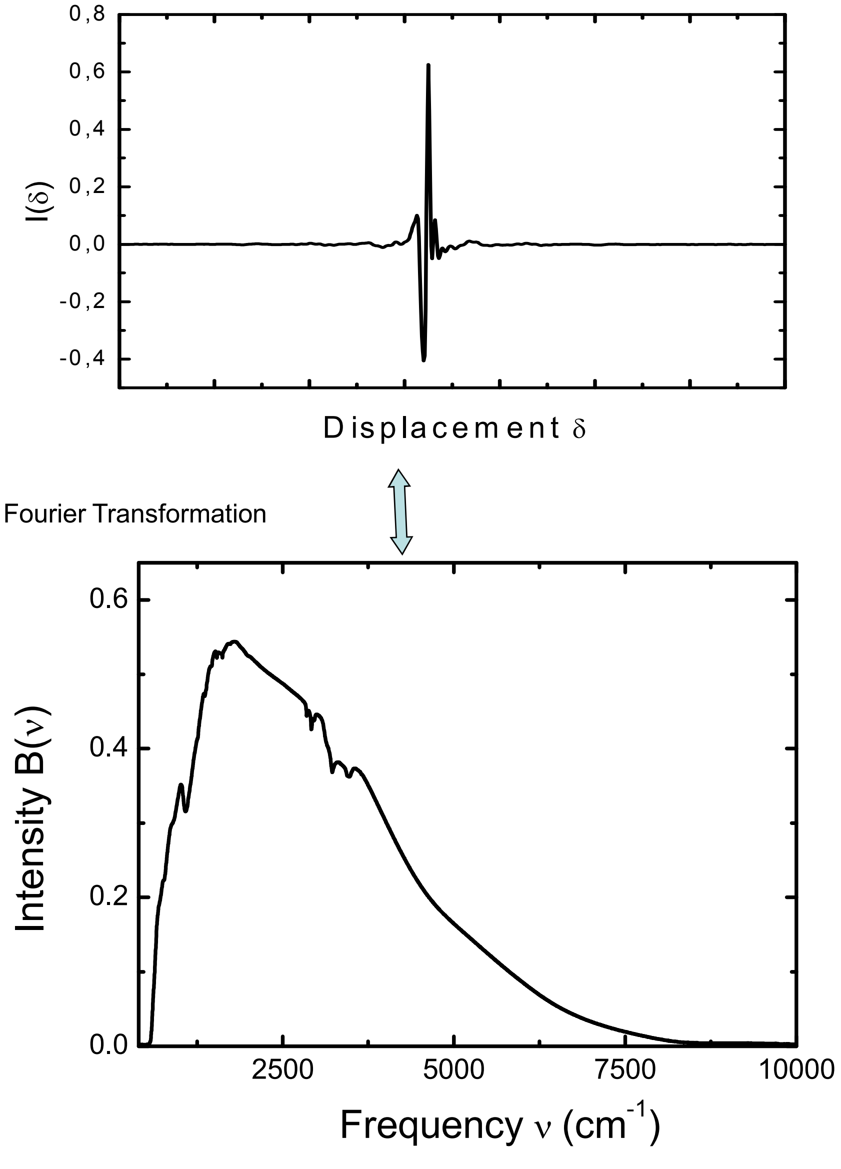

Figure 3.5: *An illustration of how an interferogram is Fourier transformed to produce a typical spectrum in the MIR frequency range for carbon nanotube [2].*

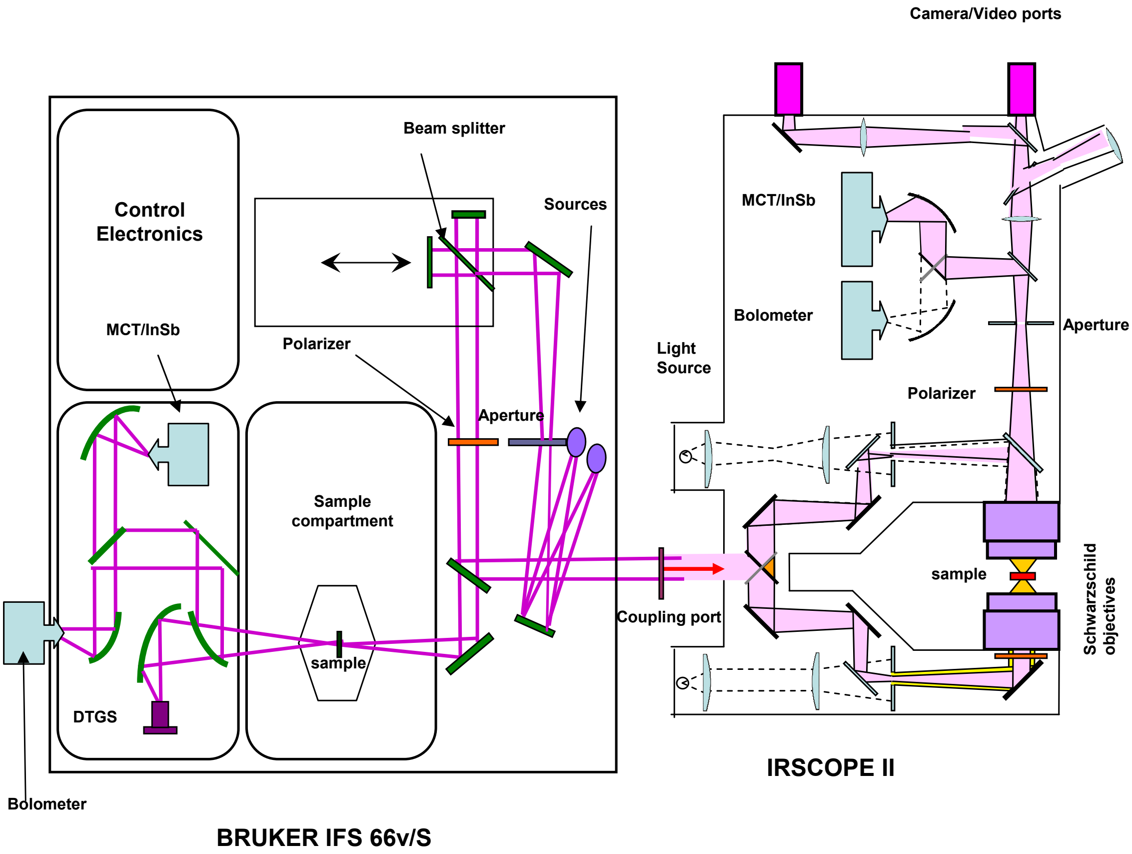

Figure 3.6: *Optical layout of Bruker IFS66v/S Fourier transform infrared spectrometer coupled to IR microscope.*

of this FTIR spectrometer. The FTIR spectrometer can cover a broad frequency range from 30 to 30000 cm^{-1}, (from far-infrared (FIR) to visible frequencies). There are three different light sources for the different ranges in the infrared frequencies. The size of the beam spot can be chosen to use apertures of size 0.25 - 12 mm with the remotely-controlled aperture wheel (see Figure 3.6). Depending on the frequency required for the measurement, different combinations of source, beamsplitter and the detector are chosen. The mercury cadmium telluride (MCT) and InSb detectors used at mid-infrared (MIR) and near-infrared (NIR) frequencies, respectively, are operated at liquid nitrogen temperature. Deuterated triglycine sulfate (DTGS) detectors are used also in FIR and MIR ranges and operated at room temperature. A silicon diode

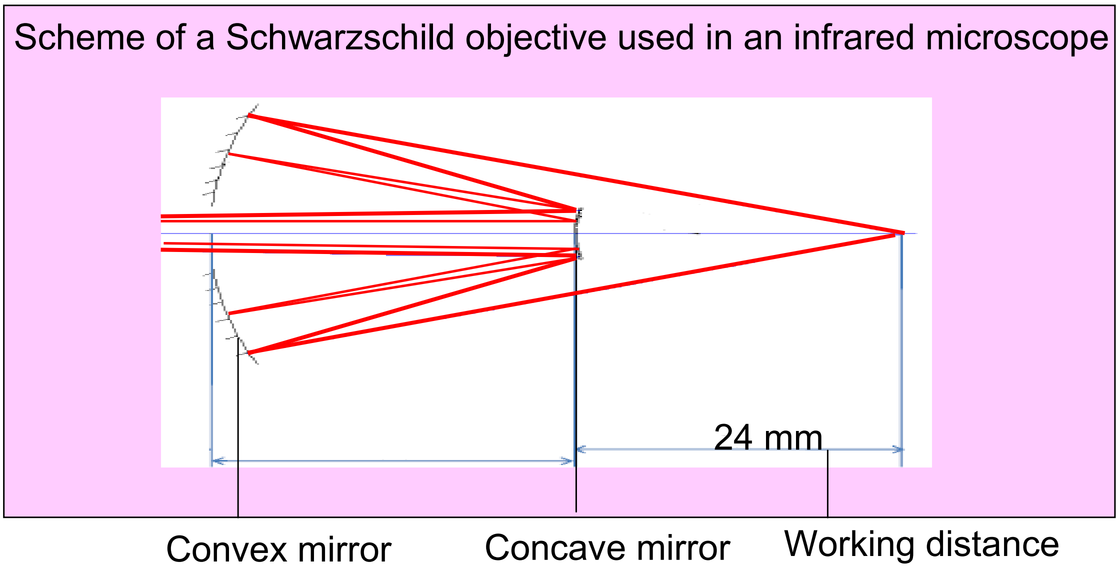

Figure 3.7: *Scheme of a Schwarzschild objective used in an infrared microscope.*

and a GaP diode detector can be used for the measurements in the visible/UV range. The silicon-based bolometer used in the FIR frequency range is a cryogenic detector operated at liquid helium temperature. The list of sources, beamsplitters, polarizers and detectors used for the different frequency ranges in the spectrometer are listed in Table 3.1.

3.2.3 Infrared microscope

In order to study very small samples by infrared spectroscopy, the radiation needs to be strongly focused. This can be accomplished with a commercial infrared microscope, which is coupled to the spectrometer. The first stage in any type of microscopic analysis is to point and locate a sample under the microscope. The sample must be in the focus in order to obtain an optimum spectrum. Obviously, this is also crucial as the sample size gets smaller. The infrared microscope provides visual examination of microscopic samples. Figure 3.6 shows the optical layout of the infrared microscope. The construction of the infrared microscope is as follows:

- **Two identical Schwarzschild objectives**: The radiation is being focused by Schwarzschild objectives. They consist of one spherical convex and one spherical concave mirror (see Figure 3.7). The objectives of our setup have a 15x magnification and a working distance of 24 mm.

- **Controlled mirrors**: it is possible to guide the incident light in the optical path of the microscope for the view mode, the reflection mode and the transmission mode.

The microscope can be operated in reflection as well as in transmission mode. The diameter of the beam is varied by apertures between 20 μm and 250 μm. In our infrared microscope, two camera ports are available; thus, during the experiment pictures of the studied sample can be taken.

3.3 Infrared spectroscopy under high pressure

Diamond is known to be the hardest natural material. In addition, it is also one of the least compressible materials. Another very important property of diamond is its transparency in the most spectrum of the electromagnetic radiation. The mentioned unique properties of diamond make it ideal candidate for generation of high pressures. And it was realized in diamond anvil cells. For more details information about diamond and diamond anvil cells (see ref. [62–64]). In general, every diamond anvil cell (DAC) contains the following parts: (i) A force applying device; (ii) Two diamond anvils; (iii) A gasket and (iv) A pressure-transmitting medium. A general schematic drawing of a DAC is shown in Figure 3.8 [2]. The sample is placed between the two culets of the diamond. Figure 3.9 shows a typical view of the top and bottom diamond of the easy lab cell before aligning the culets of the diamond. Within this project, I used two types of diamond anvils cells (DACs) (i) Syassen-Holzapfel cell [58] and (ii) a clamped cryoDAC Mega by *Easylab* company. The ruby luminescence setup were used in this work, in order to determine the pressure inside the pressure cells. In this project, I used the following pressure transmitting media: (i) finely ground CsI powder; (ii) 4:1 methanol-ethanol alcohol mixture; (iii) cryogenic liquefied argon and helium. For filling the Syassen-Holzapfel type DAC with helium, I used a commercial glass cryostat.

3.3.1 Syassen-Holzapfel-type DAC

Figure 3.10 (a) and (b) shows the Syassen-Holzapfel DAC and its cross-sectional view used in this project respectively. "The Syassen-Holzapfel type diamond anvil cell is

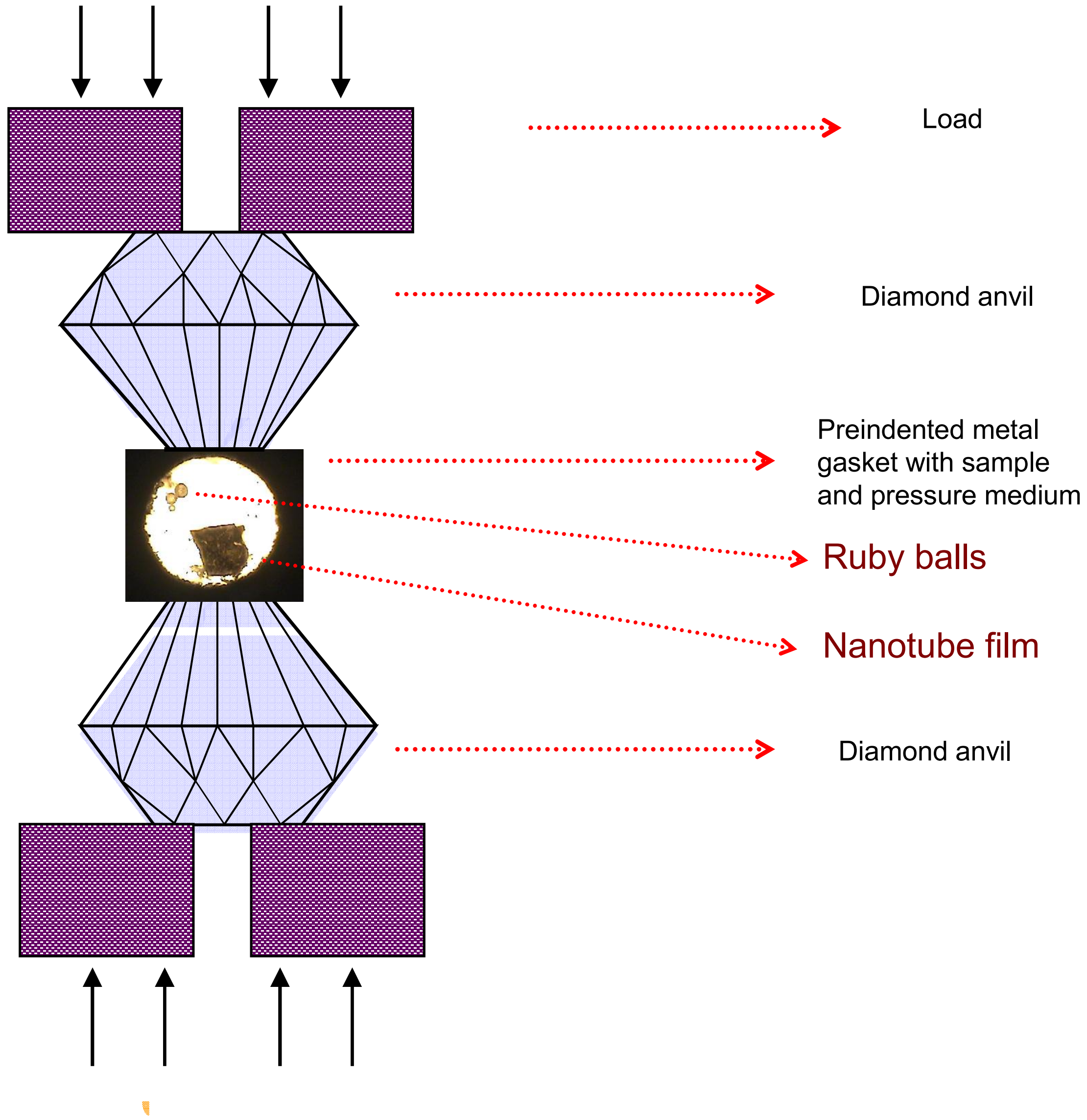

Figure 3.8: *The drawing of diamond anvil cell illustrating its basic operation [65]).*

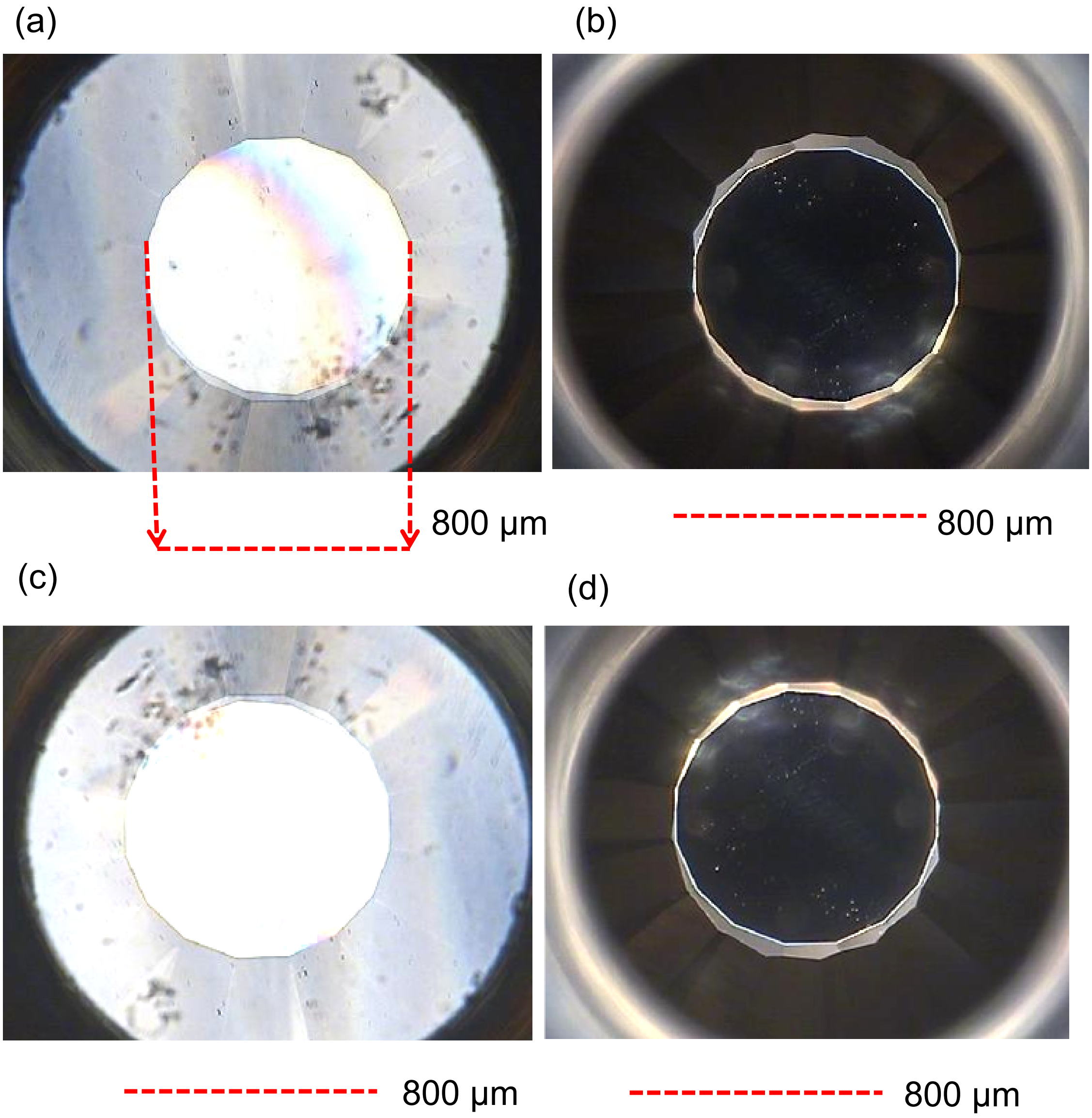

Figure 3.9: *Typical view of diamond of the easy lab cell (a),(b) before aligning the culets of the diamond in the reflection mode and transmission mode respectively (c),(d) after aligning the culets of the diamond in the reflection mode and transmission mode respectively.*

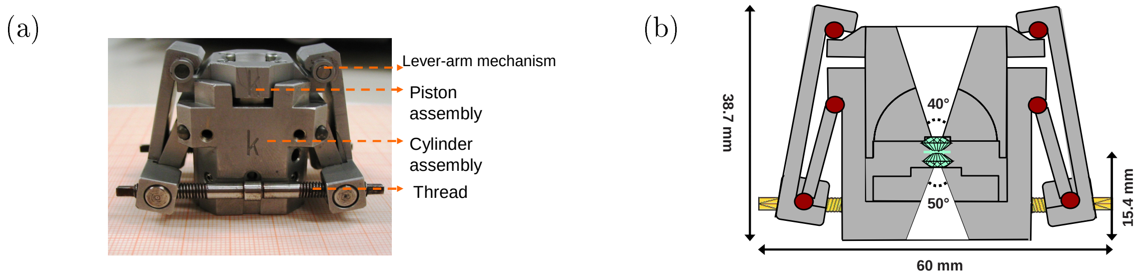

Figure 3.10: *(a) The main parts of Syassen-Holzapfel cell are shown in the picture. (b) The dimensions of the Syassen-Holzapfel pressure cell are indicated in the schematic cross-sectional view showing also the inner construction [58].*

a clamped piston-cylinder cell developed by Huber, Syassen and Holzapfel [58] [2]". The specification of the Syassen-Holzapfel DAC used within this project is as follows:

- 15.4 mm as a shortest distance to the sample.
- "The diamond anvils are made of type-IIa diamonds with height of 1.6 mm and culet diameter of 400 μm [2]".
- "The maximum pressure that can be generated in this DAC is around 25 GPa [2]".
- "The opening angle of the apertures at the piston and the cylinder assemblies are 40 ° and 50 °, respectively, to minimize signal loss [2]".

The specification of the gasket used with this pressure cell is as follows:

- "A gasket made from stainless steel [2]".
- "The initial thickness 0.25 mm [2]".
- "The gaskets pre-indented to a thickness about 50-70 μm [2]".
- "The drilled holes with diameter of about 150-300 μm [2]".

3.3.2 CryoDAC Mega Clamp cell

Figure 3.11 shows the clamp cell CryoDAC used in this project. The specification of the cryoDAC mega from *easylab* is as follows:

- "The diameter of the complete pressure cell assembly is 38 mm [2]".
- "The diamond anvils have height of 1.6 mm and culet diameter of 800 μm [2]".

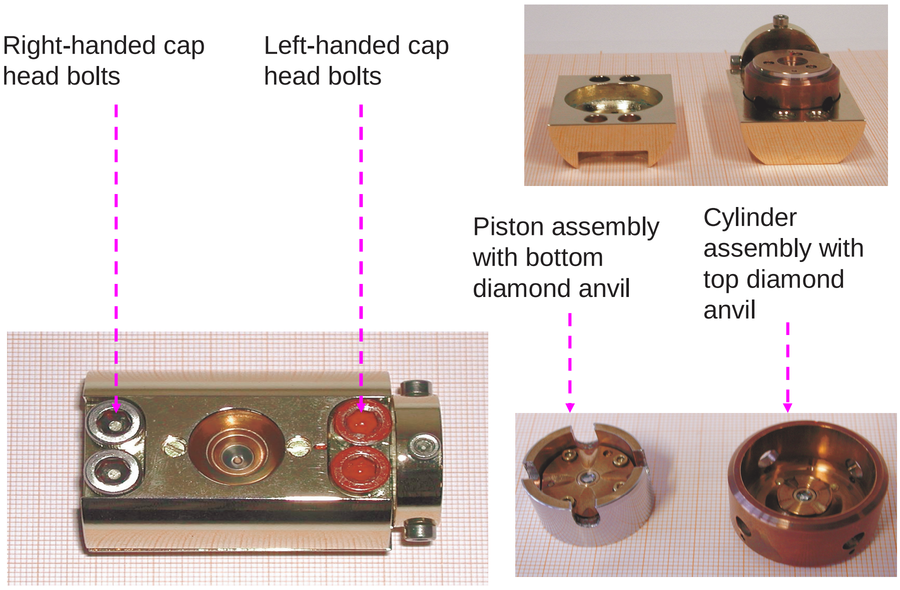

Figure 3.11: *The main parts of the clamp cell CryoDAC are shown in the picture.*

- "The opening angle of the apertures in this DAC is 50 ° at both the piston and cylinder assemblies [2]".
- "The maximum pressure that can be achieved in this DAC is about 12 GPa [2]".

The specification of the gasket used with this pressure cell is as follows:

- "The gaskets used together with this DAC are made of CuBe alloy with a thickness of 0.4 mm [2]".
- "The gaskets are preindented to a thickness of about 100 μm and drilled with holes of diameter 400 μm [2]".

3.3.3 Pressure determination method

Ruby is α-alumina (Al_2O_3). The Al^{3+} ions are replaced by Cr^{3+} ions. The Cr^{3+} is surrounded octahedrally by six O^{2-} ions. The crystallographic arrangement strongly affects the Cr^{3+} ions. When yellow-green light is absorbed by Cr^{3+}, the electrons can be excited to the metastable ^{2}E level. From this level, the electrons relax to lower energy level under emission of radiation, namely the characteristic R_1 and R_2 lines. Under hydrostatic pressure, the ruby lattice compresses almost uniformly [66–70]. This

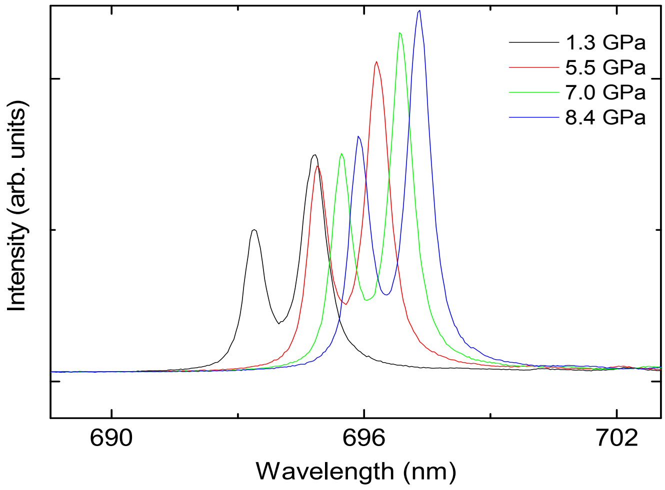

Figure 3.12: *A typical ruby spectrum R_1 and R_2 lines for various pressures at room temperature are shown.*

leads to a reduction of the Cr and O ion distance. Hence, the crystal field at the Cr^{3+} ions is increasing and the energy splitting changes. This means that the energy gap between the ^2E and the ground state decreases and the R_1 and R_2 lines shift to higher wavelength, which is called a red shift. The pressure-dependent line shift can be described by the equation [68]:

$$P(GPa) = \left(\frac{A}{B}\right)\left[\left(1+\frac{\Delta\lambda}{\lambda_0}\right)^B - 1\right] \tag{3.10}$$

"The parameters are A=1904 GPa and B=7.665. $\Delta\lambda$ is the wavelength shift of the R_1 line with pressure and λ_0 refers to the wavelength at zero pressure (694.25 nm at 298 K). A typical shift of the ruby R_1 line is shown in Figure 3.12 (b). It can be observed that the pressure-shifts are large and the frequency of R_1 can be determined easily and accurately [2]". "Thus, by measuring the frequency of the R_1 luminescence line from a ruby ball placed next to the sample in a DAC at a given temperature, the pressure generated in the sample space of the DAC can be determined [2]". Figure 3.13 shows view of the pressure cell loaded with a piece of carbon nanotube and the ruby ball.

Within this project, "the ruby ball placed in the DAC is excited by green laser of wavelength 532 nm produced by the diode-pumped solid-state laser with a power

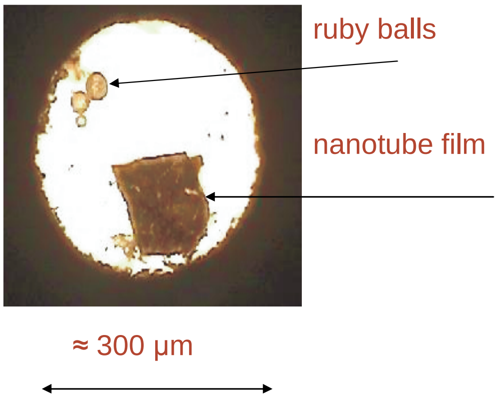

Figure 3.13: *A typical view of the pressure cell loaded with a piece of carbon nanotube film marked as sample.*

of 15 mW transmitted through a dichroic mirror. "The dichroic mirror reflects light of wavelength in the range 500-580 nm and transmits light with other wavelengths. Thus, the luminescence spectrum from the ruby is transmitted to the CCD spectrograph through the mirror and an optical fiber coupling the output from the microscope to the spectrograph [2]" (see Figure 3.14). The CCD spectrograph used in this work "is a commercial MS260i^{TM} grating-type imaging spectrograph. Figure 3.14 shows the schematic drawing of the ruby luminescence arrangement coupled to the IR microscope illustrating the luminescence measurement configuration [2]". The CCD spectrograph "consists of an asymmetrical in-plane Czerny-Turner optical configuration with unequal entrance and exit focal lengths of 220 mm and 257 mm, respectively (see Figure 3.14) [71]. The grating of this spectrograph consists of 1800 lines/mm [2]".

3.3.4 Pressure transmitting media

The larger number of high pressure experiments are intended to be achieved under hydrostatic conditions. In fact, the pressure in every part of the experimental volume is inhomogeneous in the most situations, and an amount of difference between mostly uni-axial stress and shear stresses become visible. Inhomogeneous pressure distribution may affect quality and accuracy of the experimental data. For example, apparent anomalies in pressure dependence may be detected which are not related to intrinsic properties of the studied sample. For this purpose, the hydrostatic pressure transmitting medium becomes more valuable. Therefore, it is important to characterize the various pressure medium which we used in our experimental work.

There are serval studies of the hydrostatic limits of different liquids [74,75]. Klotz *et al.* [74] "presented a systematic study of various fluids which are currently used in

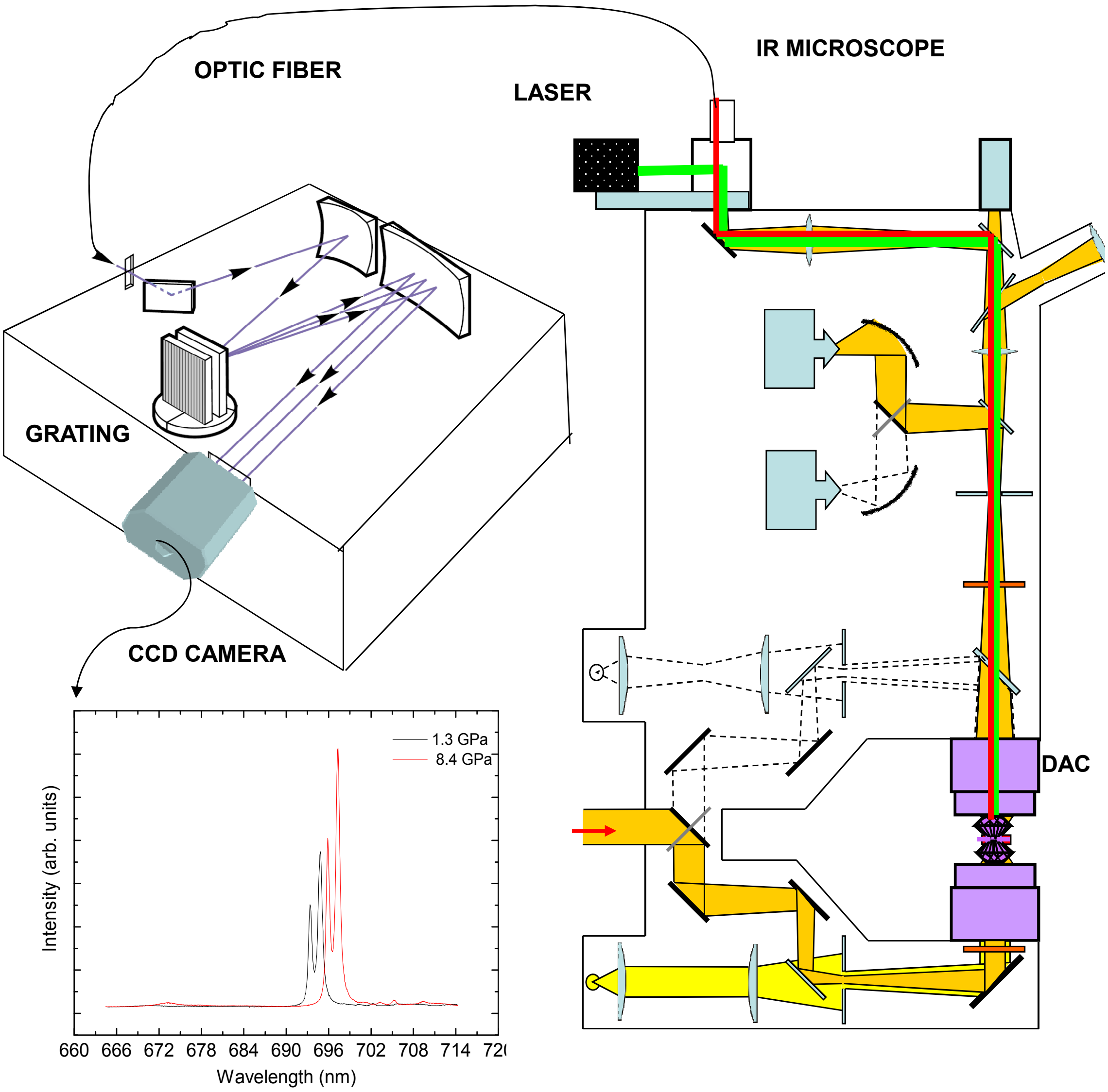

Figure 3.14: *Schematic sketch of ruby luminescence spectrometer and a typical ruby spectrum R_1 and R_2 lines for the lowest and highest pressure.*

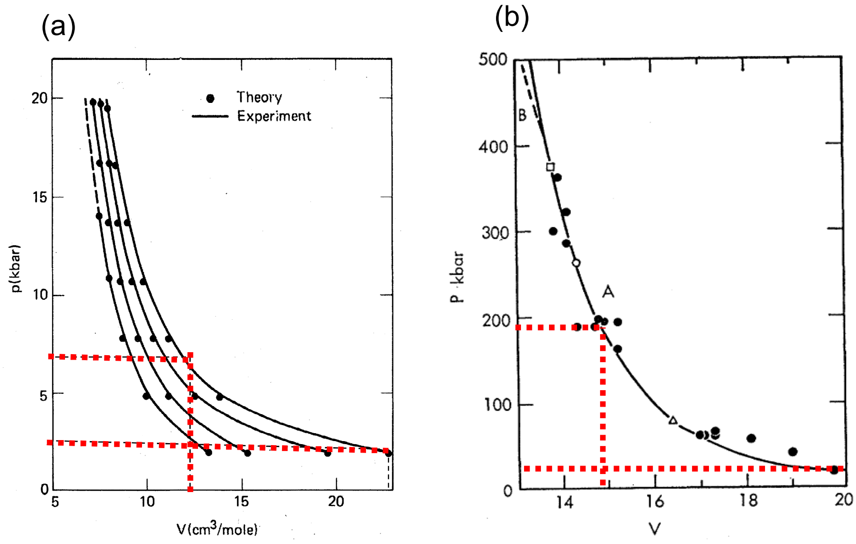

Figure 3.15: *Compressibility effects of (a) helium and (b) argon. Helium is very compressible compering to argon at low pressure [72, 73].*

high pressure experiments up to the Mbar range. The data of Klotz *et al.* were obtained by exactly the same procedure which allows a direct comparison between different pressure media. The data provide solidification transition pressures, as well as absolute values of pressure gradients across the sample chamber once the medium is solid. The data are useful for investigations in the 10 GPa range which include applications in large volume devices [74]". Klotz used "a diamond anvil cell (DAC) and the ruby fluorescence method. In most of the cases, the fluids were loaded into a membrane DAC [74] with anvil culets of 400 μm diameter and stainless steel gaskets with a 150-200 μm bore, preindented to a thickness of 40 μm. In the case of helium the culet size was 150 μm, and the gasket had a bore of 80 μm and an initial thickness of 15 μm [74]". Klotz used different hole size and initial thickness of the gasket in the case of helium because helium is very compressible at very low pressure compared to other pressure media (see Figure 3.15). In order to increase the pressure few kbar (up to 5 kbar), the volume is decreased by almost 20 % percent as shown in the Figure 3.15 (a). On the other hand, using argon as pressure transmitting medium provides least compressibility condition in the diamond anvil cell as compared helium. It is clear from Figure 3.15 (b) that the pressure is increased up to 200 kbar as the volume is decreased by about 20 % percent.

Figure 3.16 shows the DAC loaded with nanotube sample and ruby spheres immersed

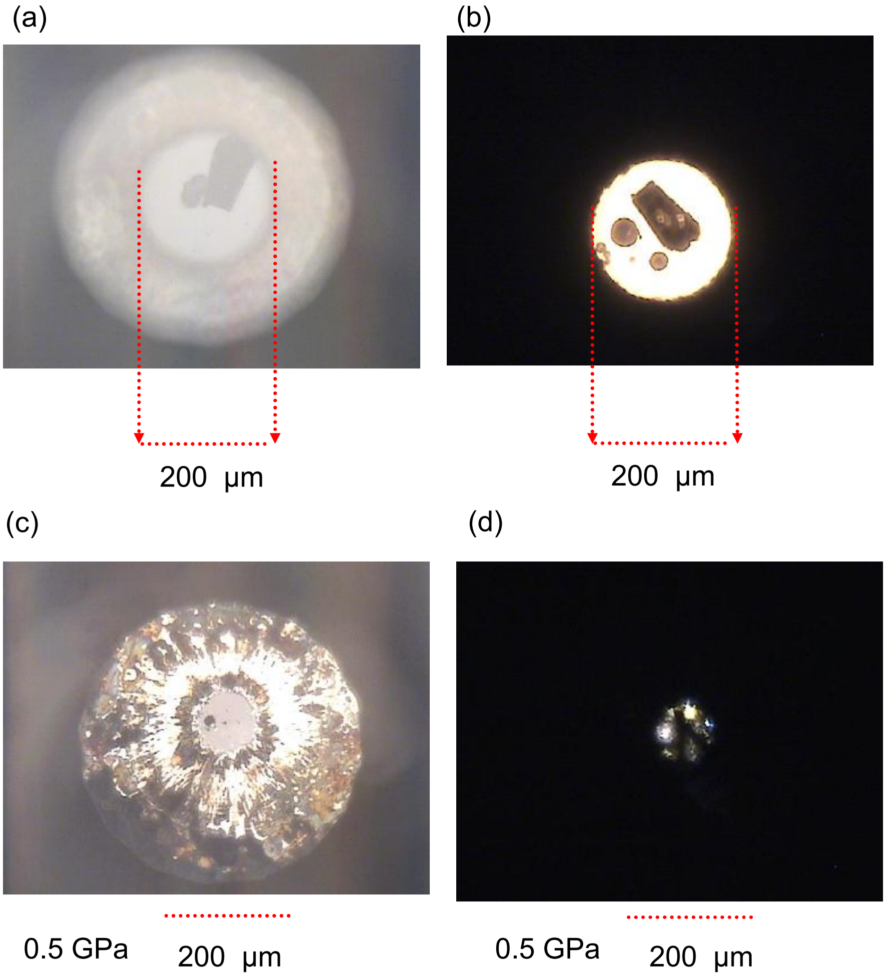

Figure 3.16: *Pictures of DAC loaded with nanotube sample and ruby spheres immersed in helium as a pressure transmitting medium:(a) DAC loaded with sample without filling with helium in reflection mode, (b) DAC loaded with sample without filling with helium in transmission mode, (c) DAC loaded with sample after filling with helium at 0.5 GPa in reflection mode, (d) DAC loaded with sample after filling with helium at 0.5 GPa in transmission mode.*

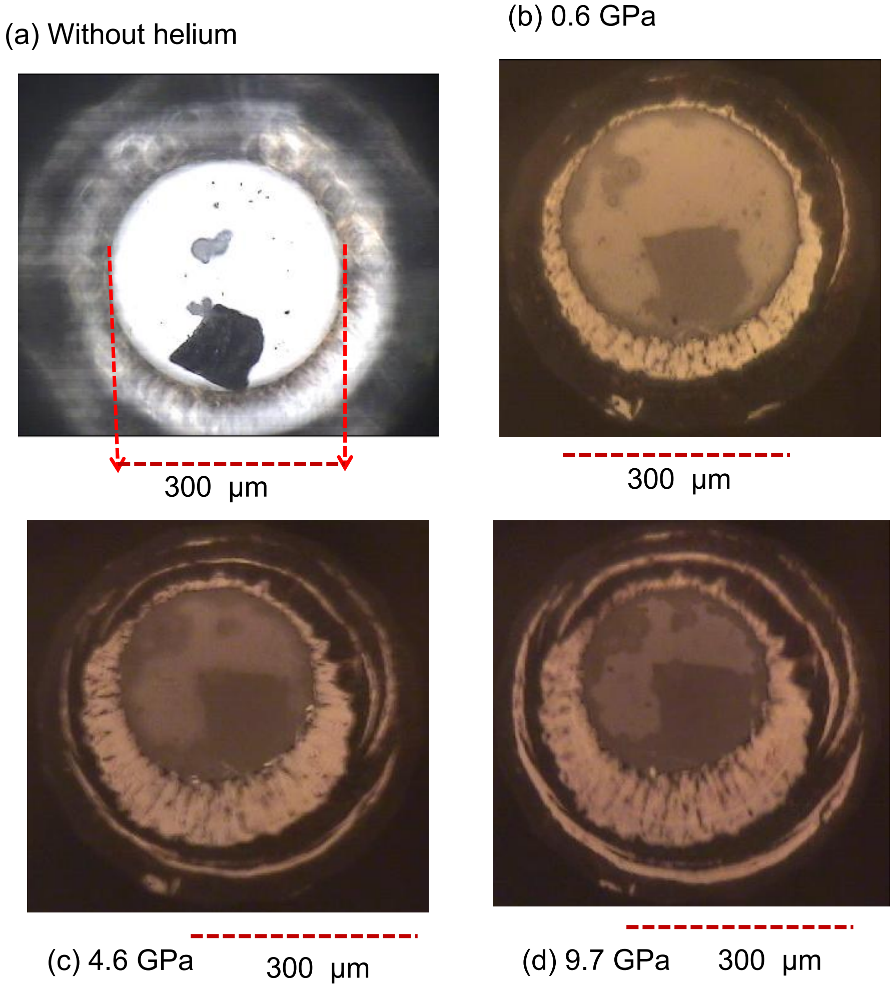
(a) Without helium

(b) 0.6 GPa

(c) 4.6 GPa

(d) 9.7 GPa

Figure 3.17: *Compressible effect of helium (a) DAC loaded with sample without filling with helium,(b) DAC loaded with sample after filling with helium at 0.6 GPa and (c) DAC loaded with sample after filling with helium at 4.6 GPa (d) DAC loaded with sample after filling with helium at 9.7 GPa .*

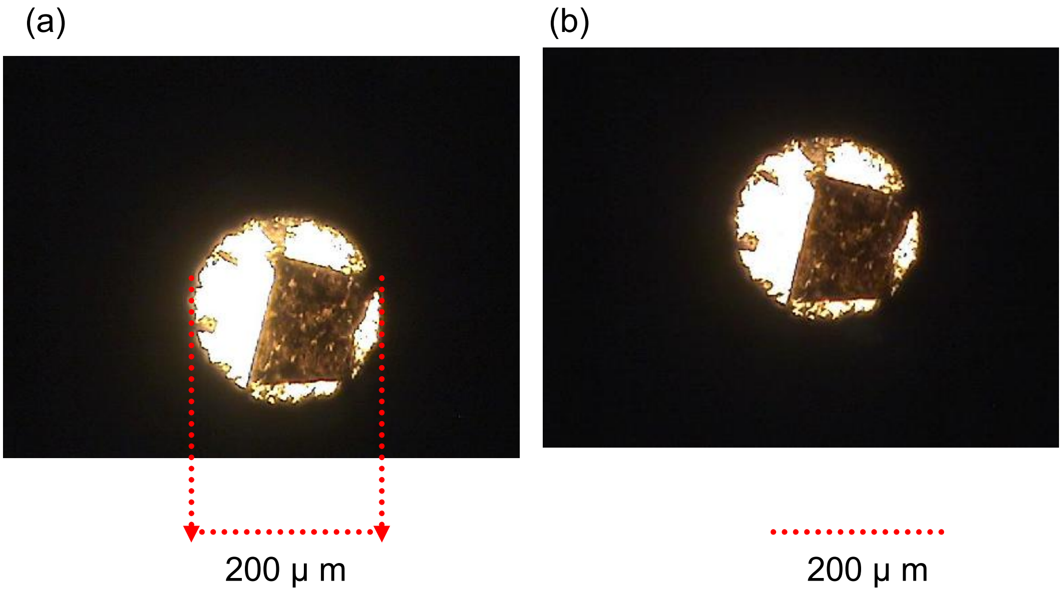

Figure 3.18: *Compressible effect of alcohol mixture the DAC loaded with sample after filling with alcohol mixture (a) at lower pressure (around 1 GPa) and (b) around 9.7 GPa.*

in helium as a pressure transmitting medium. It is clear from this figure that the pressed area is affected by a moderate pressure. Figure 3.16 (a) and (b) demonstrate a typical view of the pressure cell loaded with a piece of sample. In Figure 3.16 (a) and (b), the pictures were taken before filling the DAC with helium in reflection mode and in transmission mode. The sample hole was about $\approx 200\ \mu$m. Application of a moderate pressure caused decrease of the hole by almost 50 % (see Figure 3.16 (c) and (d)).

I made another filling with helium and the starting hole size was about $\approx 300\ \mu$m (see Figure 3.17 (a)). Figure 3.17 (b-d) shows the sample hole area after fill the DAC with helium and applying different pressure. The pressed area is shrunk by almost 10 % up to 9.7 GPa, which is appropriate to perform the IR measurements (see Figure 3.16 (b-d)). On the other hand, Figure 3.18 (a) and (b) shows the pressed area and the hole size in the transmission mode after filling the cell with alcohol mixture at lower pressure around 1 GPa. and around 9.7 GPa respectively. It is clear that the pressed area and the hole size are not affected by applying pressure up to 9.7 GPa.

The high pressure transmission measurements on carbon nanotube samples within this project have been performed using helium, alcohol mixture, argon and CsI as the pressure transmitting media. Figure 3.19 shows the hydrostaticity limits of helium, alcohol mixture and argon determined by the deviation from a linear pressure dependence of the fluorescence line. In the case of helium, the deviation is almost constat up to ≈20 GPa. On the other hand, it is noticeably increased at ≈1.7 GPa and around ≈10 GPa in the case of argon and alcohol mixture respectively. Helium is the best available pressure transmitting medium, even in its solid state, i.e. above 12.1 GPa at 300 K [74,76]. Methanol-ethanol mixtures 4:1 is the most commonly used pressure transmitting medium and has been investigated by numerous groups which conclusively show that the glass transition is at 10.5 GPa. Among the rare gases argon has the advantage that it is affordable and relatively easy to load. The disadvantage is its low solidification pressure, i.e. 1.4 GPa at 300 K. In the following subsections, the filling procedures of the pressure cells with helium and argon are explained.

Helium

A commercial glass cryogenic setup was used for filling the pressure cell with helium. Figure 3.20 shows the schematic diagram of the helium-filling setup for the Syassen-Holzapfel type DAC used in this project. Briefly, the helium filling can be done as follows: The first vacuum layer is sealed under 4×10^{-3} bar. The second layer is filled with liquid nitrogen. The third layer is sealed also under 4×10^{-3} bar. The vessel is purged with helium gas several times, and then filled with liquid helium. During this process, the helium flows into the DAC. The DAC is then sealed with the aid of a remote access mechanism provided in the cell holder.

Argon

A cryogenic-filling setup for argon was used [2]. "Figure 3.21 shows the schematic diagram of the argon-filling setup for the Syassen-Holzapfel type DAC used in this project. A similar arrangement is used for the CryoDAC Mega cell with adaptations to accommodate the differences in the way the load is applied (see Section 3.3 for detailed information on the construction of the DACs used in this project) [2]". "The argon filling can be done as follows: The vessel is purged with argon several times and continuous argon flow is maintained with slight over-pressure. The vessel is then placed in the liquid nitrogen bath. The flow of argon is then regulated such that there is a constant under-pressure of about 0.8 bar maintained in the vessel. "During this process, the argon liquefies and flows into the DAC. The DAC is then sealed with the aid of a remote access mechanism provided in the cell holder [2]".

Pressure medium	Solidification pressure [73-75]
Helium	12 Gpa
Argon	1.4 GPa
Alcohol mixture	10 GPa

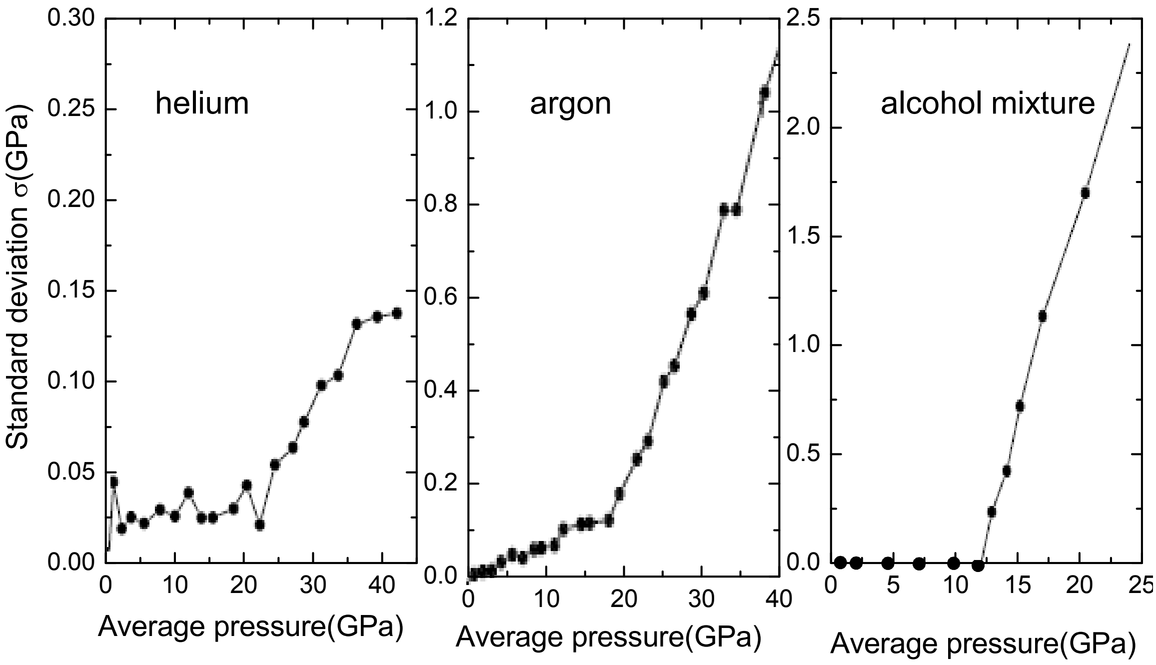

Figure 3.19: *Pressure dependence of the standard deviation σ for helium, argon and 4:1 methanolethanol [74].*

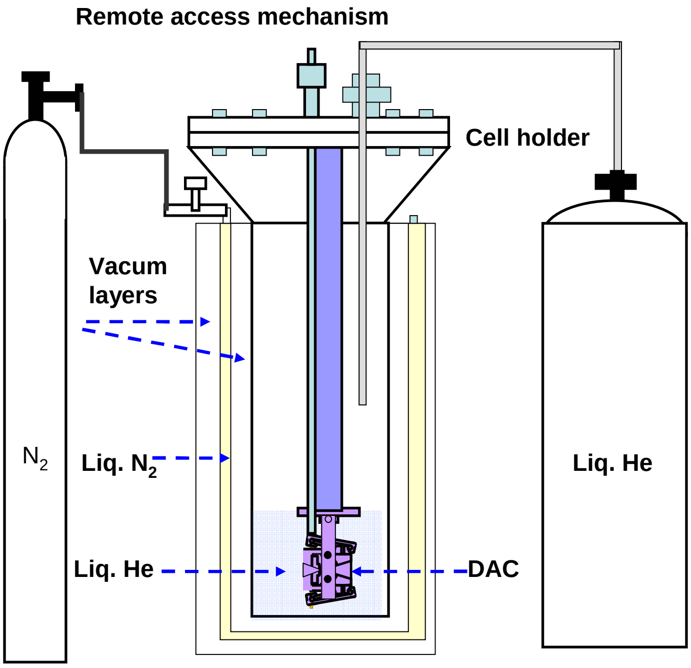

Figure 3.20: *General schematic drawing of the experimental arrangement for cryogenic loading of helium in the Syassen-holzapfel type DAC.*

3.3.5 Optical properties of diamond

"In order to perform IR measurements, DACs employ type-IIa diamonds which do not contain nitrogen impurities and are insulating. The refractive index (n_{dia}) is 2.38 at 800 cm^{-1}. The dispersion of the refractive index of diamond is very small in the IR range (see Figure 3.22). The changes in the refractive index of diamond with increasing pressure is about -0.00052 /GPa [77, 78] [2]".

IR transmission at high pressures

Figure 3.23 illustrates the general configuration for transmission measurements. In order to measure the reference spectrum for each measured pressure, the sample is placed one half of the gasket hole area and then filling with the pressure medium and ruby ball. The transmittance of the sample in the DAC can be calculated as

$$T = \frac{I_{sample}}{I_{reference}} \tag{3.11}$$

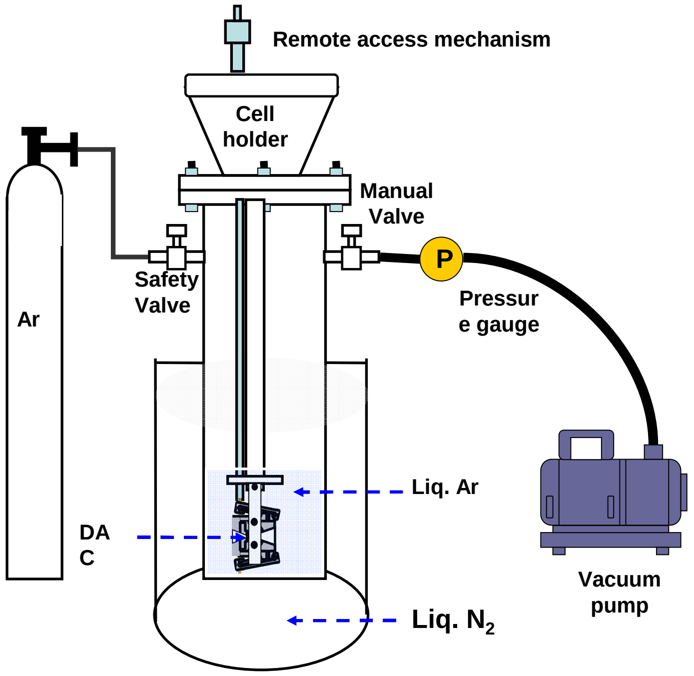

Figure 3.21: *Schematic sketch of the experimental arrangement for cryogenic loading of argon in the Syassen-holzapfel type DAC [2].*

the absorbance can be calculated as from transmittance

$$A = -log_{10}T \tag{3.12}$$

"where I_{sample} is the intensity of light transmitted through the sample in the DAC while $I_{reference}$ is the intensity of light transmitted through the pressure medium within the DAC [2]". One of the important aspect to be considered is the sample tilting, while we are filling the pressure cell with the sample. The sample must be completely flat in order to avoid the sample movement during the measurements in the transmission mode. Figure 3.25 shows the pressure cell loaded with tilted sample.

It is important to consider the interference fringes. The wiggles in the pressure-dependent absorbance spectra are Fabry-Perot interference fringes due to multiple reflections within the sample or between the surface of the diamond anvil and the sample surface. These interference fringes appear specially in case of using helium an alcohol mixture as a pressure transmitting media. Since helium and alcohol mixture remain liquid up to 10 GPa the studied SWCNT film is not pressed towards the diamond anvil surface, but remains free standing. Therefore, a small gap between

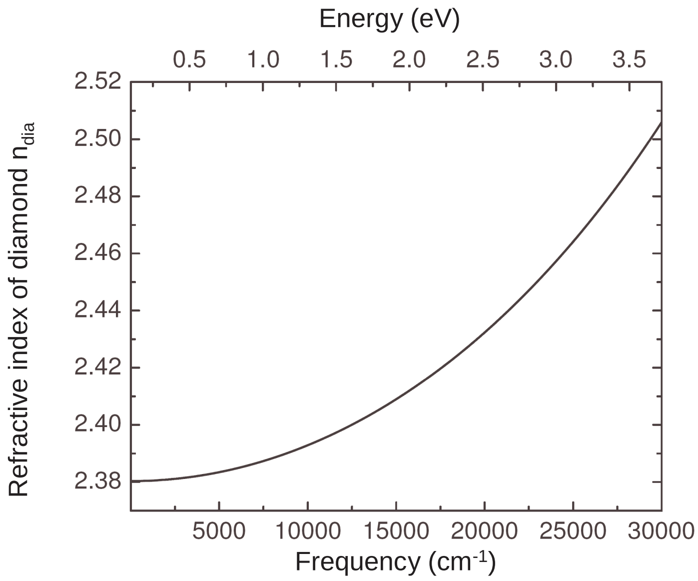

Figure 3.22: *The refractive index of diamond in the infrared frequency range* [77].

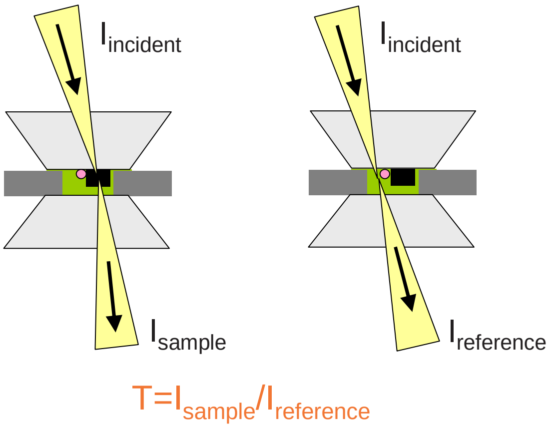

Figure 3.23: *An illustration of a transmission measurement configuration in a diamond anvil cell [2].*

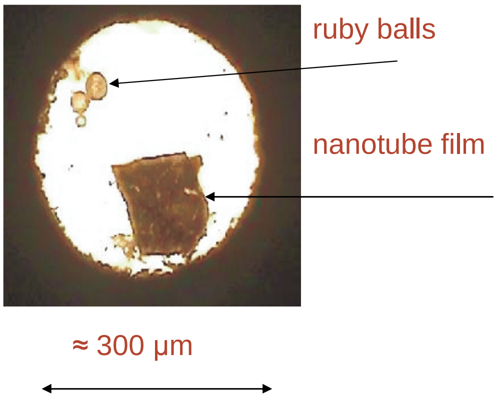

Figure 3.24: *A typical view of the pressure cell loaded with a piece of flat carbon nanotube film marked as sample.*

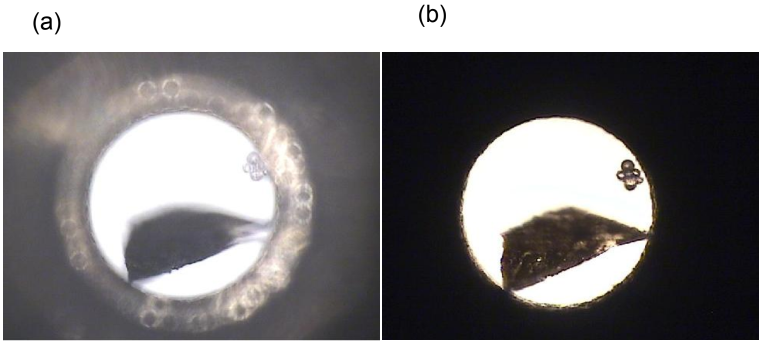

Figure 3.25: *The pressure cell loaded with tilted sample.*

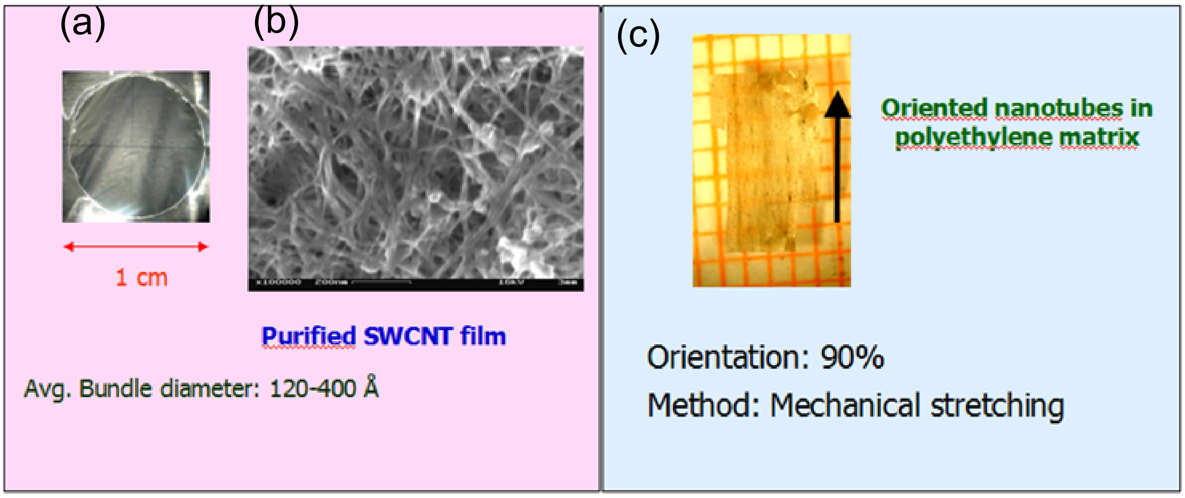

Figure 3.26: *(a) "Optical image of an unoriented carbon nanotube film [2]". (b) "SEM picture of a purified unoriented carbon nanotube film [2]".*(c) "Optical image of oriented nanotubes embedded in poylethylene matrix. The black arrow in the figure indicates the orientation of the nanotube axis in the matrix [2]".

SWCNT film and the diamond anvil produced weak Fabry-Perot interference pattern. However, this interference does not affect precision of the fitting procedure. The wiggles period is small compared to the typical width of the analyzed spectral features.

3.4 Investigated Nanotubes Samples

I studied within this project several nanotube samples: oriented, unoriented nanotubes, C_{60} peapods and DWCNTs. "The unoriented SWCNT films were obtained from Dr. F. Hennrich from the Institute of Nanotechnology at Forschungszentrum Karlsruhe, Germany [81, 82] [2]". The average thickness of the unoriented single wall carbon nanotube film synthesized by Hennrich *et.al* [81,82] was about 200 nm. Figure 3.26 (a) shows the optical image of the unoriented nanotube film [2]. "Figure 3.26 (b) shows the scanning electron microscopic (SEM) image of the purified unoriented film [2]". From the SEM image, the bundle diameters of the unoriented single wall carbon nanotube is about 12-40 nm [2].

"The film of oriented nanotubes in the polyethylene matrix was received from Prof. Y. Iwasa at the Institute for materials research, Tohoku university, Japan [83] [2]".

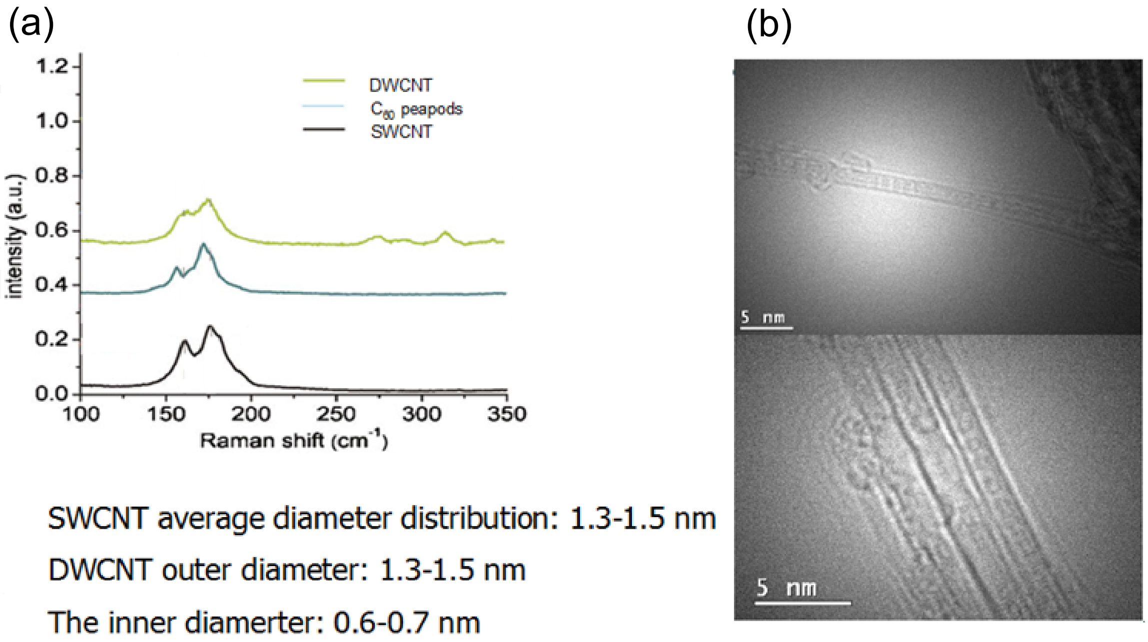

Figure 3.27: *(a) Raman spectrum of SWCNT, peapods and DWCNT (b) TEM image of a peapods with adsorbed* C_{60} *molecules [79, 80]. (c) TEM image of a washed* C_{60} *peapods [79, 80].*

Sample Type	Synthesis	d (nm)	Orientation	Avg. Thickness
Purified unoriented CNTs	Laser ablation	1.3 nm	-	200 nm
Oriented SWCNTs embedded in polyethylene matrix	Laser ablation	1.4 nm	90% within 25°	25 μm
Purified unoriented SWCNTs	Arc discarge	1.4 nm	-	150 nm
Peapods	Arc discarge	1.4 nm	-	150 nm
Purifed unoriented DWCNT	Arc discarge	Outer. d. 1.4 nm Inner. d. 0.7 nm	-	150 nm

Table 3.2: *List of the samples investigated within this project and brief information on the morphological properties and synthesis technique.*

Figure 3.26 (c) shows the optical microscopy image of the oriented nanotube film embedded in polyethylene matrix. The film thickness is about 10-30 μm. "The orientation of the nanotube axis is indicated by the arrow [2]". The studied samples of unoriented and oriented nanotubes have been prepared by the pulsed laser evaporation method. The average diameter is between 1.2 nm to 1.4 nm.

The C_{60} peapods and DWCNTs were obtained from Dr. Katalin Kamarás; Research Institute for Solid State Physics and Optics, Hungarian Academy of Sciences [79, 80]. Samples C_{60} peapod-based DWNCTs were prepared from arc discharge single-walled nanotubes (SWNCTs). The C_{60} peapods (C_{60} encapsulated SWCNTs) and DWCNTs studied within this project were prepared by Kamars *et al.* [79,80] using the supplementation method. The starting material of single walled carbon nanotube and C_{60} fluorine were prepared by using the arc-discharge technique and were obtained from NANOS Research (former SES Research). The average diameter of starting material of single walled carbon nanotube is 1.3 nm. Figure 3.27 (b) shows the high resolution transmission electron microscopic (TEM) images of the C_{60} peapods films [79, 80]. See Ref. [79–83] for more detailed information about the studied sample. A general overview of the studied nanotube samples is shown in Table 3.2. In general, single and double wall carbon nanotubes bundles can be synthesized by laser evaporation, arc discharge and chemical vapor deposition. See Ref. [6, 84, 85] for more detailed information. In the following I present a brief description of both techniques which were used for synthesis single wall carbon nanotubes. **Laser ablation** The laser evaporation apparatus consists of the following parts [6, 84]:

Synthesized method	Bundle diameter	Tube diameter	Catalyst
Laser ablation [84]	10-20 nm	1.2-1.3 nm	Ni-Co 1:1
Arc discharge [85]	10-20 nm	1.3-1.4 nm	Ni-Co Co-Y Ni-Y 1:1

Table 3.3: *Comparison between single wall carbon nanotubes synthesized by laser ablation and arc discharge.*

1. Laser source.
2. Furnace.
3. Graphite target contains Co-Ni as a catalyst.
4. Water cooling system.
5. Quartz tube.

Synthesis of carbon nanotube soot using laser ablation technique is as follows. First, "the graphite target is placed in the middle of [2]" the quartz tube. Then temperature of the furnace is increased to ≈ 1200 °C. The graphite target is vaporized by using laser beam. **Arc-discharge** Arc-discharge is one of the most efficient techniques to synthesize carbon nanotube with variety of diameter. The main parts of arc discharge apparatus are as follows [6, 85]:

- Power supply to produce high current.
- Two electrodes (anode and cathode).
- Stainless steel or quartz tube in which the anode and cathode are fixed.
- Water cooling system.
- The catalyst.

The diameter and the quality of carbon nanotube synthesized by arc-discharge depend on the catalyst used during the synthesis process. There are several mixtures of the catalyst such as Ni-Co, Co-Y or Ni-Y in various atomic percentages. Table 3.3 shows the comparison between single wall carbon nanotubes which were synthesized by laser ablation and arc discharge [84, 85]. Scanning electron microscope (SEM) images show that bundle diameter is almost the same in both cases. Transmission electron microscope (TEM) images show that the tube diameter is slightly larger in case of using arc discharge technique [84, 85].

4 Results and Discussion

In this chapter, the pressure-dependent infrared studies on the SWCNTs, C_{60} peapods and DWCNTs films are presented and discussed.

4.1 Unoriented SWCNT films

The pressure-dependent transmission measurements were performed in the near-IR and visible frequency ranges 2000-22000 cm^{-1} at pressures up to 8 GPa using helium, alcohol mixture, argon or CsI as pressure transmitting media. In order to study very small samples by infrared spectroscopy, the radiation needs to be strongly focused. This can be accomplished with a commercial infrared microscope, which is coupled to the spectrometer. Figure 4.1 shows the absorbance spectra of the unoriented SWCNTs film in the near-infrared and visible frequency range at the lowest pressure (0.3 GPa helium, 0.4 GPa alcohol mixture, 0.7 GPa argon, 0.4 CsI). Because helium is very compressible below 1 GPa, the starting pressure of helium is lower compared to alcohol mixture, argon and CsI. Helium is very compressible at very low pressure compared to the other pressure media. In order to increase the pressure a few kbar (about 5 kbar), the volume is decreased by almost 20 % percent [72]. On the other hand, argon and alcohol mixture have less compressibility compared to helium. For example, the pressure is increased by $\approx$ 200 kbar, when the volume is decreased by $\approx$ 20 % percent in case of argon as a pressure transmitting medium [73] (see Section 3.3.4).

The linear background contribution to the absorbance spectra produced by the low energy tail of the π plasmon absorption centered around 5 eV was subtracted from the measured spectra in order to obtain the pure absorption due to the optical transitions (see Figure 4.1) [86,87]. The first two bands, approximately around 0.68 eV and 1.2 eV, are assigned to transition between the first and second pair of van Hove singularities in semiconducting tubes (S_{11}, S_{22}), respectively whereas the band around 1.8 eV is assigned to the first pair of singularities in metallic tubes M_{11}. The energies of the optical transition are slightly different because the starting pressure is not the same for all pressure transmitting medium (see Table 4.1) and they are strongly affected by applying pressure as we will see later.

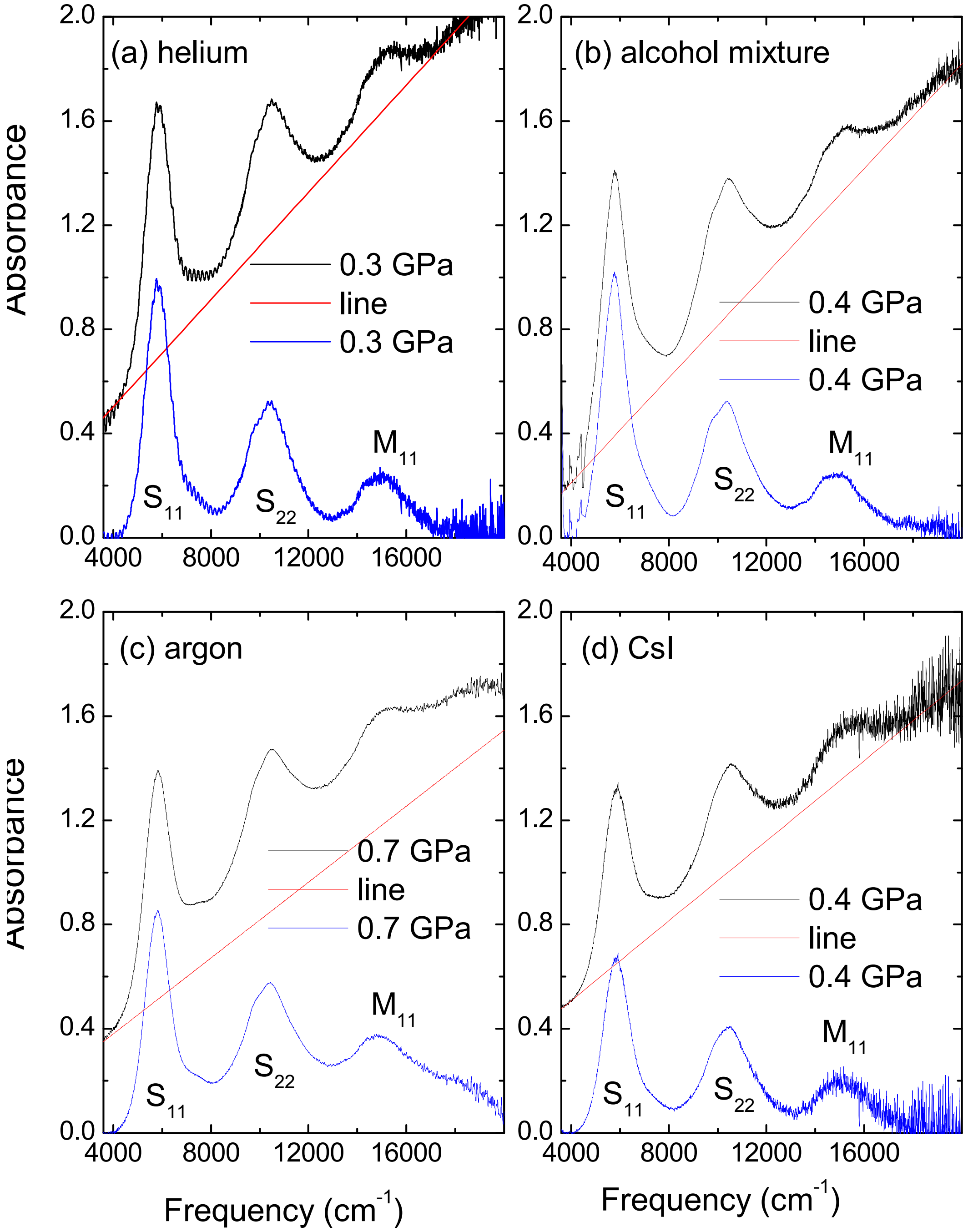

Figure 4.1: *Absorption spectra of purified unoriented carbon nanotube films at lowest measured pressure together with the linear background subtracted spectra for using (a) helium (0.3 GPa), (b) alcohol mixture (0.4 GPa), (c) argon (0.7 GPa) [2] and (d) CsI (0.4 GPa) as a pressure transmitting medium. The labels* S_{ii} *and* M_{ii} *denote the optical transitions between pairs of van Hove singularities in semiconducting and metallic SWCNTs, respectively, where the indices ii indicate the energy sequence of the involved van Hove singularities [51].*

Optical transition	helium	alcohol mixture	argon	CsI
$S_{11}(1)$	5822 cm^{-1}	5781 cm^{-1}	5809 cm^{-1}	5838 cm^{-1}
$S_{22}(1)$	9827 cm^{-1}	9771 cm^{-1}	9658 cm^{-1}	9911 cm^{-1}
$S_{22}(2)$	10570 cm^{-1}	10374 cm^{-1}	10377 cm^{-1}	10718 cm^{-1}
$M_{11}(2)$	14384 cm^{-1}	14302 cm^{-1}	——	——
$M_{11}(2)$	15279 cm^{-1}	15098 cm^{-1}	14994 cm^{-1}	15024 cm^{-1}

Table 4.1: *The energies of the optical transitions of the unoriented SWCNTs at lowest pressure for using helium, alcohol mixture, argon and CsI as a pressure transmitting media.*

In case of using helium as a pressure transmitting medium, the small wiggles are seen clearly in the absorbance spectra (Figure 4.1 (a)). These wiggles are Fabry Perot interference fringes due to multiple reflections between the surface of the diamond anvil and the sample surface. These interference fringes appear specially in case of using helium as pressure transmitting medium. Since helium and alcohol mixture remains liquid up to 10 GPa the studied SWCNT film is not pressed towards the diamond anvil surface, but remains free standing. Therefore a small gap between SWCNT film and the diamond anvil produces weak Fabry-Perot interference pattern. However, this interference does not affect precision of the fitting procedure. The wiggles period is small compared to the typical width of the analyzed spectral features. On the other hand, the other pressure transmitting media turn solid at very low pressure, and CsI is already solid at ambient condition.

The main results are presented in Figure 4.2 (i) and (ii), which depicts the transmission and the absorption spectra of purified SWCNT films in the near infrared and visible frequency range as a function of pressure. Obviously, the optical spectra of the SWCNTs are strongly affected by pressure in the measured frequency range for using different pressure media as follows: (i) The intensity of the optical transition decreases with increasing pressure. (ii) The optical absorption bands located above 4000 cm^{-1} shift to lower frequencies and broaden.

According to theoretical investigations the red-shift of the optical absorption bands under pressure can be attributed to the pressure-induced deformation of the nanotubes causing σ^*-π^* hybridization effects and changing the symmetry of carbon nanotubes [88, 89]. The red-shift of the optical transitions is in a good agreement with the previous pressure-dependent studies on SWCNTs [90]. Kazaoui *et al.* used solid pressure transmitting medium (KBr), which is known to be less hydrostatic compared to helium and alcohol mixture [46]. The reported shift of the energy of S_{11} transition

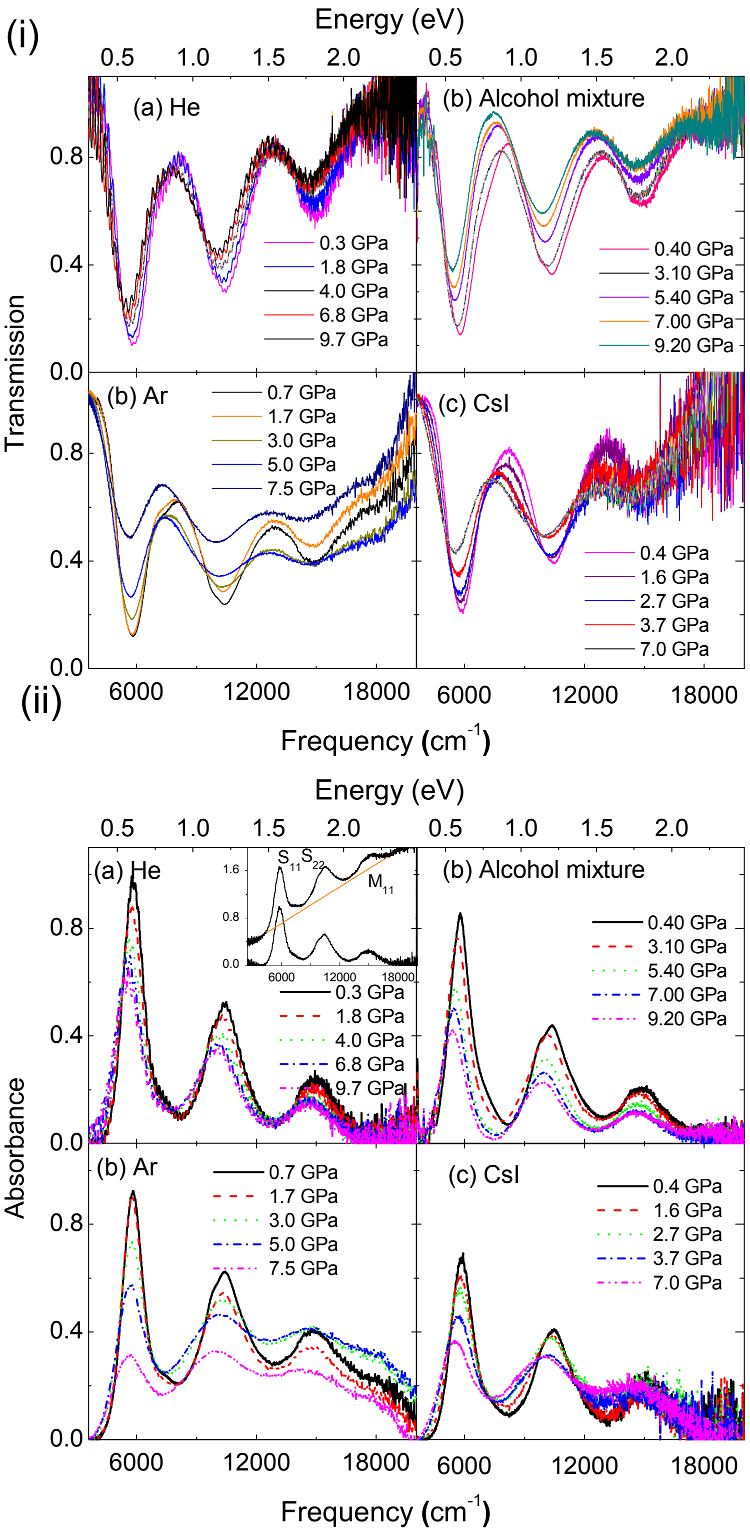

Figure 4.2: *(i) Transmittance spectra of purified unoriented carbon nanotube films at different pressure using (a) helium, (b) alcohol mixture, (c) argon [2] and (d) CsI as a pressure transmitting media [51]. (ii) IR-spectra in absorbance mode of purified unoriented SWCNTs films at different pressure using (a) helium, (b) alcohol mixture, (c) argon [2] and (d) CsI as a pressure transmitting media [51]*

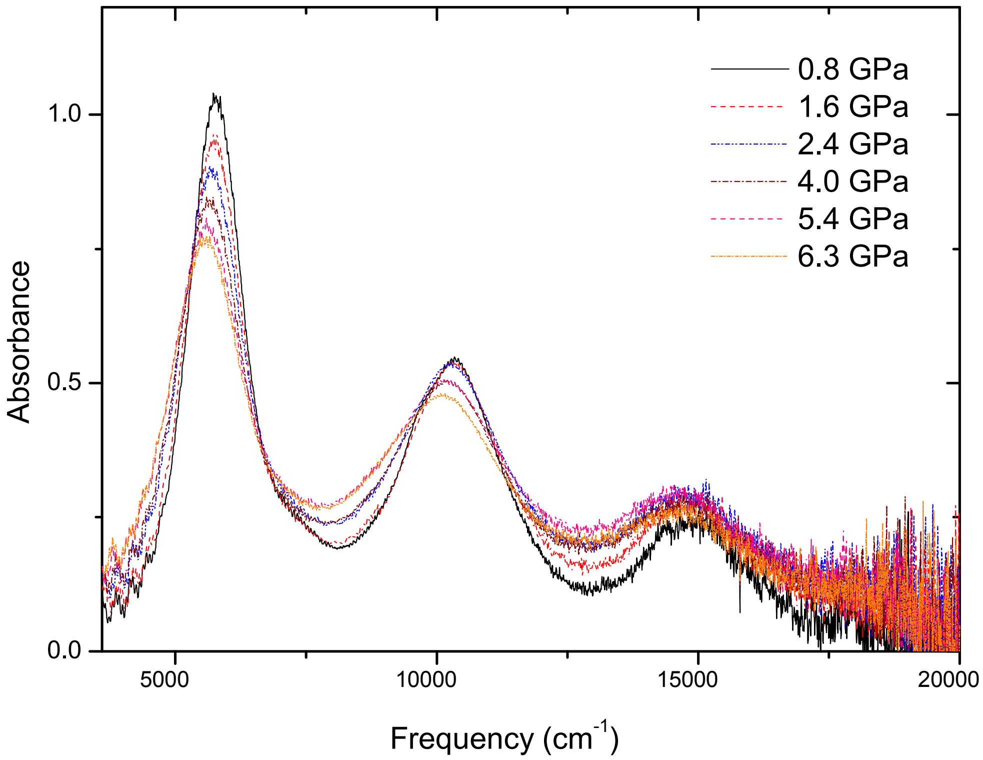

Figure 4.3: *IR-spectra in absorbance mode of purified unoriented SWCNTs films with releasing pressure using helium as a pressure transmitting medium [51]*

at 4 GPa is nearly two times more than that observed in our measurements using different pressure transmitting media including a solid pressure transmitting medium CsI [46]. The shift of the optical transition with releasing pressure was completely reversible (see Figure 4.3).

The energies of the optical transitions were obtained according to the following procedure (see Figure 4.1): The linear background contribution was subtracted from the measured spectra. The background-subtracted spectra were then fitted with Lorentz functions (see Figure 4.4). Generally, SWCNTs occur in bundles with 10-100 nanotubes per bundle. These bundles usually consist of nanotubes with different chirality and slightly different diameters. Clearly from the fitting of the absorbance and transmittance spectra as shown in Figure 4.4 (i) and (ii), there is a spread in the excitation

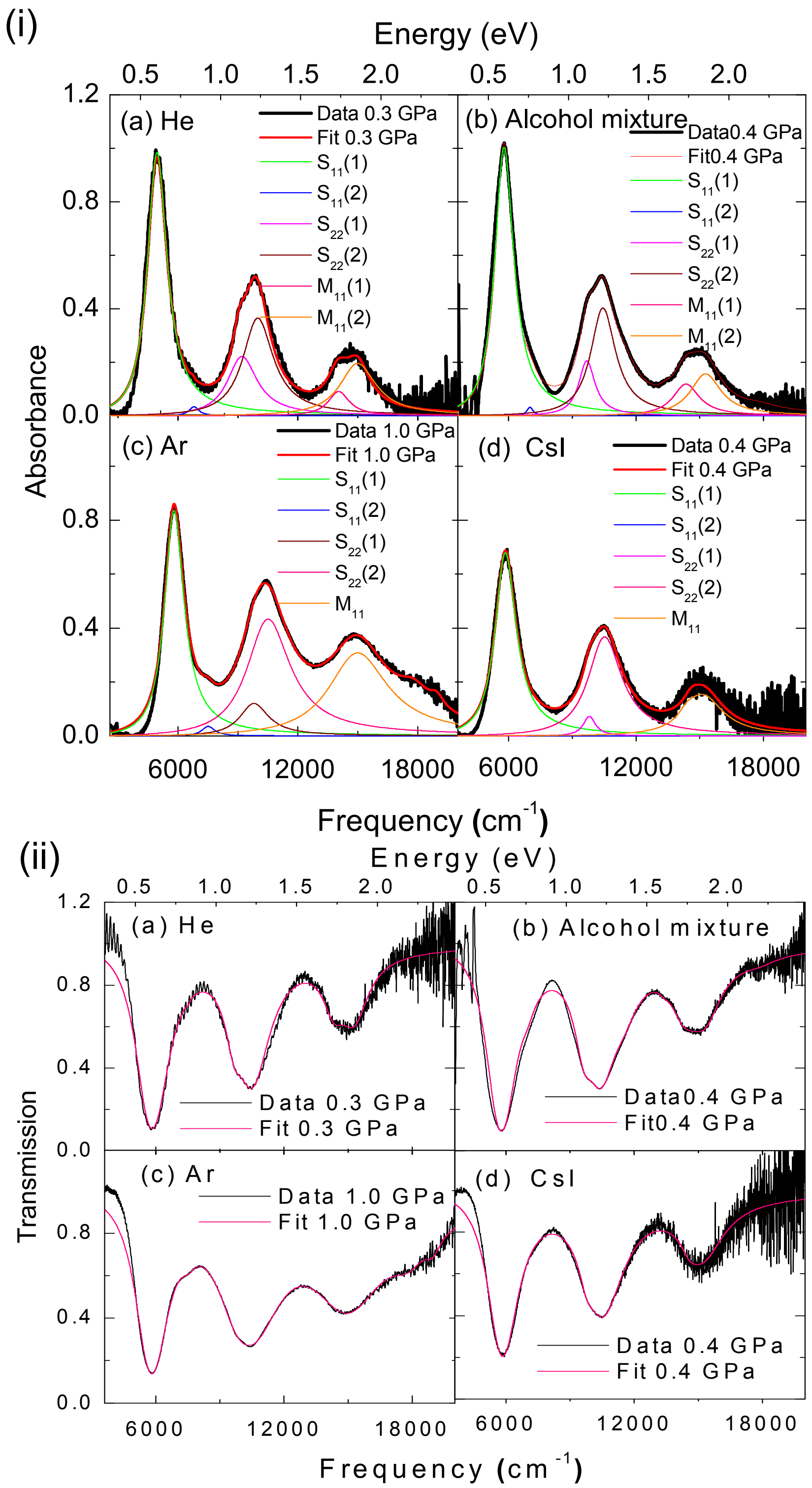

Figure 4.4: *(i) Fit of the measured absorption spectrum of SWCNT at low pressure and the fit with Lorentz functions for using (a) helium, (b) alcohol mixture, (c) argon [2] and (d) CsI as a pressure transmitting medium [51]. (ii) The fitting of the IR-spectra in transmission mode for using (a) helium, (b) alcohol mixture, (c) argon [2] and (d) CsI as a pressure transmitting medium [51].*

energies of the different optical transitions [27] which is in good agreement with both theoretical and experimental investigations.

Kataura showed that the energy differences between the vHs peaks E_{ii} depends on the tube diameter [27]. He also showed that there is a spread in energy for a fixed diameter (see Section 2.4 for more details). It is obvious from Figure 4.4 (i) that the spread in energy is smaller for the first optical transition S_{11} which is consistent with recent experimental and theoretical results [27]. Therefore we used only one contribution in order to fit the S_{11} transitions. On the other hand, we used two contributions in order to fit the S_{22} transitions for all pressure media. In case of using helium and alcohol mixture as a pressure transmitting media, we used two Lorentzian contributions for fitting the M_{11} band as well as for the S_{22} band. In contrast, for argon and CsI we used only one Lorentzian contributions in order to fit the M_{11}. The broadening of the M_{11} band is smaller due to better hydrostaticity in case of helium and alcohol mixture as a pressure transmitting media, therefor we used two Lorentzian contributions for fitting the M_{11} transition.

4.1.1 Low pressure regime

Figure 4.5 shows the obtained energies of the optical transition of the SWCNTs film as a function of pressure. Without considering the pressure transmitting medium, with increasing pressure, the optical transitions shift to lower energy up to the pressure P_c=2-3 GPa i.e. the optical transitions show only a small red-shift up to certain critical pressure P_c. By applying pressures above P_c, the energies of the optical transitions decrease suddenly. The anomaly in the pressure-induced shifts of the optical transitions at around P_c=2-3 GPa is more pronounced for the S_{22} and M_{11} optical transitions.

It is clear from Figure 4.5 that the critical pressure P_c shows different values for different pressure transmitting media. Table 4.2 shows the values of the critical pressure P_c for using different pressure transmitting media. In Figure 4.5, the vertical gray bar marks the range of the critical pressure P_c of the first structural deformation. The vertical red dashed line marks the critical pressure of the structural phase transitions in the case of using argon and CsI as pressure transmitting media, and the vertical blue dashed line marks the critical pressures of the structural phase transitions for using helium and alcohol mixture. The values of the critical pressure are estimated for various pressure transmitting media at the points, which are marked by the vertical red and blue dashed lines. For argon and CsI, P_c is slightly lower compared to helium and the alcohol mixture. Helium and alcohol mixture have better hydrostaticity comparing to argon and CsI. The solidification pressure is above 10 GPa in case of helium and alcohol mixture. In contrast, argon solidifies at very low pressure around

	helium	alcohol mixture	argon	CsI
Critical pressure	$P_c \approx 3$ GPa	$P_c \approx 3$ GPa	$P_c \approx 2$ GPa	$P_c \approx 2$ GPa

Table 4.2: *P_c values for using helium, alcohol mixture, argon and CsI as a pressure transmitting media.*

1.3 GPa and the CsI is already solid at ambient conditions. Therefore, the P_c value slightly changes with the pressure transmitting medium used. The critical pressure P_c values depends on the degree of hydrostaticity in the diamond anvil cell (DAC). Using solid pressure transmitting medium (CsI) produces the least hydrostatic condition in the DAC as compared to alcohol mixture or helium. Therefore, the P_c value is lower in the case of using CsI as a pressure transmitting medium compared to helium and alcohol mixture. The anomaly is more obvious from calculating the derivative of the energy of the optical transition as a function of pressure (see Figure 4.6). This figure illustrate the derivative of the optical transitions S_{11}, $S_{22}(1)$, $S_{22}(2)$, $M_{11}(2)$ as a function of pressure for the various pressure transmitting media used. The anomaly is seen obvious clearly for $S_{22}(1)$, $S_{22}(2)$, $M_{11}(2)$ optical transitions for all media used (CsI, argon, alcohol mixture and helium). Kuntscher demonstrated that "except for helium as pressure transmitting medium there is a spread in the critical pressure for the various optical transitions; we attribute this spread to nonhydrostatic loading conditions during the pressure runs. The S_{11} transition does not show an anomaly and is thus not a good indicator for the pressure-induced structural phase transition, independent of the pressure transmitting medium used [91]." It is also clear from Figure 4.6 that the anomaly occurs at ≈ 2 GPa for argon and CsI as pressure transmitting media, whereas for helium and alcohol mixture it is found at ≈ 3 GPa. In the case of helium as the pressure medium, the anomaly is more clear, because the absorption band transitions are narrower. Helium is the best hydrostatic pressure medium known, thus the various contribution of the optical transition appear clearly and can be fitted better.

Figure 4.7 shows the relative changes of the energy of the optical transitions with respect to the lowest pressure for using different pressure transmitting media. It can be seen, that the pressure-induced changes are comparable for different pressure transmitting media. It is interesting to note that the pressure-induced shift is more obvious for certain optical transitions, for example, the anomaly is least obvious for the S_{11} transitions. It is also clear from Figure 4.7 that the relative shifts of the S_{22} and M_{11} optical transitions suddenly increases at $P_c \approx 3$ GPa. Kazaoui *et al.* showed that the optical transitions of semiconducting tubes vanish at the pressure of about 4.1 GPa while the transitions corresponding to the metallic tubes persist in the optical

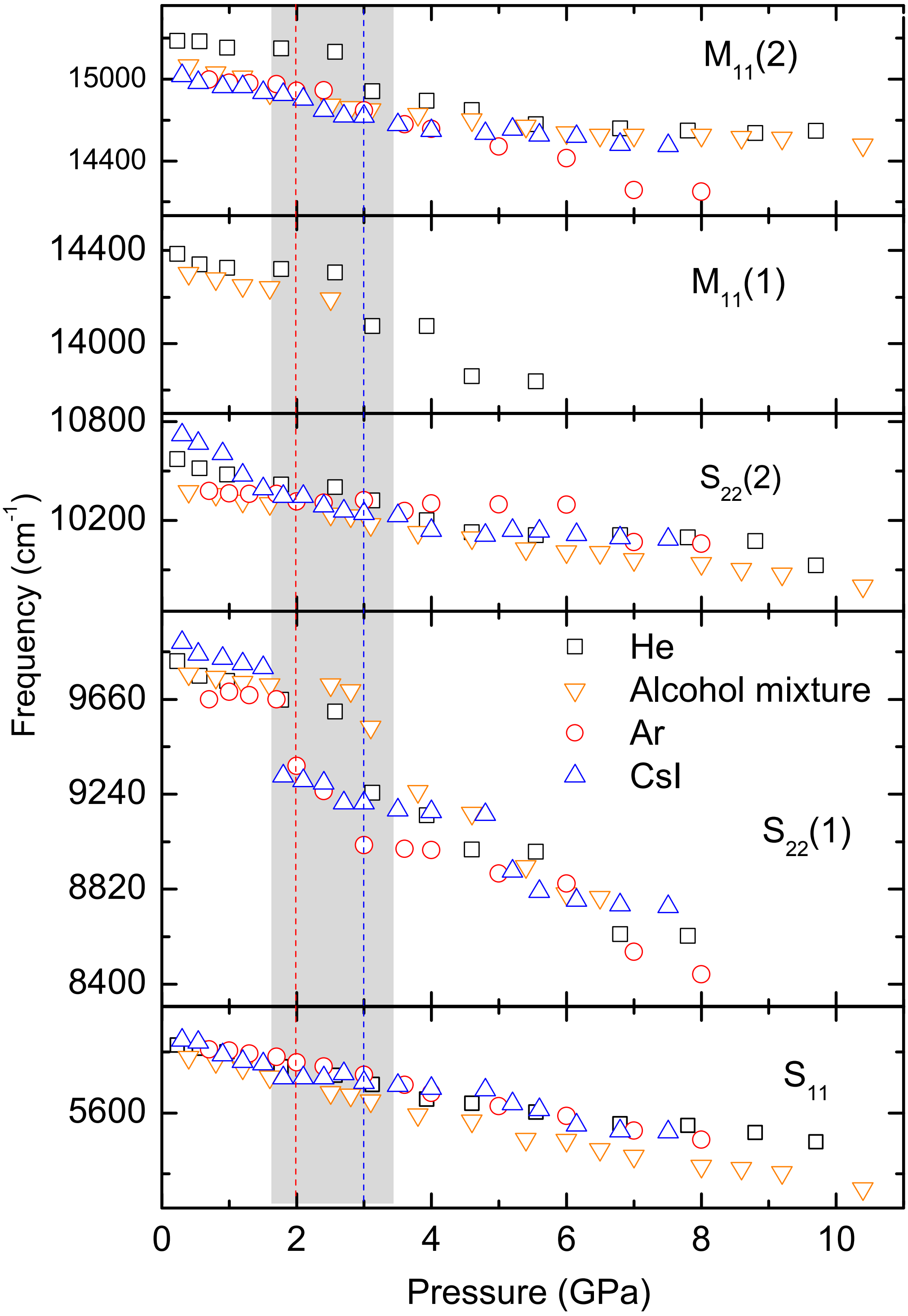

Figure 4.5: *Pressure dependence of the optical transition energies obtained from the absorbance spectra measured using helium (black squares), alcohol mixture(orange triangles) argon [2] (red circles) and CsI (blue triangles) as pressure transmitting medium [51].*

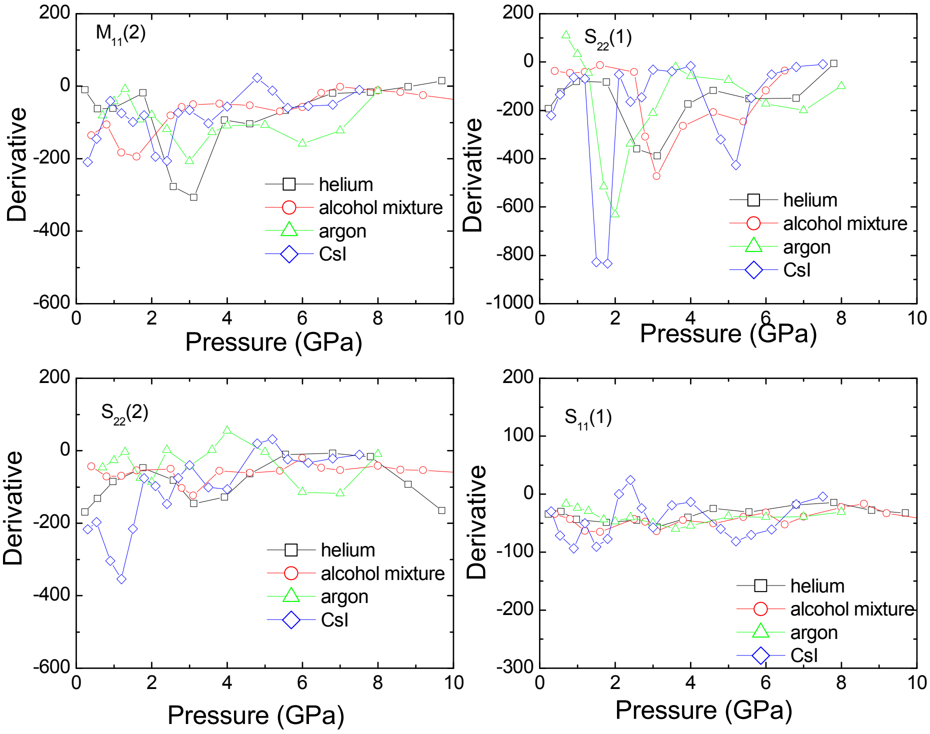

Figure 4.6: *The derivative of the energy of the optical transition versus pressure for using helium, alcohol mixture, argon [2] and CsI as pressure transmitting media.*

absorption spectra [46]. In our results, the optical transitions as a function of pressure are very similar for both semiconducting and metallic nanotubes. Thus, metallic and semiconducting SWCNTs respond to pressure in a very similar way, in contrast to the earlier report of Kazaoui *et al.* (see Figure 4.7).

Recent theoretical investigations on the nature of the changing of a circular cross section of the SWCNTs found that the SWCNTs with smaller diameter (less than 2.5 nm) undergo a radial deformation at certain pressure but hardly collapse, in contrast to tubes with larger diameters [31, 36, 37, 40, 41]. Accordingly, we attribute the observed anomaly in the pressure-induced shift to the deformation of the tubes, where the circular cross-section is changed to an oval shape [31]. This interpretation is also in agreement with that of recent experimental findings under pressure [51]. The expected value of the critical pressure P_c for the structural phase transition can be estimated for the tube diameters (1.2 - 1.4 nm) in the studied nanotube films to ≈ 2 GPa [31]. In our experimental results, an anomaly at P_c=2-3 GPa and the pressure spread are in good agreement with theoretical predictions. Our results and their interpretation are also validated by recent pressure-dependent Raman data [31,39–41].

It is also clear from Figure 4.7 that the value of the critical pressure P_c is affected by the pressure transmitting medium: For argon and CsI it is lower compared to helium and alcohol mixture because of the better hydrostaticity in case of helium and alcohol mixture. The spread of P_c seems to depend on the pressure transmitting medium as well; both the degree of hydrostaticity and the effect of adsorption might play a role for the spread of P_c values. Furthermore, our experimental results showed a good agreement with the results on films of as-grown SWCNTs [3]. The observation of an anomaly in case of as-grown SWCNTs by Thirunavukkuarasu *et al* [3] showed that the purification processes of the SWCNTs has no big effect on the critical pressure. The P_c value is not affected by the bundling of the tubes which might cause a nonuniform compression [3,51].

Resonant Raman studies on individualized nanotubes under pressure report the values P_c=10 GPa and 4 GPa for nanotubes with diameters 0.8-0.9 nm and 1.2-1.3 nm, respectively [30]. Although slightly higher, these values lie in the theoretically expected critical pressure regime [31]. On the other hand, several experimental results have proved that there is no signatures of a significant deformation up to very high pressures in bundled nanotubes [52,53]. For example, no anomaly was observed in the resonant Raman spectra of carbon nanotubes for pressures up to 40 GPa [52]. It was suggested that the anomaly is not observed because of the adsorption of argon used as pressure transmitting medium. These recent measurements on purified nanotubes suggest confidently the role of the pressure transmitting medium in determining the critical pressure of the structural phase transition due to adsorption effects [52]. In contrast to these reports, we observed the anomaly in the pressure dependence of the optical absorption bands for four different pressure transmitting media. Of course our observation of an anomaly does not exclude the physical adsorption of argon or helium on the SWCNTs during our pressure measurements.

4.1.2 High pressure regime

Resonant Raman studies on SWCNTs under pressure report the values P_c=9 GPa for nanotubes with diameters 1.1-1.3 nm, [57,91,92]. Kuntscher *et al.* [91] observed an anomaly above 4 GPa from optical spectroscopy measurements. It is seen in Figure 4.7 that the second anomaly is observed at P=5 GPa for CsI as pressure transmitting medium and P=6 GPa in case of helium, argon, and alcohol mixture. In case of

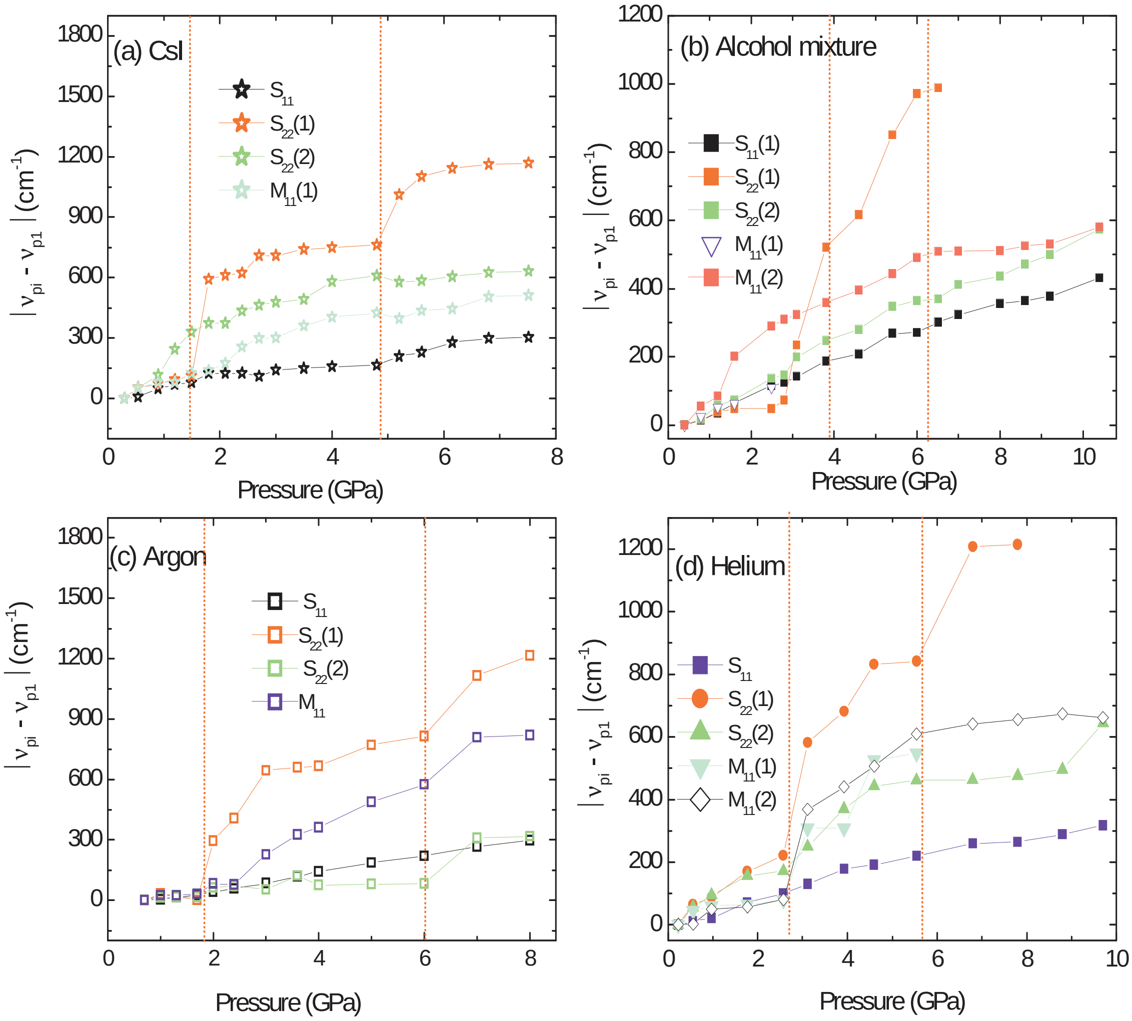

Figure 4.7: *Pressure-induced energy shifts of the optical transitions with respect to the lowest pressure, calculated as the difference between the energy of the transition, ν_{pi} , at a certain pressure p_i, and the corresponding energy at the lowest applied pressure, ν_{p1} ,for (a) CsI, (b) alcohol mixture, (c) argon [2], and (d) helium as pressure transmitting medium. The labels of the optical transitions are according to Figure 4.5. The vertical dashed lines mark the critical pressure of the second structural phase transition [51].*

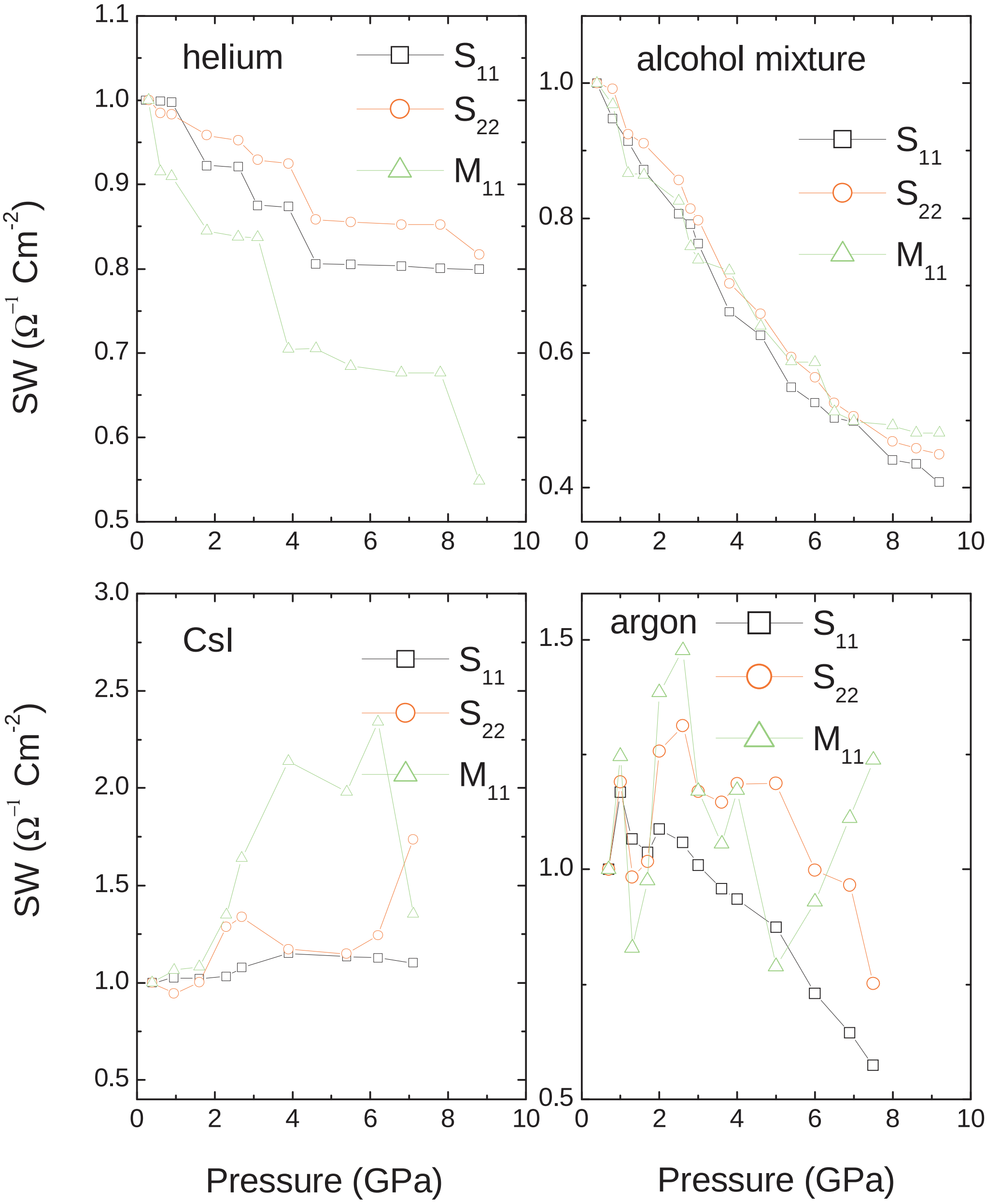

Figure 4.8: *Spectral weight of several absorption bands as a function of pressure when we use helium, alcohol mixture, argon [2] and CsI as a pressure transmitting media [51].*

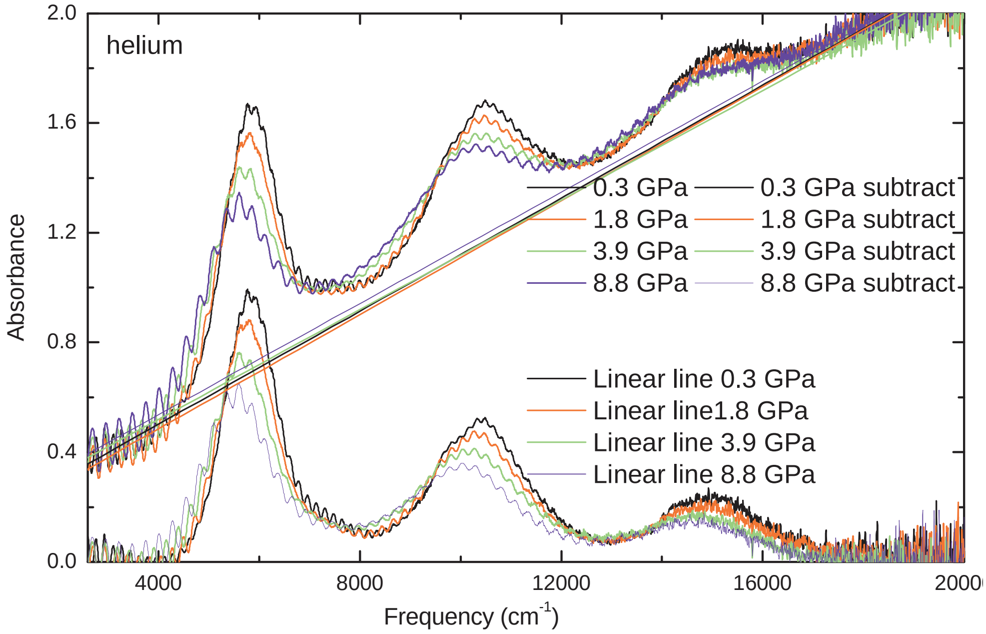

Figure 4.9: *Absorption spectra of purified unoriented carbon nanotube film at different pressure together with the linear Individuals background subtracted spectra, when we use helium as a pressure transmitting medium.*

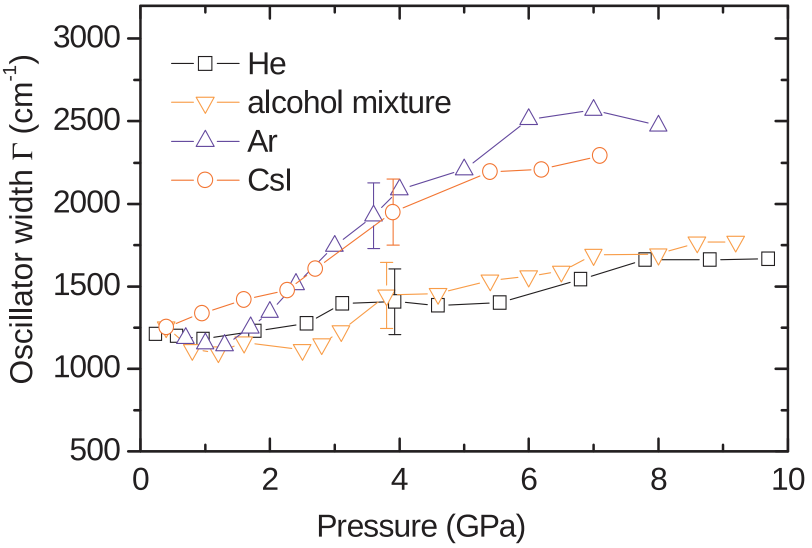

Figure 4.10: *Oscillator width of the S_{11} optical transition as a function of pressure, when we use helium, alcohol mixture, CsI and argon [2] as a pressure transmitting media [51].*

using CsI as pressure transmitting medium, the second anomaly is observed at lower critical pressure P=5 GPa compared to argon, alcohol mixture and helium as a pressure transmitting medium which is due to the less hydrostatic conditions in case of CsI.

Raman scattering experiments [57, 92] found an anomaly at ≈ 2.5 GPa in the shift of the tangential modes (G band) as well as in the intensity and the full-width-at-half-maximum of the radial breathing mode. This anomaly at 2.5 GPa was assigned to the change of the nanotubes shape from circular to oval or ellipse-like. This is the signature for the start of a structural transition in the nanotubes. Also a second anomaly at ≈ 9 GPa was observed as a plateau in the pressure-induced shift of the G band [57, 92]. This second anomaly was attributed to a more drastic change in cross section from an ellipse-like to race-track or peanut-type shape. In our experimental results, the observation of two anomalies has been interpreted by Kuntscher *et al.* [91] in following way. The first anomaly at P_c=2-3 GPa is due to the start of the structural phase transition and the second anomaly at 5-6 GPa is due to a more drastic deformation of the nanotubes cross section.

Since the dimensionality of the system might change with the application of pressure, it is important to present the spectral weight of the S_{11}, S_{22}, and M_{11} absorption bands as a function of pressure for using helium, alcohol mixture, argon and CsI as the pressure transmitting media (see Figure 4.8). In order to obtain very accurate spectral weight values, we subtracted the linear background individually for all spectra (see Figure 4.9). It is obvious from Figure 4.8 that the spectral weights for all bands decrease with increasing pressure in case of helium and alcohol mixture, which suggests that the dimensionality of the system departs from one-dimensional upon pressure application. As a result the singularity in the density of states typical for one-dimensional systems smears out towards a step-like behavior expected for two-dimensional systems. In this case, the spectral weight of the inter-band transitions is distributed over much wider energy range. Thus, the spectral weights for all absorption bands decrease with increasing pressure. The spectral weights as a function of pressures show scattering in the case of using argon and CsI as pressure media. In Figure 4.10, we show the width of the S_{11} optical transition as a function of pressure for using different pressure transmitting media. In case of using helium and alcohol mixture, the width of the absorption band S_{11} is much smaller compared to using argon and CsI, which is due to better hydrostaticity for helium and alcohol mixture. Clearly from the Figure 4.10, the oscillator width suddenly increases at around 1.5 GPa for using argon as the pressure medium.

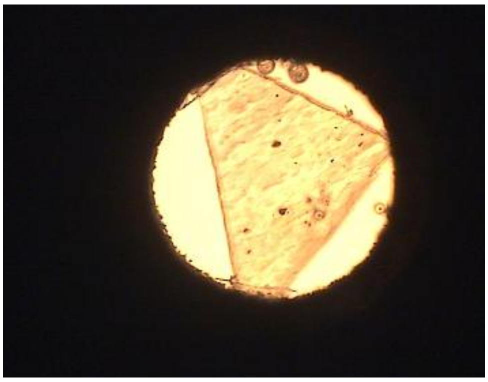

Figure 4.11: *Typical view of the DAC loaded with oriented nanotube sample and ruby spheres immersed in alcohol mixture as a pressure transmitting medium.*

4.2 Oriented SWCNTs in polyethylene matrix

The polarization-dependent investigations on the oriented nanotubes embedded in the polyethylene matrix were performed for pressures up to 8 GPa using argon, CsI and alcohol mixture as pressure transmitting media over the frequency range 2000-20000 cm^{-1}. Figure 4.12 shows the absorption spectra of the oriented SWCNTs film embedded in the polyethylene matrix at the highest and lowest pressure. Obviously, the optical response of the nanotubes-polymer matrix is highly anisotropic for the polarization of the incident light E $\|$ alignment direction and for E $\perp$ alignment direction.

The optical absorption in carbon nanotubes is strongly suppressed by the depolarizing fields for light polarized in transverse directions as it is seen in Figure 4.12 [5,9,26]. For the electric field applied along the tubes, the effect of the charges induced along the tube direction is negligible, and the electric field parallel to the cylinder length is equal to the applied field. In contrast, for the electric field applied perpendicular to the tube axis, the charges are induced on the cylinder walls. The resulting polarization vector opposes the external field and therefore reduces the net field perpendicular to the cylinder length. This strongly affects the optical absorption perpendicular to the tube axis. The weak intensity of the spectra for E $\perp$ alignment direction is due to the contributions from 10% of the unoriented tubes present in the matrix and the leakage from the non-perfect polarizer.

Upon pressure application all the observed optical absorption peaks shift towards lower energies, while at the same time significant relative intensity changes take place. The pressure-induced broadening of the absorption bands is smallest in case of argon

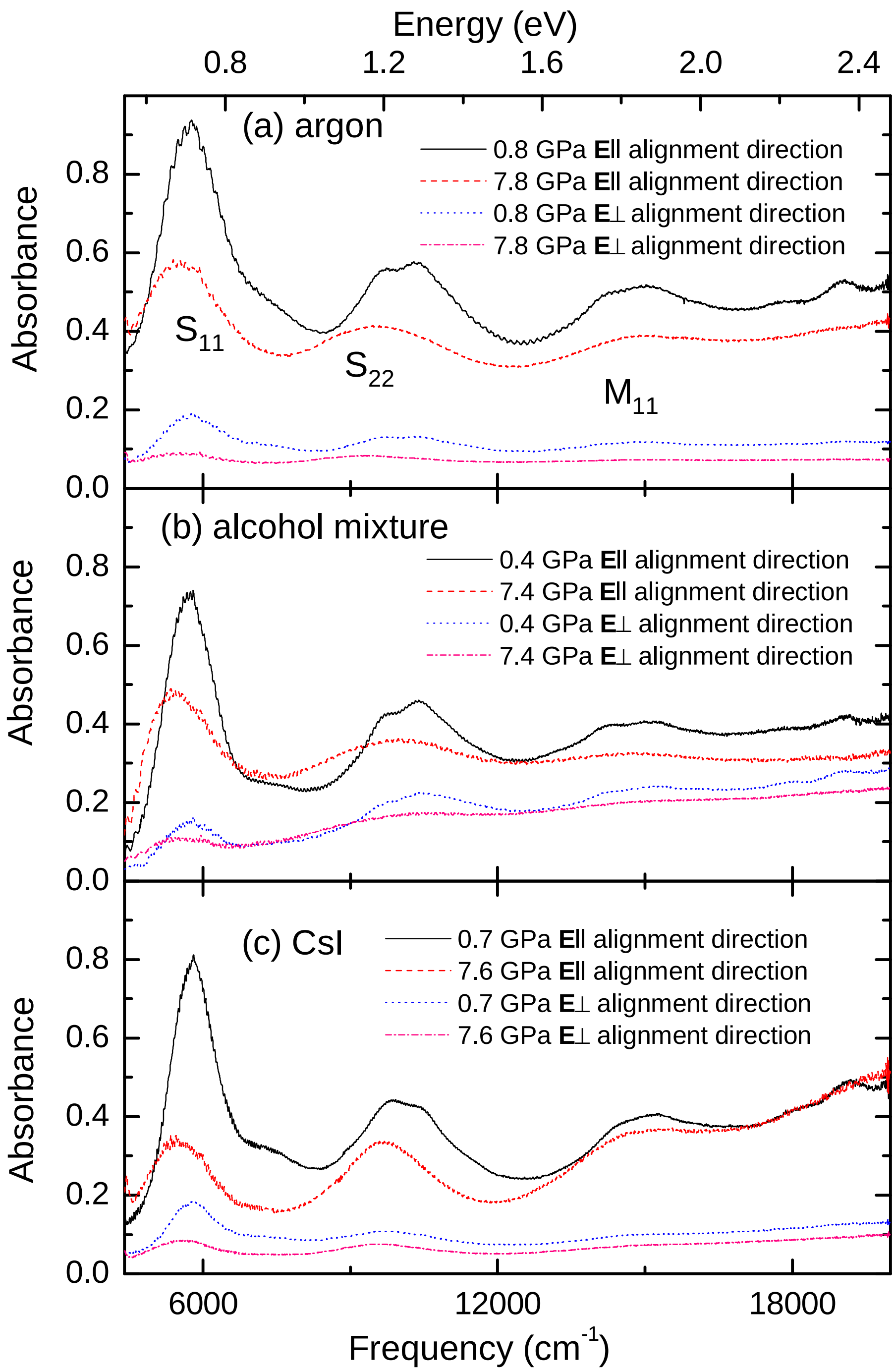

Figure 4.12: *Absorption spectra of oriented carbon nanotube films at low and high pressure for using (a) argon, (b) alcohol mixture and (c) CsI as pressure transmitting medium. The labels S_{ii} and M_{ii} denote the optical transitions between pairs of van Hove singularities in semiconducting and metallic SWCNTs, respectively, where the indices ii indicate the energy sequence of the involved van Hove singularities.*

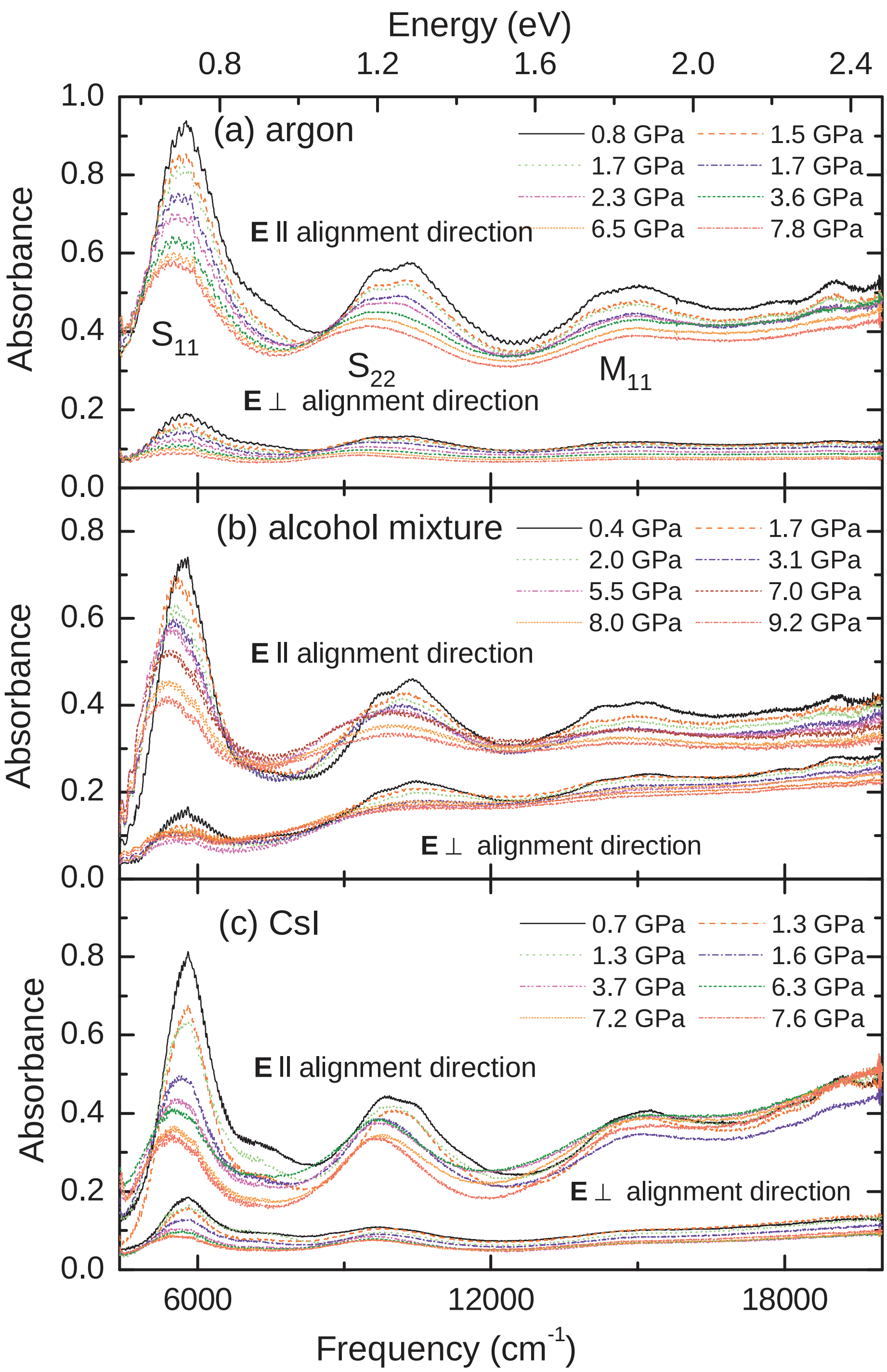

Figure 4.13: *Absorption spectra of oriented carbon nanotube films at various pressures (a) argon, (b) alcohol mixture and (c) CsI as a pressure transmitting medium.*

and alcohol mixture as pressure transmitting medium because of the better hydrostaticity, and this is consistent with the earlier study on the unoriented CNTs [3, 51]. Obviously, the electronic properties of the oriented SWCNTs are strongly affected by pressure in the entire measured frequency range for E $\parallel$ alignment direction (Figure 4.13).

The optical absorption bands S_{ii} and M_{ii} located above 4000 cm^{-1} were shifted to lower frequencies and broadend for E $\parallel$ alignment direction. Quantitative information on the energies of the optical transitions was obtained according to the following procedure. The spectra were fitted with Lorentz functions for E $\parallel$ alignment direction at the lowest pressure. The absorbance spectra for E $\perp$ alignment direction consist of low intensity absorption bands due to the 10 % randomly-oriented nanotubes, and demonstrate exactly the same behavior. Therefore, we omit their analysis here. Due to the nanotube diameter distribution in the sample, one observes a spread in the excitation energies of the different optical transitions [27]. We can clearly resolve two Lorentzian contributions for the S_{22} and M_{11} and S_{33} transitions. For the lower-lying S_{11} transitions the spread in energy is smaller [27] and thus not resolvable in our spectra as shown in Figure 4.14 (i).

It is noted that the absorption spectra for the oriented shown in Figure 4.12 are almost the same at lowest pressure for using different pressure transmitting media. With increasing pressure, the S_{11}, S_{22} and M_{11} transitions show reasonable intensity up to 8 GPa. We can clearly resolve two Lorentzian contributions for the S_{22} and M_{11} transitions for all pressure media (see Figure 4.14 (i)). Above 2 GPa the $S_{22}(1)$ peak cannot be resolved from $S_{22}(2)$ in case of using CsI as a pressure transmitting medium, the same is valid for $M_{11}(1)$ and $M_{11}(2)$ transition, while we are still able to fit the S_{22} and M_{11} using two Lorentzian contributions at 2 GPa in the case of using argon and alcohol mixture as a pressure transmitting media. This effect is illustrated in Figure 4.14 (ii).

In order to see the effect of applying pressure on the oriented SWCNTs, the same procedure was followed as in Section 4.1. The energies of the absorption bands obtained by the Lorentzian fitting as a function of pressure are plotted in Figure 4.15 (i). There are three important effects caused by applying pressure on the oriented SWCNTs:

1. The optical transitions show a red-shift with increasing pressure up to 8 GPa.
2. Anomalies are observed in the pressure-induced shift at P_c=2-3 GPa and at P_c=5-6 GPa [91].
3. The value of P_c depends on the pressure transmitting medium used: For alcohol mixture, P_c is slightly higher ($P_c \approx$ 3 GPa) compared to argon and CsI ($P_c \approx$

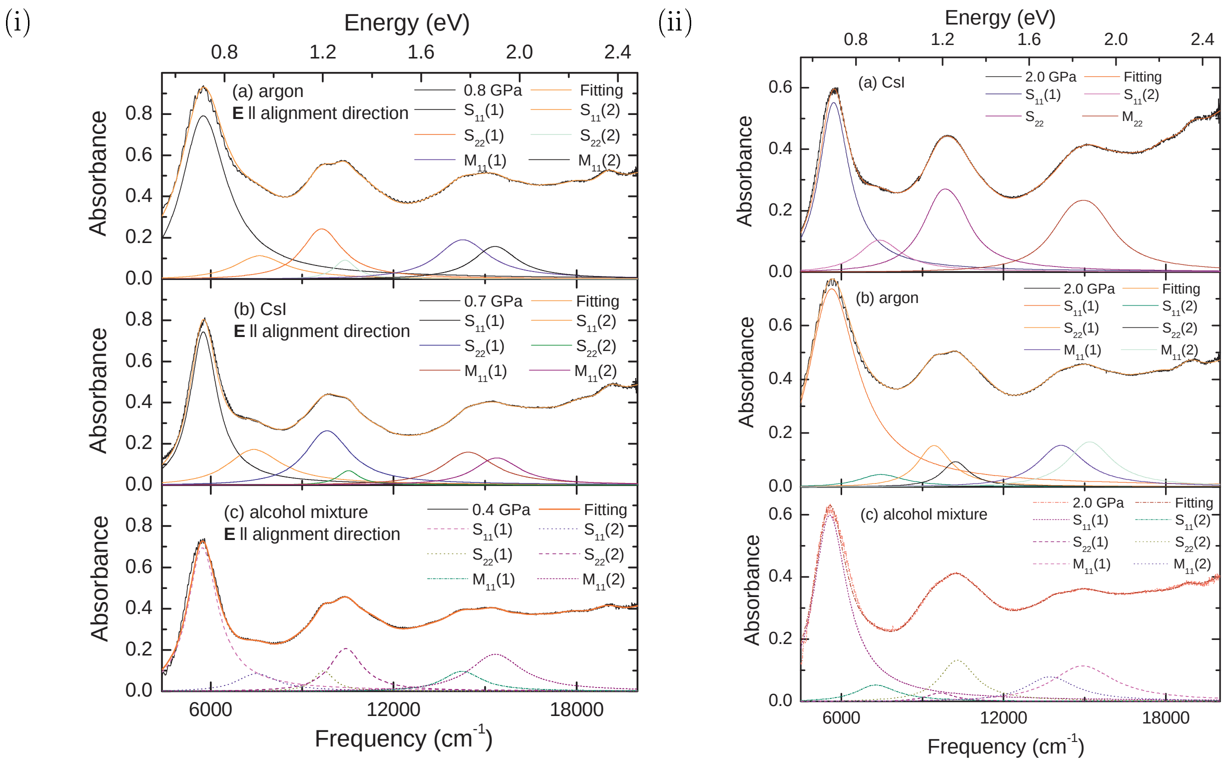

Figure 4.14: *(i) Fit of the measured absorption spectrum of the oriented SWCNT at low pressure and the fit with Lorentz functions. (ii) Fit of the measured absorption spectrum of the oriented SWCNT at 2 GPa and the fit with Lorentz functions.*

2 GPa).

These three important results were discussed in Section 4.1 for the unoriented SWCNTs. We attribute the shift of the optical transitions of the SWCNTs to lower energies to noticeable hybridization and symmetry-breaking effects arising from the pressure-induced deformation of the nanotubes. The observation of two anomalies at P_c=2-3 GPa and at P_c=5-6 GPa were explained by Kuntscher *et al.* as follows [91]: The first anomaly at is due to the start of the structural phase transition and the second anomaly at 5-6 GPa is due to a more drastic deformation of the nanotubes cross section.

The values of the critical pressure (the two anomalies) depend on the pressure transmitting medium used: The P_c values are obviously higher for using alcohol mixture as pressure transmitting medium compared to argon and CsI. We attribute this finding to the better hydrostaticity in case of the alcohol mixture as pressure transmitting medium. Under better hydrostatic conditions a higher critical pressure is expected,

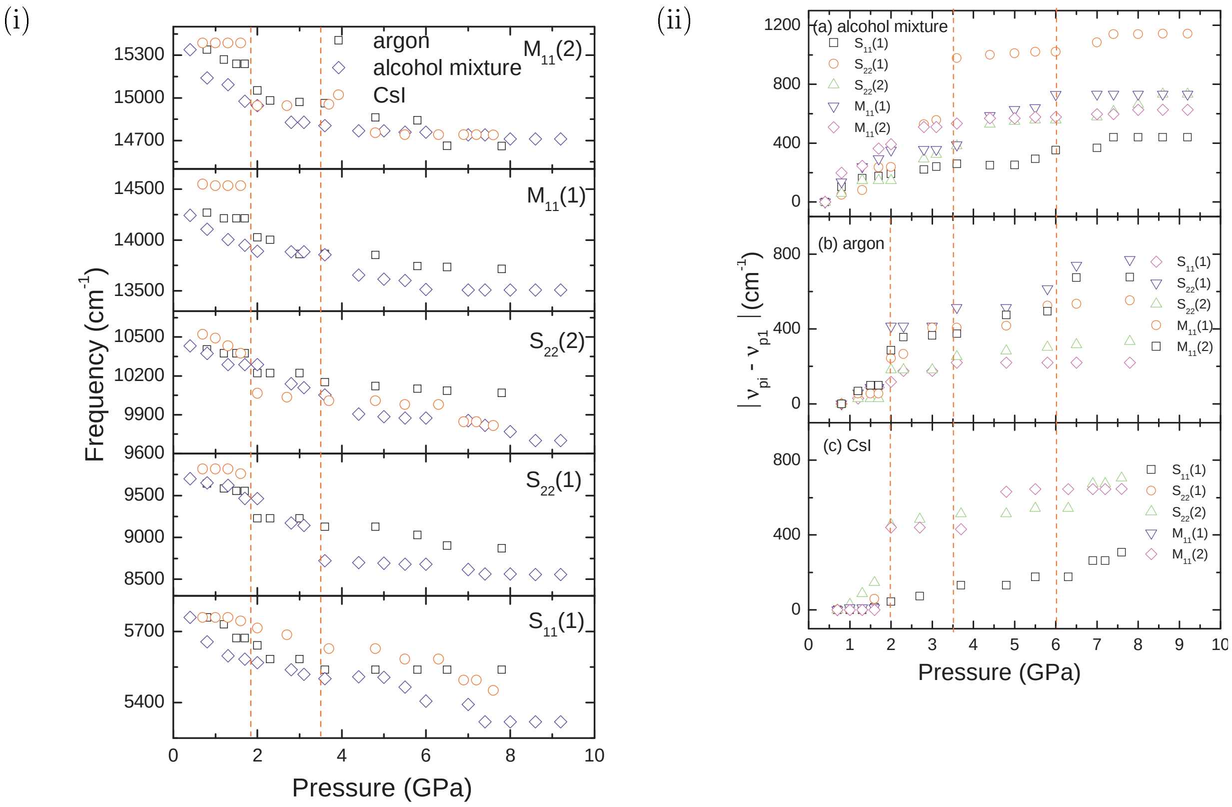

Figure 4.15: *(i) Pressure dependence of the optical transition energies obtained from the absorbance spectra. (ii) Relative energetic shifts of the optical transitions as a function of pressure for using (a) alcohol mixture, (b) argon and (c) CsI as a pressure transmitting media. The vertical dashed red lines mark the critical pressures of the first and second structural phase transitions.*

as observed in other cases. This results are consistent with the previous study on the unoriented CNTs [91]. The two anomalies are also illustrated by the relative shifts of the optical transition as a function of pressure presented in Figure 4.15 (ii), which also allows a comparison of the pressure behavior of the different types of optical transitions. It is obvious from this plot that metallic and semiconducting SWCNTs exhibit the same trend (see Section 4.1). Finally, Figure 4.16 shows the spectral weight as a function of pressure. The spectral weight decreases with increasing pressure which is probably due to loss of one-dimensionality under the application of high pressure.

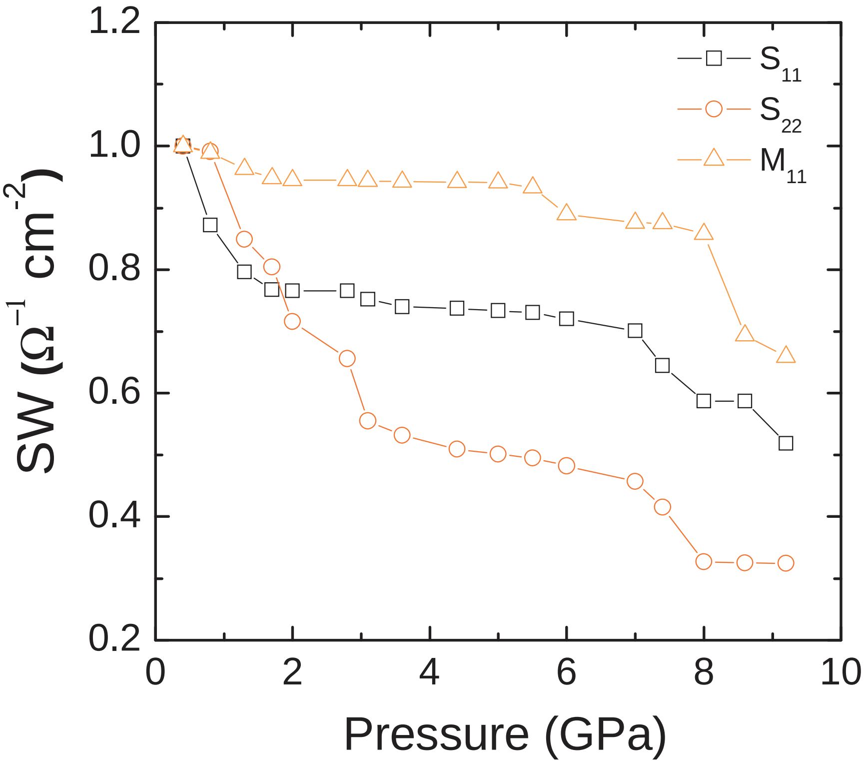

Figure 4.16: *Spectral weight as a function of pressure for using alcohol mixture as pressure transmitting medium.*

4.3 C_{60} peapods and double walled carbon nanotube

4.3.1 Ambient pressure

Figure 4.17 shows the NIR-Visible absorption spectra of SWCNTs C_{60} peapods, and DWCNTs at ambient pressure. The optical absorption features are assigned according to the previously introduced notations for the inter-band transitions across vHs in the DOS (see Section 4.1 for detailed information). Figure 4.17 reveals the optical transitions corresponding to both semiconducting and metallic nanotubes. The labels S_{11}, S_{22}, M_{11} and $S_{33/44}$ refer to the optical transitions of semiconducting or metallic tubes, with the subscripts according to the increasing energy of the involved electronic states. The spectrum also contains a strong absorption in the background of the optical transitions. This absorption corresponds to the π-plasmon at 5 eV due to the collective excitations of π electrons in the graphene sheet [27, 93]. The linear background from π-plasmon is subtracted as shown in Figure 4.17

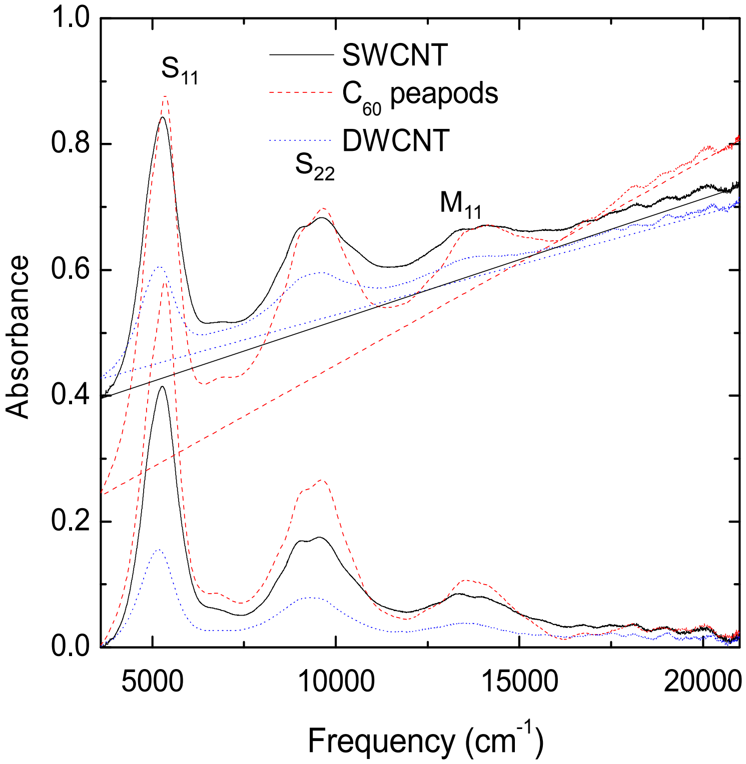

Figure 4.17: *Absorption spectra of carbon nanotube films SWCNTs, C_{60} peapods and DWCNTs. The labels S_{ii} and M_{ii} denote the optical transitions between pairs of van Hove singularities in semiconducting and metallic SWCNTs, respectively, where the indices ii indicate the energy sequence of the involved van Hove singularities.*

Figure 4.18 shows the background-subtracted absorbance spectra of the SWCNTs, C_{60} peapods and DWCNTs films at ambient conditions together with the fitting curve and its components. The different components of the principle transitions observed in the absorbance spectra correspond to the various contributions from the nanotube bundles with different diameter and chirality distributions. Note that the spectrum for the intermediate C_{60} peapods shown in Figure 4.18 is almost identical to the spectrum of the SWCNTs. For DWCNTs, the optical absorption of inner tubes with 0.7 nm diameters will overlap with those of outer tubes. In the spectra, three strong optical absorption bands at 0.6-0.67 eV, 1.04-1.2 eV, and 2.05 eV can be observed, and these are assigned to the first and second singularities of semiconducting tube (S_{11} and S_{22}) and the lowest absorption peak of the metallic tubes (M_{11}).

For a better distinction, the spectrum is divided into four regions corresponding

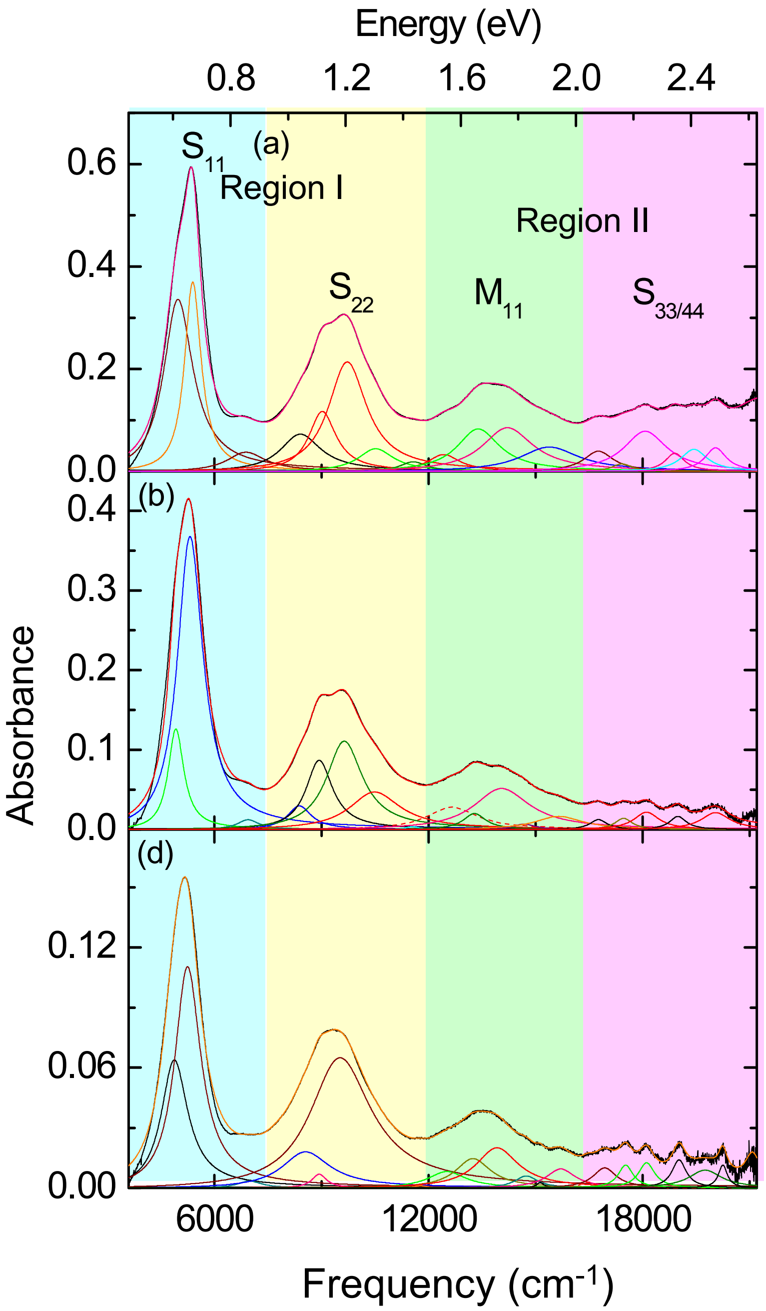

Figure 4.18: *Background-subtracted absorbance spectra of (a) SWCNTs and* C_{60} *peapods, (b)SWCNTs and (c) DWCNTs films at ambient pressure together with the fit of the optical transitions using Lorentzian oscillators. Only the strong transitions are considered and labeled.*

S_{11}	SWCNTs	C_{60} peapods	DWCNTs
$S_{11}(1)$	0.62 eV	0.6 eV	0.6 eV
$S_{11}(2)$	0.67 eV	0.66 eV	0.65 eV
$S_{11}(3)$	0.86 eV	0.86 eV	0.86 eV

Table 4.3: *List of the S_{11} optical transitions of the SWCNTs, C_{60} peapods and DWCNTs.*

S_{22}	SWCNTs	C_{60} peapods	DWCNTs
$S_{22}(1)$	1.04 eV	1.04 eV	1.04 eV
$S_{22}(2)$	1.11 eV	1.11 eV	1.11 eV
$S_{22}(3)$	1.2 eV	1.2 eV	1.2 eV
$S_{22}(4)$	1.35 eV	1.35 eV	1.35 eV

Table 4.4: *List of the S_{22} optical transitions of the SWCNTs, C_{60} peapods and DWCNTs.*

to the absorption bands of different origin. Regarding the absorption bands at 0.6-0.86 eV associated with the S_{11} of the outer tubes, three Lorentzian contribution were used for fitting S_{11} transition as shown in Figure 4.18. For the transitions $S_{11}(1)$, the peak positions for C_{60} peapods and DWCNTs are obviously downshifted as compared to the SWCNTs. The amount of the shift of the $S_{11}(2)$ transitions for C_{60} peapods and DWCNTs, are 0.01 eV and 0.02 eV respectively. There is no downshift for $S_{11}(3)$ transitions (see Table 4.3). However, the line-width is slightly wider for DWCNTs than for SWCNTs. The energies of the optical transition S_{11} are shown Table 4.3. Other peaks observed at 1.04 eV to 1.35 eV do not change their positions (see Table 4.4). Four contributions were used for fitting S_{22} transition.

As mentioned earlier, noticeable peak shifts are only observed in the absorption band S_{11} (the 0.62 eV and 0.67 eV bands). The absorption band observed experimentally for SWCNTs 0.68 eV for S_{11} transition is somewhat higher than the theoretically calculated $S_{11} \approx 0.6$ eV for the ≈ 1.4 nm tube) [27]. The electronic structures of C_{60} peapods were theoretically investigated by Okada *et al.* [94,95], where the downshift of the electronic levels toward the Fermi energy E_F for C_{60} peapods have been observed. The hybridization between the C_{60} π states and nearly free electron states of SWCNTs was observed for C_{60} peapods.

The shift of the optical transitions to lower energies was generally attributed to the hybridization between the C_{60} π states and nearly free electron states of SWNTs [94, 95]. Furthermore, the effect of hybridization between the C_{60} π states and nearly free electron states of SWCNTs was suggested as the mechanism responsible for the electron transfer from π orbital's of the SWCNTs to the interstitial space between the SWCNTs and C_{60}. According to their a density functional theory calculation, Okada *et al.* [94, 95] suggested that the occupied π band of the SWCNTs shifts toward E_F by about 0.1 eV, while on the other hand, a downshift of the electronic levels of C_{60} peapods towards E_F occurs.

Similar behavior was also reported in the study of the band-gap changes for DWCNTs by Okada *et al.* [96]. The rehybridization between the π states and σ states of each nanotube was observed for $(7,0)@(17,0)$ and $(7,0)@(19,0)$ DWCNTs. Okada *et al.* [96] observed that the $(7,0)@(16,0)$ is a metal, while $(7,0)@(17,0)$ is semimetal. Okada *et al.* [96] suggested an explanation for the observed downshift of the electronic levels toward Fermi energy E_F. The changes of the band-gap is due to the noticeable rehybridization between π and σ states of each nanotube as well as the inter-wall spacing and curvature difference between the inner-and outer-tube [96].

In addition, C_{60} peapods and empty single-walled carbon nanotubes with diameter ranged from 1.22 to 1.6 nm, as well as double-walled carbon nanotubes obtained from C_{60} peapods, were experimentally investigated by vis-NIR and Raman spectroscopy [97]. According to the experimental investigation, Ryabenko *et al.* [97] suggested an explanation for the observed downshift of the optical transitions to lower energies as a results of the filling of nanotubes with C_{60} changes "the average diameter of the electron cloud around SWCNTs. This cloud increases for thin SWCNTs, and decreases for thick ones [97]". Ryabenko *et al.* [97] observed that absorption bands of C_{60} peapods are downshifted compared to non-filled nanotubes with C_{60}.

Furthermore, Liu *et al.* [98] demonstrated that the shift of the optical transitions to lower energies in case of C_{60} peapods was generally attributed to the weak hybridization between the C_{60} π states and the SWCNTs π states. Liu *et al.* [98] observed that the overall shape of optical spectrum of the C_{60} peapods and the SWNTs is very similar. However, there are a noticeable differences in the fine structure i.e. the optical spectrums show small changes in the relative intensities, peak positions. The authors concluded that the optical transitions of the SWNTs are slightly downshifted to lower energies in case of C_{60} peapods as a results of a small increase of the SWNTs diameter by filling SWCNTs with C_{60} [98].

Apparently, the downshift of the optical transitions to lower energies in the case of C_{60} peapods and DWCNTs as compared with the empty SWCNTs can be attributed to the interaction of C_{60} and the inner tube with the outer tube. Chen *et al.* analyzed the linear optical properties of double-walled carbon nanotubes within the tight-binding model, the gradient approximation and the sum-over-state method [18]. They found

M_{11}	SWCNTs	C_{60} peapods	DWCNTs
$M_{11}(1)$	1.55 eV	1.55 eV	1.55 eV
$M_{11}(2)$	1.65 eV	1.65 eV	1.65 eV
$M_{11}(3)$	1.74 eV	1.74 eV	1.70 eV
$M_{11}(4)$	–	–	1.82 eV
$M_{11}(5)$	–	1.80 eV	1.87 eV
$M_{11}(6)$	1.90 eV	1.90 eV	1.94 eV

Table 4.5: *List of the M_{11} optical transitions of the SWCNTs, C_{60} peapods and DWCNTs obtained from the fit of the absorbance spectrum (shown in Figure 4.18).*

$S_{33/44}$	SWCNTs	C_{60} peapods	DWCNTs
$S_{33/44}(1)$	–	–	2.04 eV
$S_{33/44}(2)$	2.08 eV	2.08 eV	2.10 eV
$S_{33}(3)$	2.16 eV	2.16 eV	2.16 eV
$S_{33/44}(4)$	2.24 eV	2.24 eV	2.24 eV
$S_{33/44}(5)$	2.35 eV	2.35 eV	2.35 eV
$S_{33/44}(6)$	–	–	2.44 eV
$S_{33/44}(7)$	2.48 eV	2.48 eV	2.50 eV

Table 4.6: *List of the $S_{33/44}$ optical transitions of the SWCNTs, C_{60} peapods and DWCNTs obtained from the fit of the absorbance spectrum (shown in Figure 4.18).*

that absorption peaks may be slightly modified due to inter-tube interaction. In addition, many new absorption peaks are produced (see Table 4.5 and 4.6). Our studies also show these effects of inter-tube interaction. The experimental results may be explained, by the interaction of C_{60} and the inner tube with the outer tube. It is clear from Figure 4.18 that the a new absorption peaks appears in the case of C_{60} peapods at ≈ 1.8 eV and in the case of DWCNTs at ≈ 1.82 eV, 1.87 eV, 2.04 eV and 2.44 eV. Besides the appearance of the new absorption peaks, the S_{11} absorption peak around 0.67 eV is shifted by about 0.01 eV and 0.02 eV for C_{60} peapods and DWCNTs respectively.

Optical absorption due to the metallic outer tubes can be observed at 1.55-1.94 eV, and the small features observed in the range of 2.20-2.64 eV should be assigned to the absorption originating from S_{33} (see Figure 4.18). The energies of the optical M_{11} and S_{33} transitions are shown in Table 4.5 and 4.6 respectively. The number of contribution M_{11} and $S_{33/44}$ transitions is not the same for SWCNTs, C_{60} peapods and DWCNTs, most probably, because of the effect of C_{60} and interaction between the inner and outer tubes [18]. Chen *et al.* [18] observed that a new absorption peaks appear in the case of DWCNT at $\approx 0.3 - 0.4\ eV$. The absorption peak around 5.8 eV is reduced strongly in the case of DWCNT (see Section 2.3).

4.3.2 C_{60} peapods and double walled carbon nanotube under pressure

Upon pressure application all the observed optical absorbance peaks are shifted towards lower energies for SWCNTs, C_{60} peapods and DWCNTs, while at the same time significant relative intensity changes are taken place. The pressure dependence of the optical absorbance is illustrated in Figure 4.19. For a quantitative analysis of the pressure-induced changes in the optical transitions their energies were extracted from the absorbance spectra for all measured pressures using the same procedure as for the absorbance spectra of the unoriented and oriented SWCNTs [51] (background subtraction and fitting with Lorentzian functions, see Section 4.1 and 4.2).

Figure 4.20 illustrates the fitting curve and its components, after background-subtraction of the absorbance spectra for the SWCNT, C_{60} peapods and DWCNTs films at the lowest measured pressure. The fine structure of the absorption bands are observed in the spectrum at low pressure in case of SWCNTs and C_{60} peapods, but it is obscured in the case of the DWCNTs by the broadening of the absorption bands (see Figure 4.20). In the case of DWCNTs, upon pressure application the absorption bands are broadened, and thus one can resolve only one Lorentzian contribution for the S_{11}, S_{22} and M_{11} optical transitions. For the same reason, only the strong and most obvious transitions have been considered for the fitting using Lorentzian functions, and excellent fits were obtained. With increasing pressure, S_{22} transition and M_{11} transition in the case of SWCNTs and C_{60} peapods tubes display reasonable intensity attenuation. We can use two Lorentzian contributions for fitting the M_{11} optical transition and two Lorentzian contributions for fitting the S_{22} transition up to the highest applied pressure.

In the case of DWCNTs, the $S_{22}(1)$ cannot be resolved from $S_{22}(2)$. The same holds for the $M_{11}(1)$ and $M_{11}(2)$ transition, because the absorption bands are broadened by applying pressure (see Figure 4.20). Figure 4.21 (a) shows the absorption spectra of the SWCNTs, C_{60} peapods and DWCNTs at the lowest and the highest pressure. The pressure-induced changes in the energy of the optical transitions in the SWCNTs and C_{60} peapods are comparable to those of the unoriented and oriented CNTs, which are synthesized by laser ablation (see Section 4.1 and Section 4.2). The changes in the line width of the radial breathing mode of the empty nanotubes and the C_{70} peapods (C_{70} encapsulated single wall carbon nanotubes) under hydrostatic pressure were experimentally investigated by Raman spectroscopy [57]. Caillier *et al.* investigated the behavior of bundled C_{70} peapods by Raman spectroscopy and compared with the corresponding behavior of the nonfilled SWNT under hydrostatic pressure. He observed that "there is weak character of the fullerene-tube interaction below 2 GPa [99]". In our experimental results, the overall shift of the optical transitions to lower energies with increasing pressure has been observed in both empty SWCNTs and C_{60} peapods; "hence a stabilization of the SWCNTs by the filling with fullerene molecules is not obvious based on our results. This is in agreement with the interpretation of recent Raman measurements on C_{70} peapods under pressure, pointing out the weak character of the fullerene-tube interaction below 2 Ga [99]".

In general, the overall red-shift of the optical transitions is in qualitative agreement with the previous pressure-dependent studies on SWCNTs [46, 51, 90]. On the other hand, the energy-shift of the optical transition with respect to pressure is much smaller in case of DWCNTs. This discrepancy is most probably due to the inner tube [54,100]. Figure 4.21 (b) shows the relative changes in energies of the $S_{11}(1)$ transition in the SWCNTs film, C_{60} peapods and the DWCNTs film as a function of pressure. The maximum shift of the optical transitions with the application of pressures up to 8.5 GPa is around 100 cm^{-1}($\approx$ 0.012 eV) in the case of the DWCNTs, However it is around 500 cm^{-1}($\approx$ 0.06 eV) in the case of SWCNTs and C_{60} peapods films.

On applying pressure, the energy of the optical transitions show very small changes up to a certain pressure around 1.7 GPa in case of the SWCNT films (see Figure 4.22 (a)). Above this pressure, the energy of the optical transitions decreases more drastically with increasing pressure causing an anomaly. With the application of pressure, the circular cross-section of nanotubes deforms to stabilize at an oval shape (see Section 4.1). This radial deformation of the SWCNTs is discontinuous and occurs at a certain critical pressure P_c. The value of P_c follows the relation $P_c \propto 1/d^3$.

For nanotubes grown by arc discharge technique, with an average diameter of 1.4-1.5 nm, the critical transition pressure is expected in the range of 1.7-2 GPa [31, 35, 37, 38, 41]. This is in good agreement with our study of unoriented SWCNTs grown by laser ablation technique, with an average diameter of 1.2-1.4 nm (see Section 4.1) using the same pressure transmitting medium (alcohol mixture). We also observed anomaly around 3 GPa in case of the C_{60} peapods film (see Figure 4.22 (a)). The anomaly is obvious clearly by taking the derivative of the energies of the optical transitions (see Figure 4.23). This figure illustrate the derivative of the optical transitions S_{11}, $S_{22}(1)$, $S_{22}(2)$, $M_{11}(2)$ as a function of pressure for using alcohol mixture as a pressure transmitting medium. The anomaly is seen obvious clearly for $S_{22}(1)$, $S_{22}(2)$, $M_{11}(2)$ optical transitions. Kuntscher demonstrated that "the S_{11} optical transitions seem to

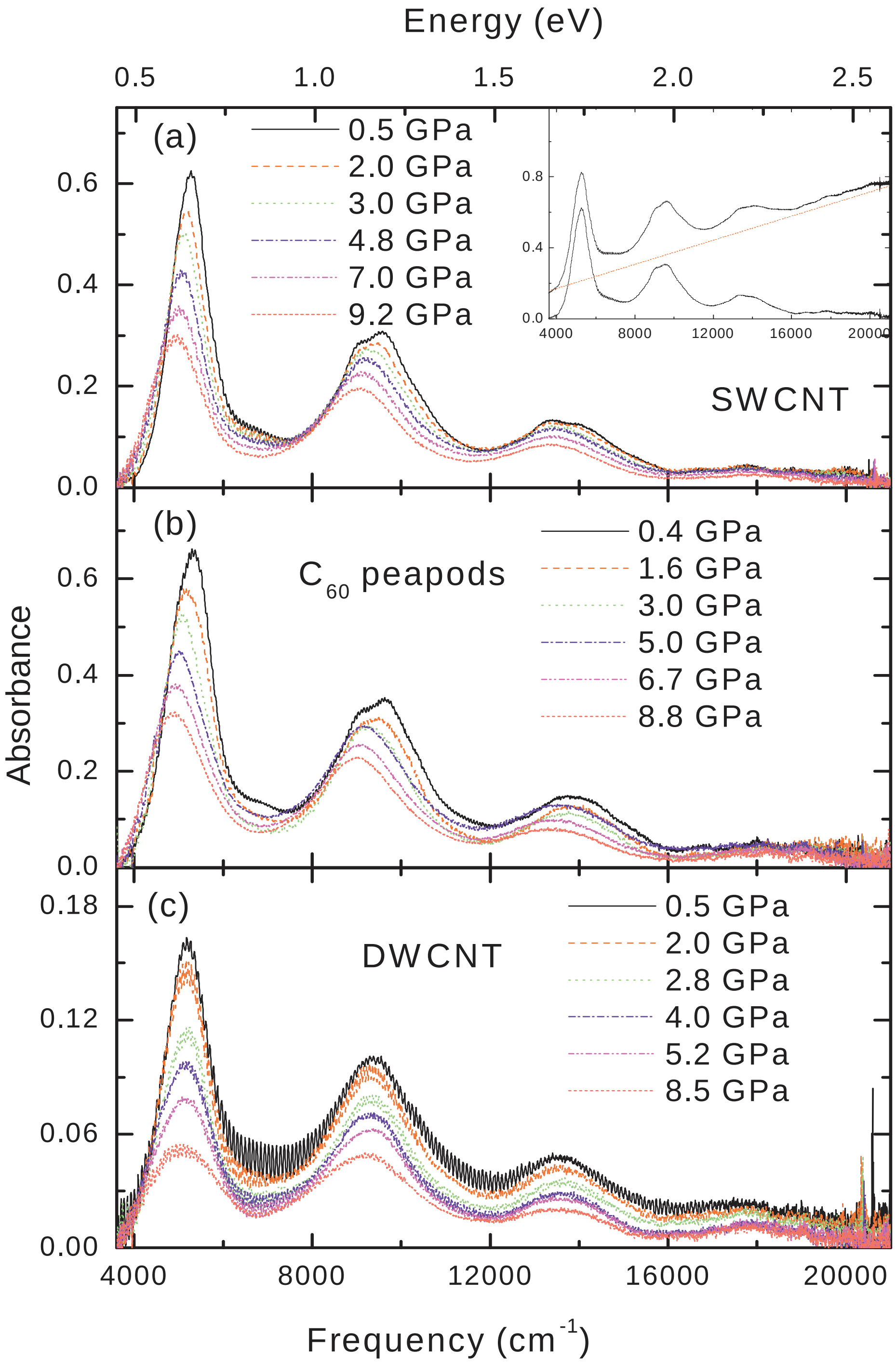

Figure 4.19: *Absorbance spectra of the SWCNTs, C_{60} peapods and DWCNTs for pressures up to 8.5 GPa. The interference fringes superimposed on the spectra are due to multiple internal reflections between the diamonds in the DAC. The inset shows the absorbance spectrum at low pressure together with the linear background and the absorbance spectrum after background subtraction.*

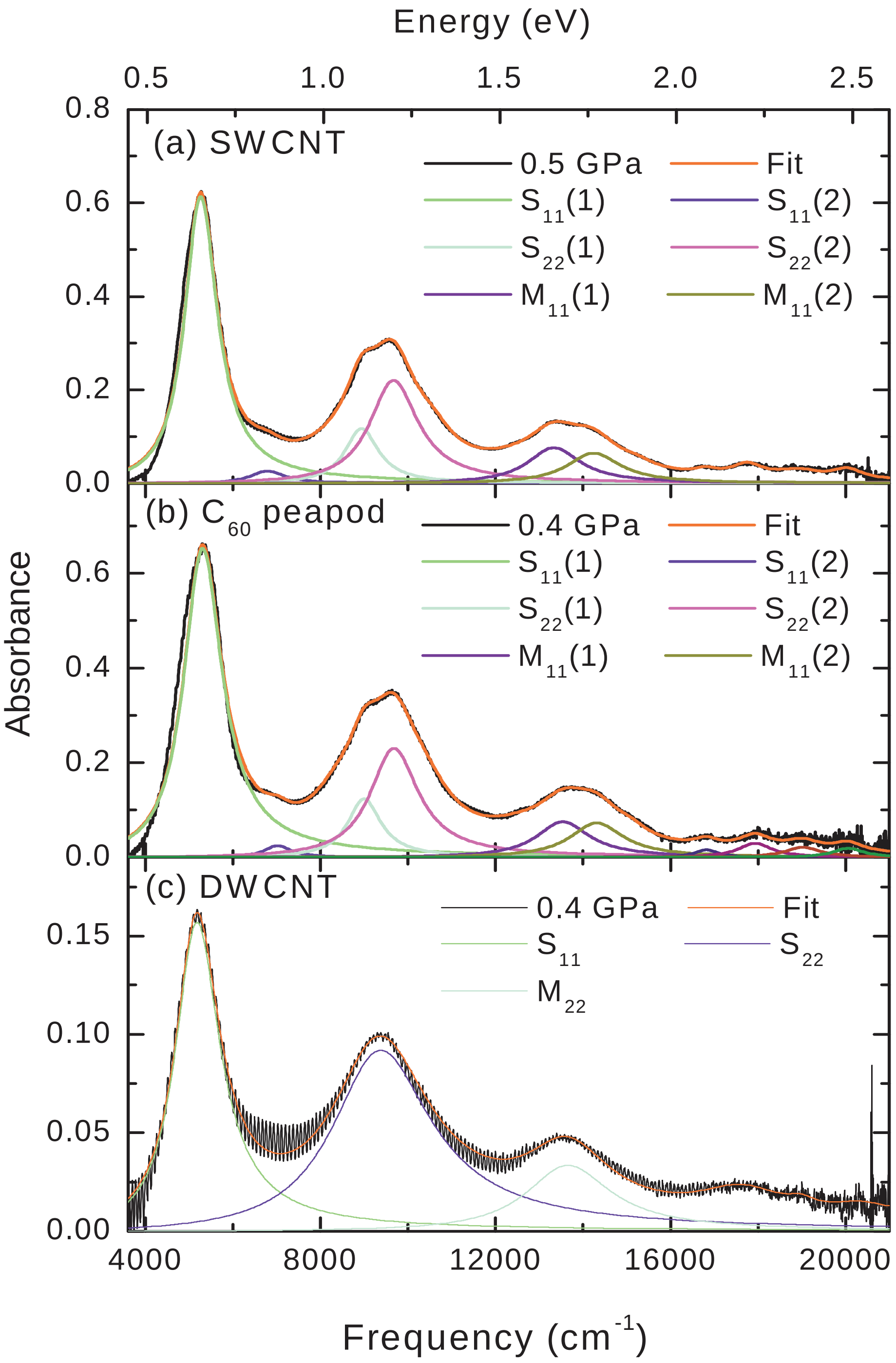

Figure 4.20: *Absorbance spectrum of the SWCNTs, C_{60} peapods and DWCNTs together with the Lorentz function fit and the fit components. The typical energy regimes of the optical transitions in the semiconducting (marked as S) and metallic (marked as M) tubes are represented.*

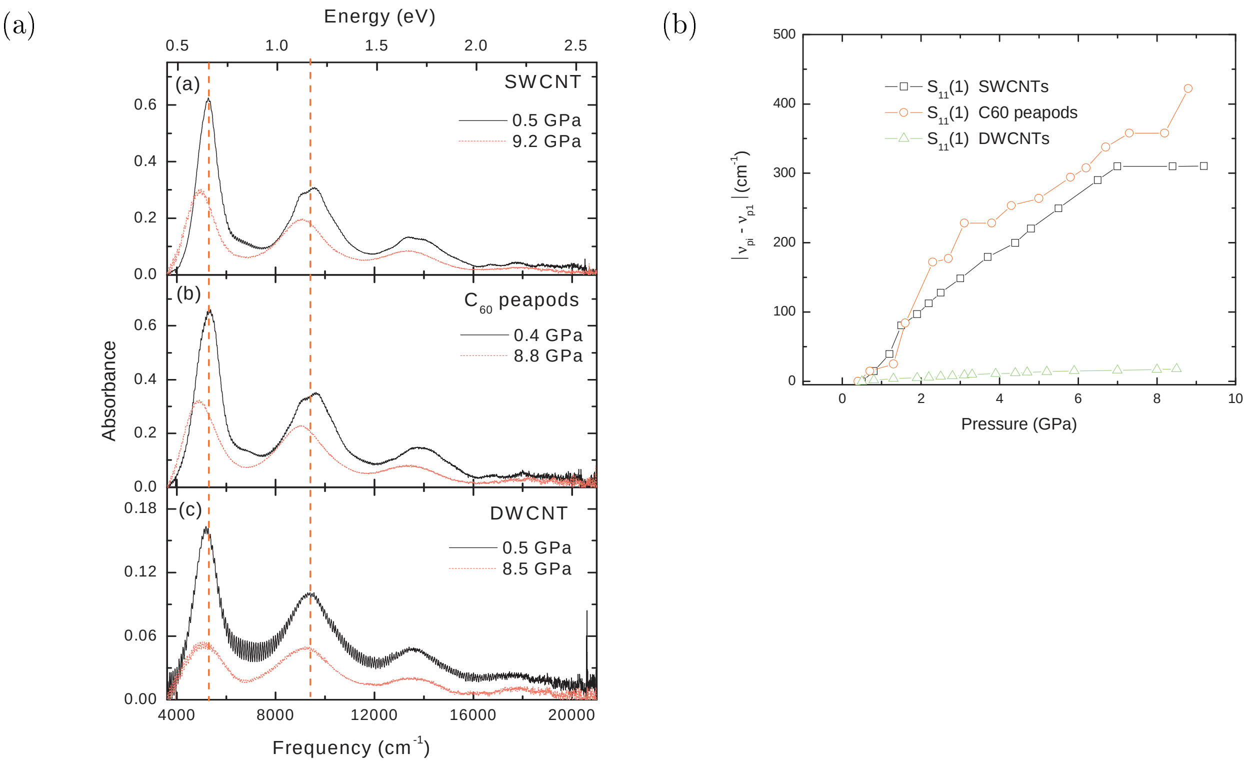

Figure 4.21: *(a) Absorbance spectra of the SWCNTs, C_{60} peapods and DWCNTs for the lowest and highest pressure. (b) Relative change in the energies of the S_{11}(1) optical transitions of the SWCNTs film, the C_{60} peapods film and DWCNTs as a function of pressure.*

be the least sensitive ones regarding the pressure-induced effects, and is thus not a good indicator for the pressure-induced structural phase transition [91,99]." It is also clear from Figure 4.6 that the anomaly occurs at ≈ 3 GPa for C_{60} peapods, and we will discuss this anomaly later. In Figure 4.23, the vertical blue dashed line marks the critical pressures of the structural phase transitions of the SWCNTs, and the vertical red dashed line marks the critical pressures of the structural phase transitions of the C_{60} peapods. There is also a second anomaly around 5 GPa in the case of C_{60} peapods, which is marked by the vertical green dashed line. We will discuss the second anomaly in the case of C_{60} peapods later. Table 4.7 shows the effects of the nanotube diameter on the anomaly observed for different samples which are synthesis with versus method (laser ablation and arc discharge).

In the case of the DWCNTs there is no change of the slope in pressure dependence of the energies of the optical transitions up to 8.5 GPa(see Figure 4.22 (b)). In case of DWCNTs, there was no anomaly observed by several Raman studies up to 10 GPa

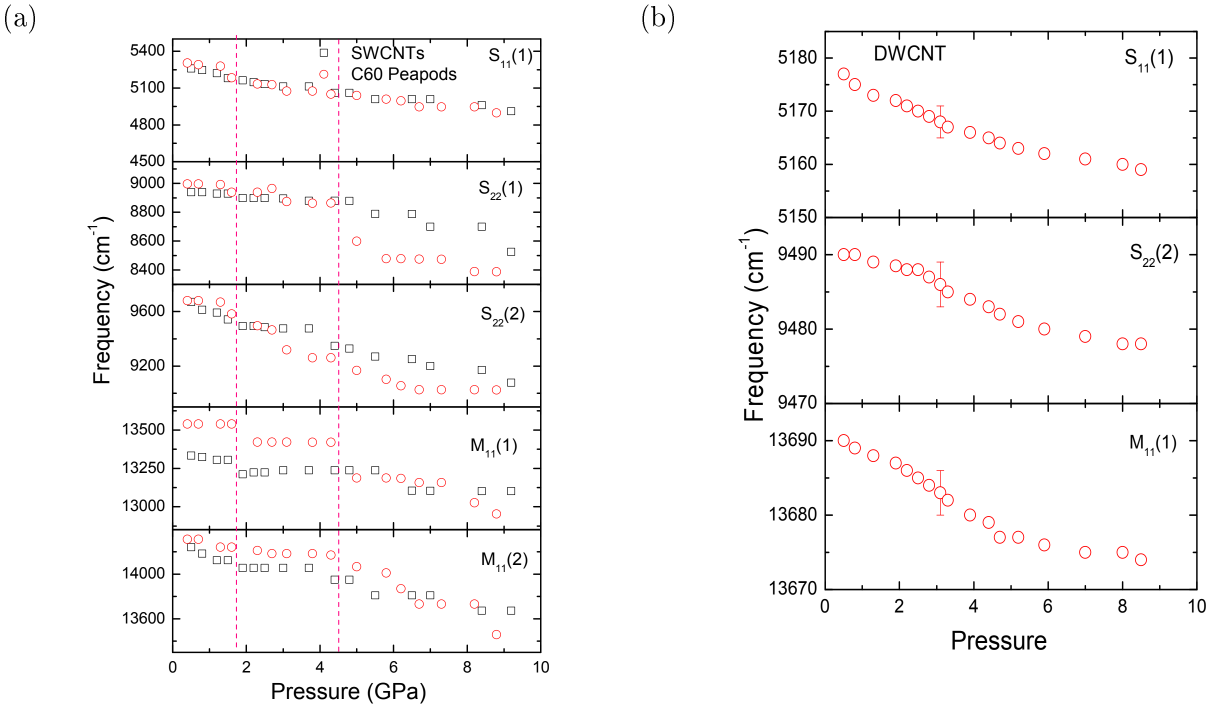

Figure 4.22: *(a) The energies of the optical transitions of SWCNTs film and C_{60} peapods as a function of pressures up to 8.5 GPa for using alcohol mixture as a pressure transmitting medium. (b) The energies of the optical transitions of DWCNTs film as a function of pressure for using alcohol mixture as a pressure transmitting medium. The vertical dashed red lines mark the critical pressures of the structural phase transitions.*

Sample Type	Synthesis	d (nm)	pressure medium	Anomaly
Purified unoriented CNTs	Laser ablation	1.2 nm	alcohol mixture	3 GPa
Oriented SWCNTs embedded in polyethylene matrix	Laser ablation	1.2 nm	alcohol mixture	3 GPa
Purified unoriented SWCNTs	Arc discarge	1.4 nm	alcohol mixture	1.7 GPa
C_{60} peapods	Arc discarge	1.4 nm	alcohol mixture	3 GPa
Purifed unoriented DWCNT	Arc discarge	Outer. d. 1.4 nm Inner. d. 0.7 nm	alcohol mixture	– – – –

Table 4.7: *Anomaly observed for versus nanotube sample for using alcohol mixture as pressure transmitting medium .*

suggesting that the outer tube acts as a protective shield for the inner tube on the bundles of DWCNTs under hydrostatic pressure. At the same time, the inner tube provides structural support to the outer tube [4, 54–56, 100]. Arvanitidis *et al.* [54] investigated the effect of the hydrostatic pressure on the double wall carbon nanotube using alcohol mixture as a pressure transmitting medium. He observed that the intensity of the radial breathing modes and the tangential band of the outer tubes remain detectable up to 10 GPa. On the other hand, the intensity of the radial breathing modes and the tangential band of the internal tubes is less sensitive to the application of pressure up to 10 GPa. Arvanitidis *et al.* [54] concluded that the outer tube shield the inner tubes against pressure, whereas the inner tube support the outer tubes against the increasing pressure.

The application of pressure initially causes the deformation of the primary tubes, which actually shield the inner tubes against pressure. At higher pressure, the increased interaction between outer and inner shells provides structural support against the deformation of the outer tubes [4,54,55]. Gadagkar *et al.* [32] used classical molecular dynamics simulations to study the collapse of single SWCNTs and double-walled DWCNTs carbon nanotube bundles under hydrostatic pressure. The collapse pressure occurs at a certain critical pressure P_c. The value of P_c follows the relation $P_c \propto 1/d_{ref}^3$. in which d_{ref} is the effective radius of the DWCNTs . Gadagkar *et al.* observed, that "the bundles show 30% hysteresis and the hexagonally close packed lattice is completely restored on decompression. They observed that the P_c for DWCNTs is close to the sum of its values for the inner and the outer tubes considered separately as SWCNTs, demonstrating that the inner tube supports the outer tube [32]".

With the application of pressure, the circular cross-section of nanotubes deforms to stabilize at an oval, elliptical, racetrack-like or peanut-shaped cross-section (see Chapter 2). According to theoretical calculation, the anomaly was observed around $\approx$ 20 GPa in the case of the DWCNTs with inner tube diameter 0.6 nm and outer tube diameter 1.4 nm [32]. The approximate anomaly value estimated for the DWCNTs studied within this project is $\approx$ 25 GPa. The pressures at which the anomaly in the pressure dependence of the optical transitions occurs in case of SWCNTs lie in the range of the expected critical transition pressure. In the case of the C_{60} peapods films, the anomaly is observed around 3 GPa. We attribute the anomaly observed to the onset of the structural deformation of the nanotubes from the circular to an ellipse-like shape. Kuntscher demonstrated that "this is in agreement with the interpretation of recent Raman measurements on C_{70} peapods under pressure, pointing out the weak character of the fullerenetube interaction below 2 GPa [57]. However, we cannot rule out that the observed anomaly is related to the pressure effects in partially empty nanotubes [91, 99]". In the case of the DWCNTs film there is no anomaly up to 8.5 GPa (the maximum pressure reached in our measurements) (see Figure 4.22 (b)),

Figure 4.24 shows the relative changes of the energy of the optical transitions of the films with respect to the lowest pressure. It can be seen that the pressure-induced changes in the energy of the optical transitions in the investigated nanotube films are comparable for SWCNTs and C_{60} peapods, but it is very small for all optical transition in the case of the DWCNTs film. It is also clear from Figure 4.24, that the shifts of the optical transitions show a second anomaly at P_c=5 GPa in the case of the SWCNTs film and in the case of C_{60} peapods [91, 99]. In the case of SWCNTs, the second anomaly was attributed to a more drastic change in cross section from an ellipse-like to race-track or peanut-type shape [91]. In our experimental results, the observation of two anomalies has been interpreted by following way. The first anomaly at P_c=1.7 GPa is due to the start of the structural phase transition and the second anomaly at 5 GPa is due to a more drastic deformation of the nanotubes cross section. This is in good agreement with our study of unoriented SWCNTs (see Section 4.1) using the same pressure transmitting medium (alcohol mixture) [91]. We attributed the second anomaly observed at $\approx$ 5 GPa in the case of C_{60} peapods due to the interaction between the fullerene molecules and the carbon nanotubes. Kuntscher demonstrated that "this second anomaly might be due to the onset of the interaction between the carbon nanotubes and the fullerene molecules, as suggested in Ref. [57] [99]". Table 4.8 shows the effects of the nanotube diameter on the second anomaly.

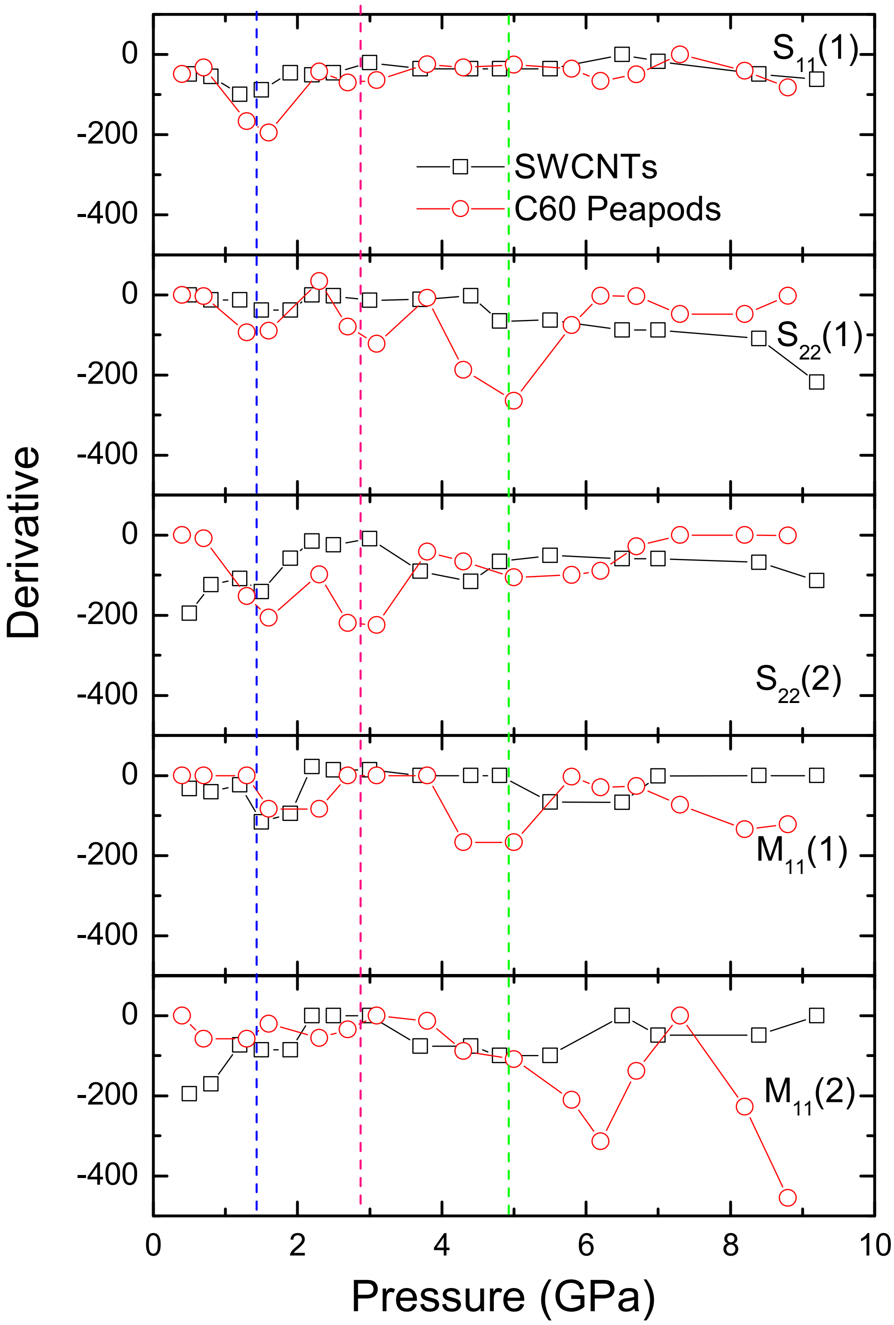

Figure 4.23: *The calculated derivative of the energies of the all optical transitions of the SWCNTs film, the* C_{60} *peapods films as a function of pressure for using alcohol mixture as a pressure transmitting medium. The vertical dashed blue, red and green lines mark the critical pressures of the first and second structural phase transitions.*

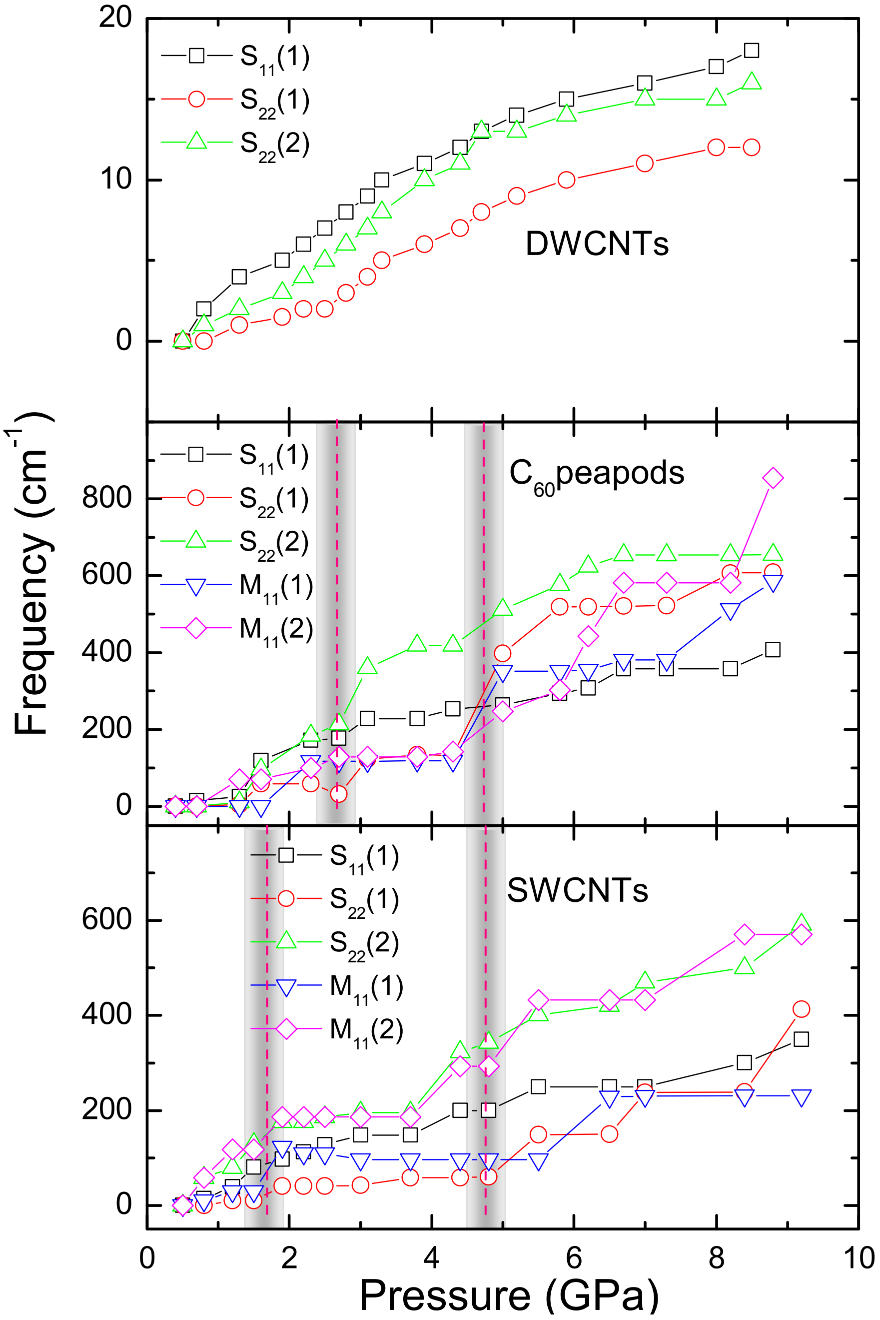

Figure 4.24: *Relative change in the energies of the all optical transitions of the SWCNTs film, the* C_{60} *peapods film and DWCNTs as a function of pressure for using alcohol mixture as a pressure transmitting medium.*

Sample Type	Synthesis	d (nm)	pressure medium	Anomaly
Purified unoriented CNTs	Laser ablation	1.2 nm	alcohol mixture	6 GPa
Oriented SWCNTs embedded in polyethylene matrix	Laser ablation	1.2 nm	alcohol mixture	6 GPa
Purified unoriented SWCNTs	Arc discarge	1.4 nm	alcohol mixture	5 GPa
C_{60} peapods	Arc discarge	1.4 nm	alcohol mixture	5 GPa
Purifed unoriented DWCNT	Arc discarge	Outer. d. 1.4 nm Inner. d. 0.7 nm	alcohol mixture	– – – –

Table 4.8: *The second anomaly observed for versus nanotube sample for using alcohol mixture as pressure transmitting medium.*

4.3.3 Hydrostaticity effect for C_{60} peapods and DWCNTs

We have explored C_{60} peapods and double wall carbon nanotubes using a methanol-ethanol mixture as pressure transmitting medium. In the following, we will compare the infrared spectra under hydrostatic pressure using other pressure media (argon and CsI). Figure 4.25 (i) and (ii) shows the absorbance spectra of C_{60} peapods and DWCNTs respectively as a function of applied pressure in the NIR-Visible frequency range obtained using the methanol-ethanol mixture, argon and CsI as a pressure transmitting medium.

After applying pressure, remarkable changes occur in the optical spectra of C_{60} peapods and DWCNTs. All the peaks lose their intensity and get broader. Qualitatively, all data sets exhibit the same trend: the optical transitions of the C_{60} peapods and DWCNTs films shift to lower energies for using alcohols mixture and CsI. For quantitative analysis, the energy of the optical transitions is extracted from the absorbance spectra for all measured pressures.

Figure 4.26 (i) and (ii) illustrate the fitting curves and their components for C_{60} peapods and DWCNTs using the various pressure transmitting media. In the case of C_{60} peapods, we used two Lorantzian contribution for fitting S_{22} and M_{11} transition for alcohol mixture, but for argon and CsI the absorbance spectrum is much broader and loses the intensity especially in the case of CsI as a pressure transmitting medium, therefore we used one Lorantzian contribution for fitting M_{11} transition (see Figure 4.26 (i)). In the case of DWCNTs, as shown in Figure 4.26 (ii) the fitting contribution is almost the same for using different pressure transmitting media. However the optical transitions are broader in the case of using argon and CsI as a pressure

Sample Type	Synthesis	d (nm)	pressure medium	First anomaly	second anomaly
Purified unoriented SWCNTs	Laser ablation	1.2 nm	alcohol mixture argon CsI	3 GPa 2 1.7	6 GPa 5 5
Purified Oriented SWCNTs	Laser ablation	1.2 nm	alcohol mixture argon CsI	3 GPa 2 GPa 2 GPa	6 GPa 5 GPa 5 GPa
Purified unoriented SWCNTs	Arc discharge	1.4 nm	alcohol mixture	1.7 GPa	5 GPa
C_{60} peapods	Arc discharge	1.4 nm	alcohol mixture argon CsI	3 GPa 2 1.5	5 GPa – –
Purifed unoriented DWCNTs	Arc discharge	Outer. d. 1.4 nm Inner. d. 0.7 nm	alcohol mixture argon CsI	– – –	– – –

Table 4.9: *The anomalies observed for versus nanotube sample for using different pressure transmitting media.*

transmitting media, because of less hydrostaticicty of CsI and argon comparing to alcohol mixture.

For further differences in the pressure dependence of the optical transitions, the relative changes in energies of the strong transitions in the C_{60} peapods and DWCNTs films film were plotted as a function of pressure. Figure 4.28 (i) and (ii) shows the changes of the energy of the optical transitions of the films as a function of pressure for C_{60} peapods and DWCNTs, respectively. Figure 4.27 (i) and (ii) shows the relative changes of the energy of the optical transitions of the films with respect to the lowest pressure for C_{60} peapods and DWCNTs, respectively.

It can be seen that the pressure-induced changes in the energy of the optical transitions in the C_{60} peapods are comparable for all pressure transmitting media. The maximum shift of the optical transitions with the application of pressures up to 8 GPa is around 1000 cm^{-1} ($\approx$ 0.12 eV). The pressure dependency of the optical transitions of both semiconducting and metallic tubes is very similar with comparable slopes (see Figure 4.27).

In general, the red-shift of the optical transitions is in qualitative agreement with the

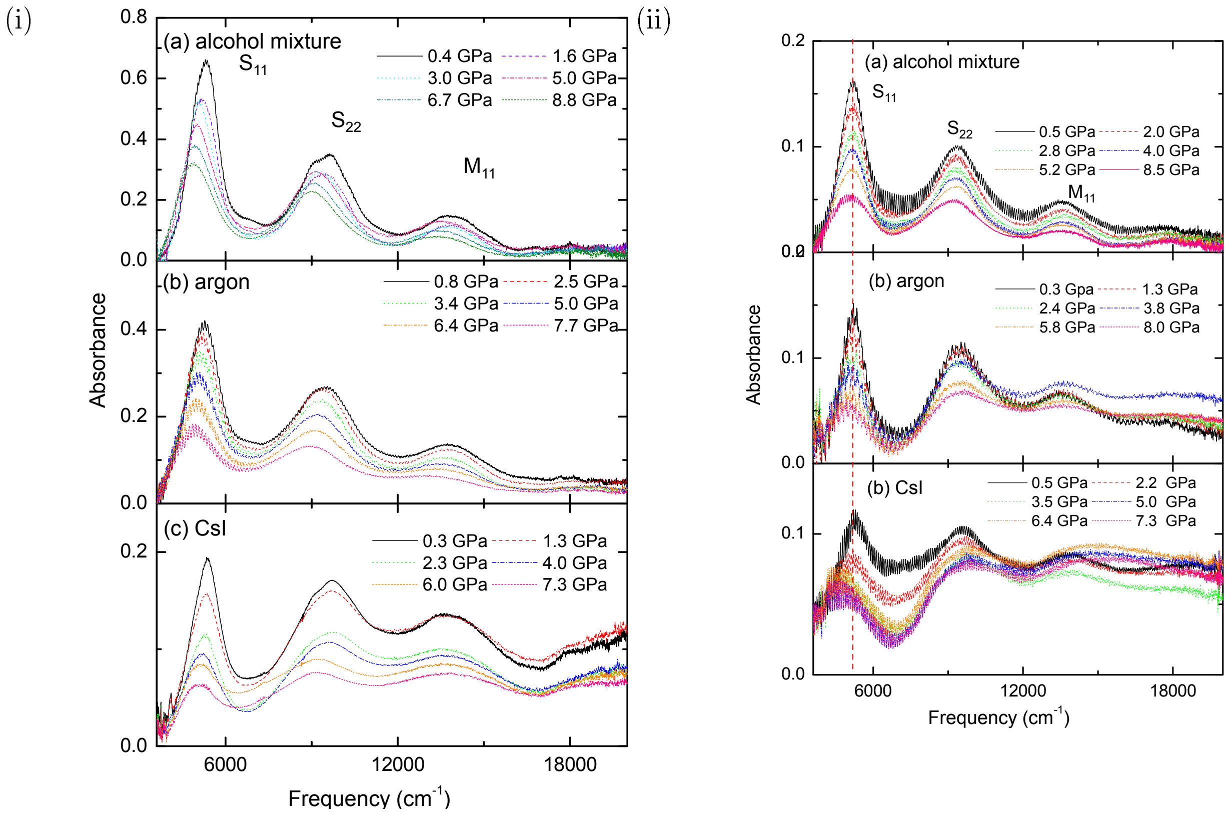

Figure 4.25: *(i) Background-subtracted absorbance spectra of* C_{60} *peapods films as a function of pressure for various pressure transmitting media: (a) alcohol mixture, (b) argon, (c) CsI. (ii) Background-subtracted absorbance spectra of DWCNTs films as a function of pressure for various pressure transmitting media: (a) alcohol mixture, (b) argon and (c) CsI.*

previous pressure-dependent studies on unoriented and oriented SWCNTs [3,51,101]. In the case of DWCNTs, the energy-shift of the optical transition under pressure is much smaller than for unoriented and oriented SWCNTs and C_{60} peapods [51]. However, the shift of the energy of optical transitions in the measurements with argon and CsI at 8 GPa is nearly 2 times as much as that observed in the measurements with alcohol mixture as a pressure transmitting medium. This discrepancy is probably due to the less hydrostatic conditions. Using more hydrostatic pressure medium (alcohol mixture) could minimize strains due to non-hydrostaticity, reducing the extent of the red-shift and the broadening of the transitions.

The effect of pressure transmitting medium on the amount of red-shift is observed in the case of DWCNTs. It is clear from Figure 4.27 (ii) that the maximum shift of the optical transitions $S_{11}(1)$, $S_{22}(1)$ and $M_{11}(2)$ with the application of pressures up to

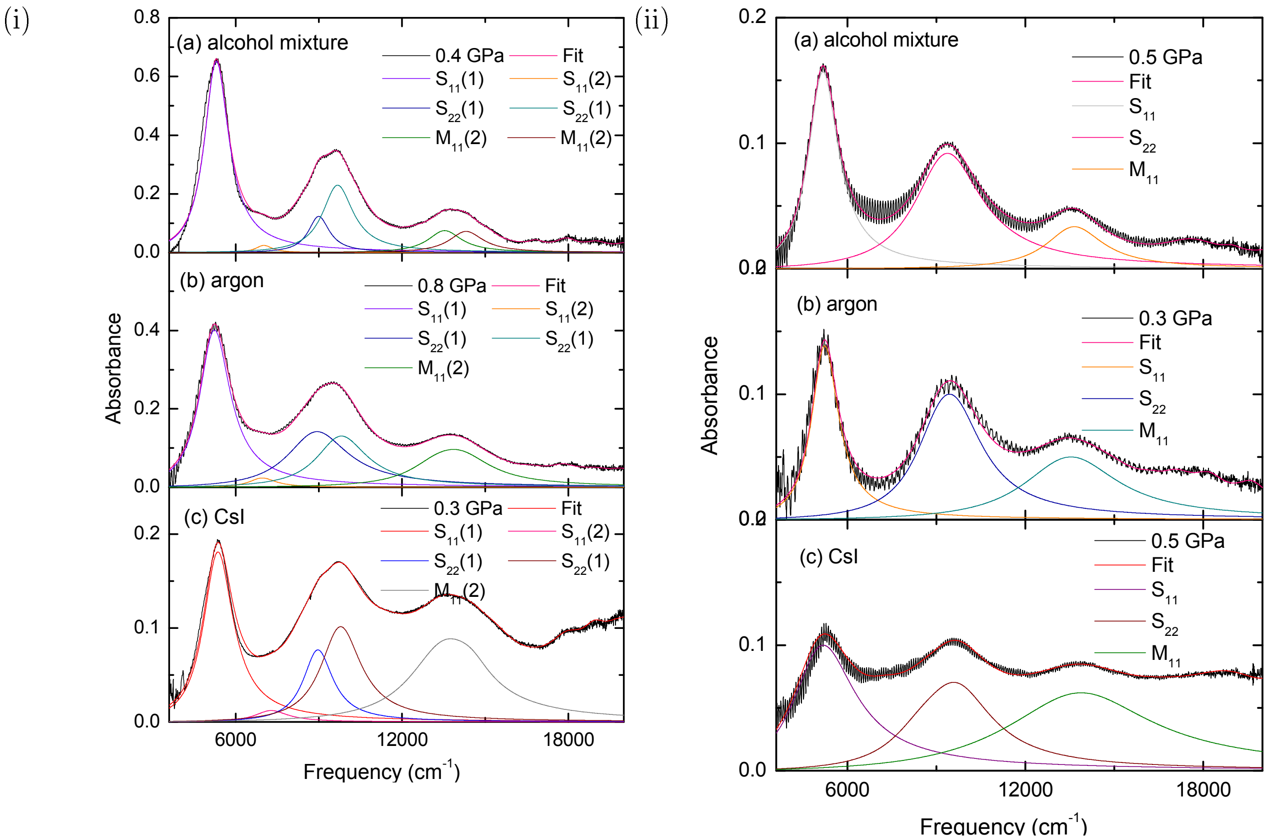

Figure 4.26: *Absorbance spectrum of the (i) C_{60} peapods and (ii) DWCNTs films at low pressure and the fit with Lorentz functions, for various pressure transmitting media: (a) alcohol mixture; (b) argon; (c) CsI.*

8.5 GPa is around 450 cm^{-1}, 250 cm^{-1} and 100 cm^{-1} respectively in the case of using CsI as a pressure transmitting medium. However, the amount of red-shift is smaller in the case of using argon and alcohol mixture as a pressure transmitting media. In the case of argon, the amount of red-shift is around 100 cm^{-1} for both $S_{22}(1)$ and $M_{11}(2)$ optical transitions and around 200 cm^{-1} for $S_{11}(1)$ optical transition. In the case of alcohol mixture as a pressure transmitting medium, the the amount of red-shift is around 20 cm^{-1} for all optical transitions $S_{11}(1)$, $S_{22}(1)$ and $M_{11}(2)$. The main reason is that an uniaxial stress component is absent in the alcohol mixture up to solidification pressure i.e., the solidification pressure of the alcohol mixture is around 10.4 GPa. On the other hand, an uniaxial stress component is present in the argon since it solidifies around 1.3 GPa and CsI is already solid at ambient condition. The main point is that the red-shift for all pressure transmitting media is very pronounced for SWCNTs. Thus, SWCNTs is sensitive to uniaxial stress.

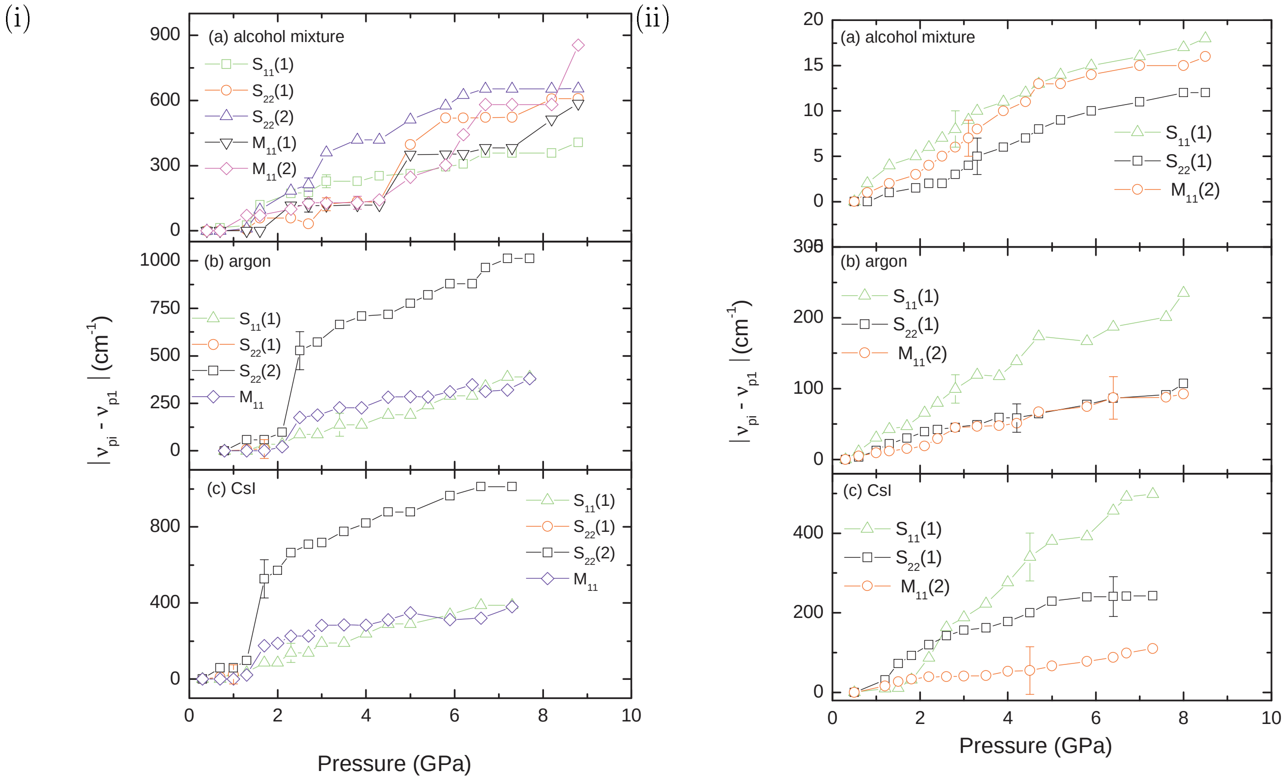

Figure 4.27: *Pressure-induced energy shifts of the optical transitions for (i) C_{60} peapods and (ii) DWCNTs with respect to the lowest pressure for (a) alcohol mixture, (b) argon and (c) CsI as pressure transmitting media.*

From the derivative of the optical spectra as shown in Figure 4.29, the anomalies are obvious clearly. It is clear from this figure that the derivative of the obtained energy of optical transitions as a function of pressure exhibit anomalies at $P_c\approx$1.5 GPa for CsI, $P_c\approx$2 GPa argon and $P_c\approx$ 3 GPa in case alcohol mixture as pressure transmitting media. In Figure 4.29, the vertical blue, red and green dashed line mark the first anomaly of the structural phase transitions for using CsI, argon and alcohol mixture as a pressure transmitting media. The critical pressure P_c of the structural deformation depends on the degree of hydrostaticity for using various pressure transmitting media. This is consistent with earlier results on unoriented SWCNTs [51] (see Section 4.1 and 4.2). In the case of using alcohol mixture, there is a second anomaly at around 5 GPa, which is marked by the vertical black dashed line. We discussed the origin of this anomaly around 5 GPa in the pervious subsection. Kuntscher demonstrated that "for the other pressure transmitting media (argon, CsI) the second anomaly is blurred by the broadening of the absorption bands". Finally, we concluded all the anomalies, which we observed for different samples for using different pressure transmitting media

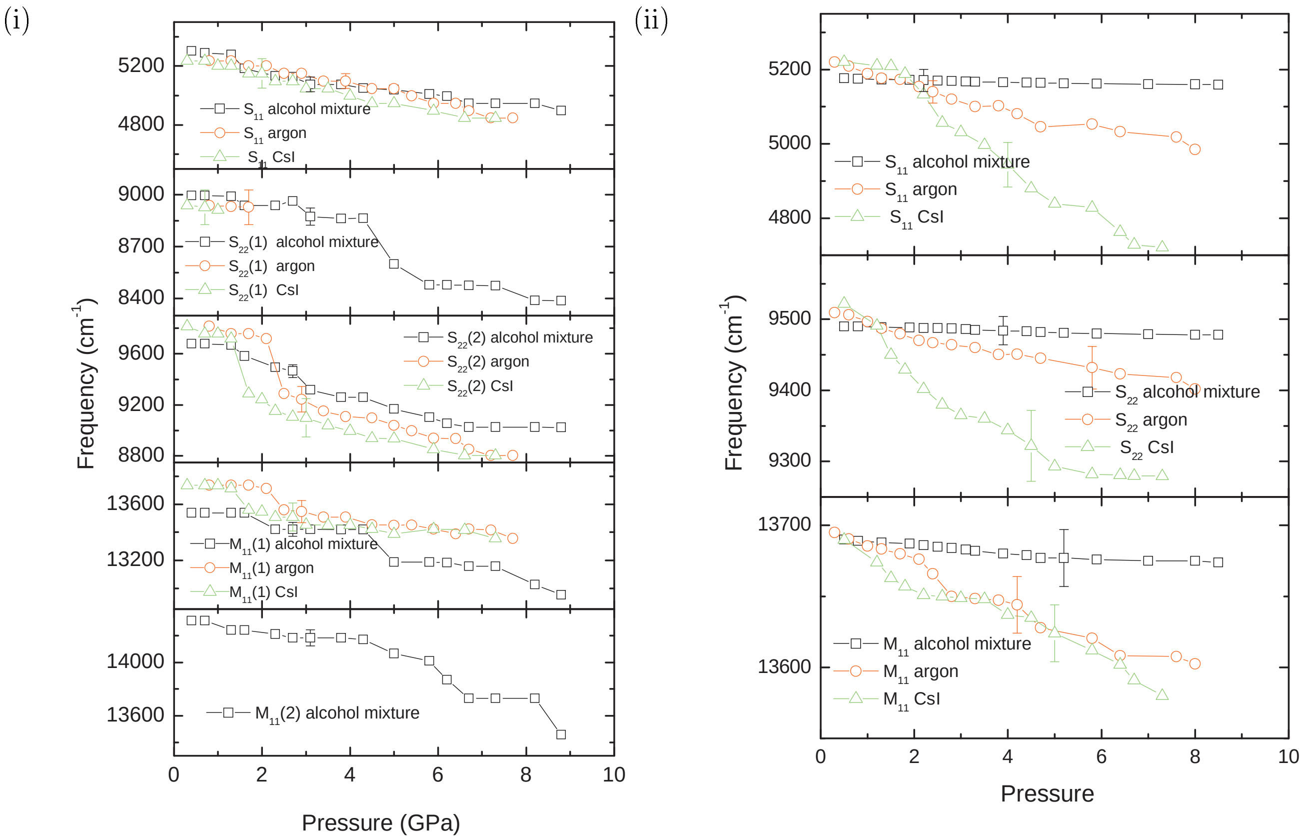

Figure 4.28: *Pressure dependence of the optical transition energies for (i) C_{60} peapods and (ii) DWCNTs obtained from the absorbance spectra, for using alcohol mixture, argon and CsI as pressure transmitting media.*

in Table 4.9.

4.4 Summary

The pressure dependence of the optical transitions have been investigated on SWCNTs (unoriented and oriented), C_{60} Peapods and DWCNTs films in the NIR-Visible frequency range for using different pressure transmitting medium for pressures up to 9 GPa. The spectra of all investigated SWCNT, C_{60} peapods and DWCNTs films contain the optical absorption bands corresponding to both metallic and semiconducting tubes. In the oriented nanotube films, a strong anisotropy is observed in the optical conductivity with respect to the alignment direction. In all films (unoriented and oriented SWCNTs, C_{60} Peapods and DWCNTs) the optical transitions shift to lower energies with increasing pressure. The amount of this red-shift is comparable in SWCNTs (unoriented and oriented) and C_{60} peapods films for using different pressure transmitting medium. This is in a good agreement with earlier results [51, 91, 99]. For DWCNTs films, the red-shift is much smaller for using alcohol mixture as a pressure medium, and increases in case of argon and CsI. In the case of DWCNTs, the energy-shift of the optical transition under pressure is much smaller than for unoriented and oriented SWCNTs and C_{60} peapods [51]. This is because DWCNTs are more stable than SWCNTs as suggested in Ref [4, 54–56, 100]. This red-shift of the optical transitions are most likely due to the significant $\sigma^*\pi^*$ hybridization effects arising from the pressure-induced deformation of the nanotubes.

The pressure dependence of the optical transitions exhibits an anomaly at about 2-3 GPa, and second anomaly around 6 GPa for SWCNTs (unoriented nanotube films and the nanotubes-polymer matric) for using different pressure media. In the case C_{60} peapods, the first anomaly is observed around 3 GPa and second anomaly is observed around 5 GPa for using alcohol mixture as a pressure transmitting medium, while the first anomaly is observed around 1.5 GPa and 2 GPa in the case of using CsI and argon respectively. The second anomaly is not observed in the case of using argon and CsI as a pressure transmitting media, because the absorbtion bands are broadened with increasing pressure. There is no clear observed anomaly in the case of DWCNTs film.

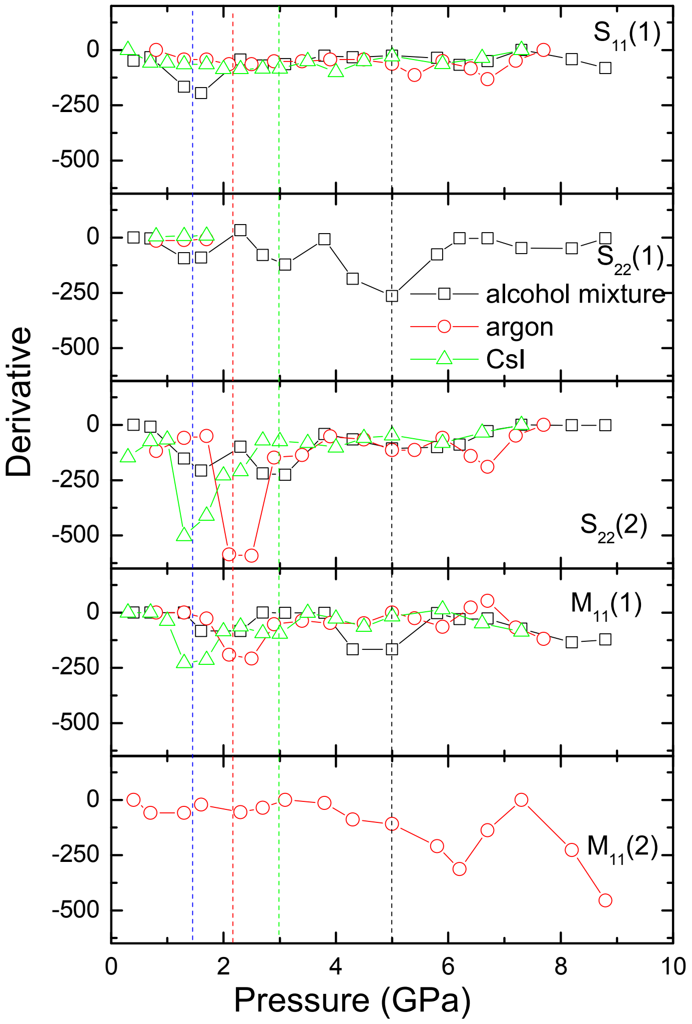

Figure 4.29: *The calculated derivative of the energies of the all optical transitions of the C_{60} peapods film as a function of pressure for using alcohol mixture, argon and CsI as a pressure transmitting media. The vertical dashed blue, red, green and black lines mark the critical pressures of the first and second structural phase transitions.*

5 Conclusions and outlook

The pressure-dependent infrared spectroscopic measurements were performed on the unoriented SWCNTs, oriented SWCNTs, peapods (C_{60} encapsulated SWCNTs) and double-walled carbon nanotube (DWCNTs) over a broad frequency range for pressures up to 8 GPa for using different pressure transmitting media. In the case of unoriented SWCNTs and oriented SWCNTs, both films show qualitatively similar results for using different pressure transmitting media. However, there are quantitative differences in the amount of the energy shifts, where the absorption bands due to transitions between van Hove singularities exhibit a red-shift with increasing pressure. This red-shift of the optical transitions is most likely due to the significant $\sigma^* - \pi^*$ hybridization effects arising from the pressure-induced deformation of the nanotubes. The red-shift of the optical transitions is comparable for using different pressure transmitting media. Furthermore, the pressure dependence of the optical transition energies exhibit an anomaly at a critical pressure of P_c= 2-3 GPa. The results for the unoriented SWCNTs films are very similar to those for oriented SWCNTs films under pressure. This results proves that the alignment of the SWCNTs does not improve the mechanical stability of the oreinted SWCNTS under pressure.

In consistent with the theoretical predictions, the anomaly can be attributed to a structural phase transition in the SWCNTs, where the circular cross section is deformed to an oval shape. This result questions the proposed importance of the pressure medium regarding the occurrence of the pressure induced structural phase transition. For more hydrostatic pressure transmitting media (helium, alcohol mixture), the critical pressure is slightly higher, $P_c \approx$ 3 GPa, compared to the less hydrostatic ones (argon, CsI), where $P_c \approx$ 2 GPa. According to our results, metallic and semiconducting nanotubes respond to pressure in a very similar way. The spectral weights of the absorption bands decrease with increasing pressure, which suggests that the dimensionality of the system is affected by applied pressure.

In addition, the pressure-induced shifts of the optical transitions in SWCNTs exhibit a second anomaly, present for all utilized pressure transmitting media. We interpret the second anomaly at pressures 5-6 GPa in terms of a more drastic change in the nanotubes cross section from an ellipse-like to race-track or peanut-type shape, in agreement with recent reports on pressure-dependent Raman scattering.

We also performed polarization-dependent transmission measurements on films of oriented SWCNTs as a function of pressure, where the polarization-dependent infrared spectroscopic measurements on the oriented nanotubes in polyethylene matrix, have been performed in the NIR-visible frequency range. A strong anisotropy is observed in the optical conductivity of oriented SWCNTs film. The pressure dependence of the optical transitions exhibit an anomaly at around 2 GPa for the nanotubes-polymer matrix in case of using argon and CsI as a pressure transmitting media, and around 3 GPa for using alcohol mixture in agreement with the unoriented SWCNTs. The second anomaly is also observed around 6 GPa. The strong anisotropy is observed in the optical transition of oriented SWCNTs film with strong absorption bands for the electric field along the alignment direction up to the highest pressure 8 GPa.

In addition, infrared spectroscopic measurements on peapods (C_{60} encapsulated SWCNTs) and double-walled carbon nanotube (DWCNTs) under pressure have been performed. The SWCNTs are more sensitive to the application of pressure than the DWCNTS due to more effective space filling of the inner tube. In order to understand the electronic properties of C_{60} peapods and DWCNTS, the pressure-dependent infrared spectroscopic measurements on the C_{60} peapods and DWCNTs films were performed in the NIR-visible frequency range for pressures up to 8.5 GPa for using three different pressure transmitting media. The amount of red-shift of the optical transitions are comparable in SWCNTs (unoriented and oriented) and C_{60} peapods films for using different pressure transmitting media. In the case of DWCNTs films, the amount of red-shift is much smaller for using alcohol mixture as a pressure medium, and 5 times increase for using argon and CsI as a pressure transmitting media. The main reason is, perhaps, a uniaxial stress component which is absent in alcohol up to solidification pressure around 10.4 GPa. On the other hand, a uniaxial stress is present in argon since it is solidification around 1.3 GPa, and CsI is already solid at ambient condition. The pressure dependence of the optical transitions exhibit an anomaly at around 2 GPa for C_{60} peapods film for using argon and CsI as a pressure transmitting media, and at around 3 GPa for using alcohol mixture as a pressure transmitting medium. There is no clear observed anomaly in the case of DWCNTs film for using different pressure media for pressure up to 8.0 GPa.

Bibliography

[1] S. Iijima, Nature **354**, 56 (1991).

[2] K. Thirunavukkuarasu, *Carbon Nanostructurees Under High Pressure Studied By Infrared Spectroscopy* (University of Augsburg, Augsburg, 2009).

[3] K. Thirunavukkuarasu, F. Hennrich, K. Kamaras, and C. A. Kuntscher, Phys. Rev. B **81**, 045424 (2010).

[4] P. Puech, H. Hubel, D. J. Dunstan, A. Bassil, R. Bacsa, A. Peigney, and E. Flahaut, Phys. Status Solidi B **241**, 3360 (2004).

[5] S. Reich, C. Thomsen, and J. Maultzsch, *Carbon nanotubes: Basic concepts and physical properties* (Wiley-VCH, Weinheim, 2004).

[6] R. Saito, G. Dresselhaus, and M. S. Dresselhaus, *Physical Properties of Carbon Nanotubes* (Imperial College Press, London, 1998).

[7] P. R. Wallace, Phys. Rev. **71**, 622 (1947).

[8] S. Reich, J. Maultzsch, C. Thomsen, and P. Ordejon$'$, Phys. Rev. B **66**, 035412 (2002).

[9] C. Thomsen and S. Reich, Raman Scattering in Carbon Nanotubes Light Scattering in Solid IX, Appl. Physics **108**, 115 (2007).

[10] J. W. Mintmire, B. I. Dunlap, and C. T. White, Phys. Rev. Lett. **68**, 631 (1992).

[11] N. Hamada, S. Sawada, and A. Oshiyama, Phys. Rev. Lett. **68**, 1579 (1992).

[12] R. Saito, M. Fujita, G. Dresselhaus, and M. S. Dresselhaus, Phys. Rev. B **46**, 1804 (1992).

[13] S. Reich and C. Thomsen, Phys. Rev. B **62**, 4273 (2000).

[14] R. Saito, M. Fujita, G. Dresselhaus, and M. S. Dresselhaus, Phys. Rev. B **46**, 1804 (1992).

[15] R. Saito, G. Dresselhaus, and M. S. Dresselhaus, Phys. Rev. B **61**, 2981 (2000).

[16] R. Saito, G. Dresselhaus, and M. S. Dresselhaus, J. Appl. Phys. **73**, 494 (1993).

[17] W. Song, M. Ni, J. Lu, Z. Gao, S. Nagase, D. Yu, H. Ye, and X. Zhang, Chemical Physics Letters **414**, 429 (2005).

[18] J. Chen, X. Wang, S. Leng, and Z. Yang, Physics Letters A **351**, 105 (2006).

[19] G. W. Ho, Y. H. Ho, T. S. Li, C. P. Chang, and M. F. Lin, Carbon **44**, 2323 (2006).

[20] J. W. Mintmire and C. T. White, Phys. Rev. Lett. **81**, 2506 (1998).

[21] M. Ouyang, J. L. Huang, C. L. Cheung, and C. M. Lieber, Science **292**, 702 (2001).

[22] A. M. Rao, J. Chen, E. Richter, U. Schlecht, P. C. Eklund, R. C. Haddon, U. D. Venkateswaran, Y. K. Kwon, and D. Tománek, Phys. Rev. Lett. **86**, 3895 (2001).

[23] S. Reich, C. Thomsen, and P. Ordejo′n, Phys. Rev. B **65**, 155411 (2002).

[24] M. J. O'Connell, S. Sivaram, and S. K. Doorn, Phys. Rev. B **69**, 235415 (2004).

[25] I. Bozovic, N. Bozovic, and M. Damnjanovic, Phys. Rev. B **62**, 6971 (2000).

[26] N. Wang, Z. K. Tang, G. D. Li, and J. S. Chen, Nature **408**, 50 (2000).

[27] H. Kataura, Y. Kumazawa, Y. Maniwa, I. Umezu, S. Suzuki, Y. Ohtsuka, and Y. Achiba, Synthetic Metals **103**, 2555 (1999).

[28] G. G. Samsonidze, R. Saito, A. Jorio, M. A. Pimenta, A. G. S. Filho, A. Grüneis, G. Dresselhaus, and M. S. Dresselhausa, Journal of Nanoscience and Nanotechnology **3**, 431 (2003).

[29] R. Saito, K. Sato, Y. Oyama, J. Jiang, G. G. Samsonidze, G. Dresselhaus, and M. S. Dresselhaus, Phys. Rev. B **72**, 153413 (2005).

[30] S. Lebedkin, K. Arnold, O. Kiowski, F. Hennrich, and M. M. Kappes, Phys. Rev. B **73**, 094109 (2006).

[31] J. A. Elliott, J. K. W. Sandler, A. H. Windle, R. J. Young, and M. S. P. Shaffer, Phys. Rev. Lett. **92**, 095501 (2004).

[32] V. Gadagkar, P. K. Maiti, Y. Lansac, A. Jagota, and A. K. Sood, Phys. Rev. B **73**, 085402 (2006).

[33] P. M. Rafailov, C. Thomsen, and H. Kataura, Phys. Rev. B **68**, 193411 (2003).

[34] S. M. Sharma, S. Karmakar, S. K. Sikka, P. V. Teredesai, A. K. Sood, A. Govindaraj, and C. N. R. Rao, Phys. Rev. B **63**, 205417 (2001).

[35] M. Hasegawa and K. Nishidate, Phys. Rev. B **74**, 115401 (2006).

[36] S. Reich, C. Thomsen, and P. Ordejon, Phys. Rev. B **65**, 153407 (2002).

[37] S. P. Chan, W. L. Yim, X. G. Gong, and Z. F. Liu, Phys. Rev. B **68**, 075404 (2003).

[38] M. H. F. Sluiter and Y. Kawazoe, Phys. Rev. B **69**, 224111 (2004).

[39] C. Li and T. W. Chou, Phys. Rev. B **69**, 073401 (2004).

[40] X. H. Zhang, D. Y. Sun, Z. F. Liu, and X. G. Gong, Phys. Rev. B **70**, 035422 (2004).

[41] R. B. Capaz, C. D. Spataru, P. Tangney, M. L. Cohen, and S. G. Louie, phys. stat. sol.(b) **241**, 3352 (2004).

[42] O. Gülseren, T. Yildirim, S. Ciraci, and C. KiliC, Phys. Rev. B **65**, 155410 (2002).

[43] S. Okada, A. Oshiyama, and S. Saito, J. Phys. Soc. Jpn **70**, 2345 (2001).

[44] I. Loa, J. Raman. Spectrosc **34**, 611 (2003).

[45] J. Tang, L.-C. Qin, T. Sasaki, M. Yudasaka, A. Matsushita, and S. Iijima, Phys. Rev. Lett. **85**, 1887 (2000).

[46] S. Kazaoui, N. Minami, H. Yamawaki, K. Aoki, H. Kataura, and Y. Achiba, Phys. Rev. B **62**, 1643 (2000).

[47] U. D. Venkateswaran, A. M. Rao, E. Richter, M. Menon, A. Rinzler, R. E. Smalley, and P. C. Eklund, Phys. Rev. B **59**, 10928 (1999).

[48] M. J. Peters, L. E. McNeil, J. P. Lu, and D. Kahn, Phys. Rev. B **61**, 5939 (2000).

[49] P. V. Teredesai, A. K. Sood, D. V. S. Muthu, R. Sen, A. Govindaraj, and C. N. R. Rao, Chem. Phys. Lett. **319**, 296 (2000).

[50] U. D. Venkateswaran, E. A. Brandsen, U. Schlecht, A. M. Rao, E. Richter, I. Loa, K. Syassen, and P. C. Eklund, Phys. Status Solidi B **223**, 225 (2001).

[51] A. Abouelsayed, K. Thirunavukkuarasu, F. Hennrich, , and C. A. Kuntscher, J. Phys. Chem. C **144**, 4424 (2010).

[52] M. S. Amer, M. M. El-Ashry, and J. F. Maguire, J. Chem. Phys. **121**, 2752 (2004).

[53] A. Merlen, N. Bendiab, P. Toulemonde, A. Aouizerat, A. S. Miguel, J. Sauvajol, G. Montagnac, H. Cardon, and P. Petit, Phys. Rev. B **72**, 035409 (2005).

[54] J. Arvanitidis, D. Christofilos, K. Papagelis, K. S. Andrikopoulos, T. Takenobu, Y. Iwasa, H. Kataura, S. Ves, and G. A. Kourouklis, Phys. Rev. B **71**, 125404 (2005).

[55] P. Puech, H. Hubel, D. J. Dunstan, R. R. Bacsa, C. Laurent, and W. S. Bacsa, Phys. Rev. Lett. **93**, 095506 (2004).

[56] U. D. Venkateswaran, phys. stat. sol. (b) **241**, 3345 (2004).

[57] C. Caillier, D. Machon, A. San-Miguel, R. Arenal, C. Montagnac, H. Cardon, M. Kalbac, M. Zukalova, and L. Kavan, Phys. Rev. B **77**, 125418 (2008).

[58] G. Huber, K. Syassen, and W. B. Holzapfel, Phys. Rev. B **15**, 5123 (1977).

[59] M. Fox, *Optical properties of Solids* (Oxford University press, New York, USA, 2001).

[60] M. Dressel and G. Grüner, *Electrodynamics of Solids* (Cambridge University press, UK, 2002).

[61] F. Wooten, *Optical properties of Solids* (Academic press, USA, 1972).

[62] D. J. Dunstan, Rev. Sci. Instrum. **60**, 3789 (1989).

[63] D. J. Dunstan and I. L. Spain, J. Phys. E **22**, 913 (1989).

[64] M. I. Eremets, *High pressure experiemental methods* (Oxford university press, New York, 1996).

[65] A. Jayaraman, Rev. Sci. Instrum. **57**, 1013 (1986).

[66] C. Ulrich, E. Anastassakis, K. Syassen, A. Debernardi, and M. Cardona, Phys. Rev. Lett. **78**, 1283 (1997).

[67] G. J. Piermarini, S. Block, J. D. Barnett, and R. A. Forman, J. Appl. Phys. **46**, 2774 (1975).

[68] H. K. Mao, J. Xu, and P. M. Bell, J. Geophys. Res. **91**, 4673 (1986).

[69] D. E. McCumber and M. D. Sturge, J. Appl. Phys. **34**, 1682 (1963).

[70] J. D. Barnett, S. Block, and G. J. Piermarini, Rev. Sci. Instrum. **44**, 1 (1972).

[71] L. Oriel, *MS260i imaging spectrograph information manual.*

[72] D. Young, A. K. McMahan, and M. Ross, Phys. Rev. B **24**, 5119 (1981).

[73] M. Ross, physical Review **171**, 777 (1968).

[74] S. Klotz, J.-C. Chervin, P. Munsch, and G. L. Marchand, J. Phys. D: Appl. Phys. **42**, 075413 (2009).

[75] G. J. Piermarini, S. Block, and J. D. Barnett, J. Appl. Phys. **44**, 5377 (1973).

[76] J. M. Besson and J. P. Pinceaux, Science **206**, 1073 (1979).

[77] E. D. Palik, *Handbook of optical constants of solids* (Academic press, USA, 1998).

[78] M. I. Eremets and Y. A. Timofeev, Rev. Sci. Instrum. **63**, 3123 (1992).

[79] *Á*. Botos, A. N. Khlobystov, B. Botka, R. Hackl, E. Sz*é*kely, B. Sim*á*ndi, and K. Kamar*á*s, physica status solidi B **247**, 2743 (2010).

[80] B. Botka, *Á*. Pekker, *Á*. Botos, K. Kamar*á*s, and R. Hackl, physica status solidi B **247**, 2843 (2010).

[81] F. Hennrich, S. Lebedkin, S. Malik, J. Tracey, M. Barczewski, H. Roesner, and M. Kappes, Phys. Chem. Chem. Phys. **4**, 2273 (2002).

[82] F. Hennrich, R. Wellmann, S. Malik, S. Lebedkin, and M. Kappes, Phys. Chem. Chem. Phys. **5**, 178 (2003).

[83] N. Akima, Y. Iwasa, S. Brown, A. M. Barbour, J. Cao, J. L. Musfeldt, H. Matsui, N. Toyota, M. Shiraishi, H. Shimoda, and O. Zhou, Adv. Mater. **18**, 1166 (2006).

[84] C. Journet and P. Bernier, Appl. Phys. A **67**, 1 (1998).

[85] C. Journet, W. K. Maser, P. Bernier, A. Loiseau, M. L. de la Chapelle, S. Lefrant, P. Deniard, R. Lee, , and J. E. Fischer, Nature. **388**, 756 (1997).

[86] M. E. Itkis, D. E. Perea, S. Niyogi, S. M. Richard, M. A. Hamon, H. Hu, B. Zhao, and R. C. Haddon, Nano Letters **3**, 309 (2003).

[87] O. Jost, A. A. Gorbunov, W. Pompe, T. Pichler, R. Friedlein, M. Knupfer, M. Reibold, H. D. Bauer, L. Dunsch, M. S. Golden, and J. Fink, Appl. Phys. Lett. **75**, 2217 (1999).

[88] J. C. Charlier, P. Lambin, and T. W. Ebbesen, Phys. Rev. B **54**, R8377 (1996).

[89] G. Liu, X. Wang, J. Chen, and H. Lu, phys. stat. sol. (b) **245**, 689 (2008).

[90] J. Wu, W. Walukiewicz, W. Shan, E. Bourret-Courchesne, J. W. A. III, K. M. Yu, E. E. Haller, K. Kissell, S. M. Bachilo, R. B. Weisman, and R. E. Smalley, Phys. Rev. Lett. **93**, 017404 (2004).

[91] C. A. Kuntscher, A. Abouelsayed, K. Thirunavukkuarasu, and F. Hennrich, Phys. Status Solidi B **247**, 2789 (2010).

[92] M. Yao, Z. Wang, B. Liu, Y. Zou, S. Yu, Y. Hou, S. Pan, M. Jin, B. Zou, T. Cui, G. Zou, and B. Sundqvist, Phys. Rev. B **78**, 205411 (2008).

[93] T. Pichler, M. Knupfer, M. S. Golden, J. Fink, A. Rinzler, and R. E. Smalley, Phys. Rev. Lett. **80**, 4729 (1998).

[94] S. Okada, S. Saito, and A. Oshiyama, Phys. Rev. Lett. **86**, 3835 (2001).

[95] S. Okada, M. Otani, and A. Oshiyama, Phys. Rev. B **67**, 205411 (2003).

[96] S. Okada and A. Oshiyama, Phys. Rev. Lett. **91**, 216801 (2003).

[97] A. Ryabenko, N. Kiselev, J. Hutchison, T. Moroz, S. Bukalov, L. Mikhalitsyn, R. Loutfy, and A. Moravsky, Carbon **45**, 1492 (2007).

[98] X. Liu, T. Pichler, M. Knupfer, M. S. Golden, J. Fink, H. Kataura, Y. Achiba, K. Hirahara, and S. Iijima, Phys. Rev. B **65**, 045419 (2002).

[99] C. A. Kuntscher, A. Abouelsayed, A. Botos, A. Pekker, and K. Kamar$a$΄s, physica status solidi (b) **248**, 2732 (2011).

[100] R. Pfeiffer, H. Kuzmany, C. Kramberger, C. Schaman, T. Pichler, H. Kataura, Y. Achiba, J. Kürti, and V. Zolyomi, Phys. Rev. Lett. **90**, 225501 (2005).

[101] A. Abouelsayed, K. Thirunavukkuarasu, F. Hennrich, , and C. A. Kuntscher, High Pressure Research **29**, 559 (2009).

Acknowledgements

I would like to express my gratitude to Prof. Dr. Christine Kuntscher for introducing me into the vast and interesting field of low-dimensional systems, and for offering constant guidance and dedicated attention in my work.

My immense thanks to our collaborator Dr. Katalin Kamarás not only for giving us the samples of C_{60} peapods and DWCNT films studied for this work, but also undoubtedly for her rewarding discussions. I thank our other collaborators Dr. F. Hennrich, Prof. Y. Iwasa for providing the SWCNT films studied within this PhD project. Of course, the research projects can not progress easily without the help from the technical assistants in the institute. Therefore, I convey my thanks to Mrs Beate Spörhase at Experimental Physik II, Universität Augsburg. A special thanks to Dr. Matthias Klemm for his assistance during scanning electron microscopic measurements on carbon nanotubes films. My thanks to all members of AG Kuntscher for creating a wonderful work environment. It is an extreme pleasure to thank my dear friends Dr. Alexej Pashkin, Dr. Komalavalli Thirunavukkuarasu, Kaneez Rabia, Ali Abdul Qader Al Hadithy, Jihaan Ebad Allah, Estaline Amitha Francis, Abid Karim and Armin Huber for standing firmly by my side with their constant encouragement and moral support. I can not forget their fruitful discussions and comments related to my work. Gratefully thanks to the Egyptian government for financial support for my scholarship. Gratefully thanks also to the Egyptian embassy and our culture office. Last but not the least, I thank my parents, wife, brother and sister for being my invisible strength and motivation no matter what happens, without which it would have been impossible for me to pursue my work.

Curriculum Vitae

Personal information

Date of birth : 26 May 1977
Nationality : Egyptian
Gender : Male
Martial status : Married

Education

Sep 1983 - May 1997	All Egyptian Primary School, All Egyptian Secondary School.
Sep 1997 - May 2001	Bachelor's degree in Physics, Faculty of Science, Physics Department, Al Azhar University, Cairo, Egypt.
Aug 2001 - Jun 2003	Pre-Master on Experimental Physics, Faculty of Science, Physics Department, Al Azhar University, Cairo, Egypt.
Aug 2003 - Jun 2005	Master's degree in Physics, Faculty of Science, Physics Department, Al Azhar University, Cairo, Egypt. Title: *Preparation and Spectroscopic Studies of Some Chalcognides in the Nanorange.*
Dec 2005 - May 2007	Assistant Researcher Spectroscopy Dept, Physics Division, NRC. Giza, Egypt.
May 2007 - October 2012	Start of Ph.D in Physics, Universität Augsburg, Augsburg, Germany.

List of publications

- *Magnetic-Order-Induced Crystal Symmetry Lowering in ACr2O4 Ferrimagnetic Spinels.* S. Bordacs, D. Varjas, I. Kezsmarki, G. Mihaly, L. Baldassarre, A. Abouelsayed, C. A. Kuntscher, K. Ohgushi, and Y. Tokura, Phys. Rev. Lett. **103**, 077205 (2009).

- *Pressure-induced phenomena in single-walled carbon nanotubes probed by infrared spectroscopy.* A. Abouelsayed, K. Thirunavukkuarasu, K. Kamarás, F. Hennrich, and C. A. Kuntscher, High Pressure Research **29**, 559 (2009).

- *Role of the Pressure Transmitting Medium for the Pressure Effects in Single-Walled Carbon Nanotubes.* A. Abouelsayed, K. Thirunavukkuarasu, F. Hennrich, and C. A. Kuntscher, J. Phys. Chem. C, **144**, 4424 (2010).

- *Pressure-induced phenomena in single-walled carbon nanotubes: Structural phase transitions and the role of pressure transmitting medium* C. A. Kuntscher, A. Abouelsayed, K. Thirunavukkuarasu, F. Hennrich, Phys. Status Solidi B, **247**, 2789 (2010).

- *Pressure studies on fullerene peapods* C. A. Kuntscher, A. Abouelsayed, Á. Botos, Á. Pekker, and K. Kamarás, Phys. Status Solidi B, **248**, 2732 (2011).

- *Pressure effects on unoriented and oriented single-walled carbon nanotube films studied by infrared microscopy* C. A. Kuntscher, A. Abouelsayed, K. Thirunavukkuarasu, F. Hennrich, and Y. Iwasa, J. Appl. Phys. **111**, 112614 (2012).